HIGH RESOLUTION MRI OF THE HUMAN BRAIN USING REDUCED-FOV TECHNIQUES AT 7 TESLA

By

Christopher Joseph Wargo

Dissertation

Submitted to the Faculty of the

Graduate School of Vanderbilt University

in partial fulfillment of the requirements

for the degree of

DOCTOR OF PHILOSOPHY

in

Biomedical Engineering

August, 2011

Nashville, Tennessee

Approved By:

John Gore, PhD

Adam Anderson, PhD

Brian Welch, PhD

Victoria Morgan, PhD

Seth Smith, PhD

Copyright © 2011 by Christopher Joseph Wargo
All Rights Reserved

In Memory of my Dad,
Timothy John Wargo, MD

Dedicated to my Mom,
Lorraine Marie Wargo, RN

ACKNOWLEDGEMENTS

The work described here is the result of collaborations with a number of individuals that I would like to acknowledge for their support and assistance over the years, without which, it would not have been completed. First, John Gore, who has been a valued advisor and mentor with comprehensive imaging experience, provided a supportive environment to freely explore ideas within an exceptional imaging facility. I also wish to thank my committee members. First Adam Anderson, with a strong MR background and specific experience in DTI, he was the first to teach me MRI through early graduate coursework. Brian Welch has an expertise of the Philips system that is arguably unrivaled in our imaging institute, I have benefited from that many times over the years. Victoria Morgan provided a comprehensive background in clinical human imaging with specific application in epilepsy. Though the initial aim in this area was not realized, it remains a strong interest. Seth Smith supported the work with excellent practical MR knowledge and a passion for spinal cord imaging. This thesis was largely motivated by contemplating whether histological spinal cord slides could be replicated in quality using MRI. An added thanks to Calum Avison who advised my Masters thesis that taught me much about coil design and parallel imaging, and resulted in the use of SENSE described here.

Beyond the committee, I would specifically like to acknowledge Jay Moore, Marcin Jankiewicz, and Huairen Zeng for their support with RF design, assisting in the implementation of the explored composite RF pulses, and spiral and spoke excitations. I also thank Ha-Kyu Jeong for his help defining human DTI protocols

and reconstructions, and acknowledge the human imaging facility staff, Leslie McIntosh, Debbie Boner, Donna Butler, and Robin Avison, as well as Chuck Nockowski for his technical support with 7T failures. This work would not have been completed without regular subjects, a special thanks to BH, LW, TR, GC, JV, AF, JT, KS, and BG. Thanks also to Stephan Fischer of Philips Medical Systems who taught Philips pulse programming and assisted with the first STEAM version the methods are derived from. I also acknowledge Johan van den Brink for suggesting OVS use for 3D scans, motivating the described OVS-IVI 3D imaging approach.

The remainder of acknowledgements are directed at sources of moral support, including various individuals throughout the VUIIS too numerous to mention. A special thanks to Nancy Hagans for all the help she has provided over the years. To my office mates in AA1112, thank you for the constant technical and moral support. To friends throughout the BME department, Vanderbilt campus, Nashville area, and across the US, a big thank you for the timely distractions when I needed it most. Finally, I want to give my thanks and love to my family, my brothers Sean and Andrew, their wives Cindy and Kat, and my nieces and nephew, Laura, Grace, and Colin, I would not have made it to this point without you. To my Mom, this work is dedicated to you for being a constant and unwavering supporter through it all despite recent challenges. I complete this thesis in memory of my father who passed unexpectedly before I completed this work. His passion for medicine and commitment to the care of others remains a constant source of motivation for me. It is written with hope that in some small way, it helps contribute to improvements in medical diagnostics and therapy for individuals such as him.

TABLE OF CONTENTS

Chapter Page

LIST OF FIGURES

Figure Page

CHAPTER I

INTRODUCTION

Magnetic Resonance Imaging (MRI) is a modality commonly applied in medical clinical and research practice to provide visualization of internal biological tissue structures. For human applications, this enables specific anatomical features to be identified and assessed for diagnostic purposes or to probe tissue physiological processes and pathologies. Compared to other approaches such as x-ray, PET, and SPECT, MRI uses non-ionizing radiation while providing distinct soft tissue contrast for anatomical identification that can be customized for the application. Functional and dynamic properties can also be investigated to explore topics ranging from brain activation under stimulus, cardiac function, and receptor uptake using exogenous contrast agents. Unique characterization of diffusion behavior, vascularization, and relative tissue properties can also help to understand the effects of disease and potential treatments.

Advancements in MRI technology are driven largely on improving image quality for these applications, enhancing methods of contrast to identify specific features of interest, and extensions to functional and dynamic applications that can be implemented for clinical use. Image quality improvements specifically focus on enhancing detectable signal, increasing image resolution, and reducing corrupting artifacts. Of these, resolution is central to image quality to enable discernment of specific anatomical features or to spatially and temporally define functional behavior.

In MRI, resolution is challenged by the trade-off between the image signal-to-noise ratio (SNR) and the achieved voxel size; smaller voxel sizes produce lower SNR values potentially diminishing overall quality. In addition, high-resolution can require obtaining a large number of points for a specific field-of-view (FOV) size that is constrained to the dimensions of the object in the plane imaged to prevent fold-over or aliasing effects. Such scan durations can become prohibitive and are sensitive to patient bulk and physiological motion effects, with acquisition of large data set increasing sensitivity to susceptibility variation causing image blurring and distortion.

Attempts to counter these obstacles to high-resolution imaging has driven increments in the magnetic field to ultra-high field strengths, such as 7T, to provide additional signal to support resolution improvement. However, 7T application for *in vivo* high-resolution imaging has not been unambiguously accomplished, and faces a number of challenges such as increased B1 inhomogeneity and shorter T_2* values. Solutions to efficiency constraints and time-dependent artifact sensitivity have resulted in a variety of rapid imaging techniques such as echo planar imaging (EPI) and parallel imaging methods that reduce overall image data sizes. Similar acceleration is possible by selectively restricting the signal to localized FOV dimensions using reduced-FOV methods, but this approach has currently not been optimized for human imaging at the 7T field strength. Conceivably, such an approach is attractive when imaging experiments are isolated to specific regions of interest in the brain to enable high reduction of the FOV dimensions.

In this work, we aim to address this later deficiency by implementing a variety of reduced-FOV approaches at 7T that have been optimized for the challenges at

this ultra-high field strength, with comparisons of relative performance to determine the best approach for high-resolution imaging. This optimal approach will be applied to explore localized imaging in the human brain targeting *in vivo* 160 to 300 μm resolutions, with specific emphasis on improvements in scan duration and reduction of time-dependent artifacts to obtain high image quality. Where applicable, reduced-FOV will synergistically be combined with additional rapid imaging techniques such as EPI, parallel imaging, and partial fourier methods to achieve the highest accelerations possible in data acquisition. Additional exploration of the benefits of this rapid imaging approach will be performed for high-resolution brain diffusion tensor imaging, and localized acquisitions of the cervical spinal cord.

CHAPTER II

BACKGROUND

1. Basic Principles of MRI

Magnetic resonance signal is established by manipulation of atomic nuclei with magnetic moments, typically hydrogen protons due to water abundance in humans. The proton contains spin angular momentum with a current about the spin axis that results in production of its own magnetic field and dipole moment. Exposure of the proton to an externally applied strong magnetic field causes the dipole moment to orient at an angle in relative alignment with the local field direction. The applied torque results in precession of the proton around the main field at an angular frequency that is dependent on the field strength, B_0, and gyromagnetic ratio of the hydrogen proton, γ (42.6 MHz/T) as defined by the Larmor equation [1]:

$$\omega_0 = \gamma B_0 \qquad 2.1$$

Here, the gyromagnetic ratio corresponds to the ratio of the proton magnetic moment and its angular momentum. Since the spin angular momentum for the hydrogen proton is quantized, its magnetic moment alignment can only be in two states: parallel or anti-parallel to the applied external field. The latter is the higher energy state; as a result, a small excess of protons in a specific volume will be in parallel alignment with B_0. For such a volume, the total excess of parallel moments defines the net magnetization, M_0, as dictated by Boltzmann probability, the volume proton spin density, ρ_0, and sample temperature T [1] :

$$M_0 = \frac{\rho_0 \gamma^2 \hbar^2}{4kT} B_0 \quad 2.2$$

2. Manipulation of Magnetization Using Applied RF Pulses

Ultimately, this net magnetization is the source of signal in an MRI experiment used to provide information about the object imaged. To initiate detection, the established magnetization vector is tipped away from B_0 by applying a time-varying radiofrequency waveform over a specific duration. The RF energy of this pulse is generated in a direction orthogonal to the main field by a transmission coil external to the object. In order to effect the proton spin magnetization and induce a downward nutation of the magnetization into the transverse plane perpendicular to B_0, the frequency of the RF pulse must be on resonance, matching that established for protons by the Larmor equation. Typically, M_0 is tipped 90º by the RF pulse to ensure the full magnetization is detected, but any specific 'flip angle", θ, may be targeted. The achieved flip angle corresponds to the time integral of the RF pulse, $B_1(t)$, with the transverse magnetization determined by the resulting angle [2]:

$$\theta(t) = \gamma \int_{-t}^{t} B_1(t) dt \quad 2.3$$

$$M_{xy} = M_0 \sin\theta \quad 2.4$$

Once tipped, it is the magnetization precession in the transverse plane that generates a detectable signal. The time-varying magnetic flux caused by the rotating magnetization establishes an electromagnetic force in a nearby receive coil by induction which generates a voltage that has a dependency on the density of protons in the volume and the external magnetic field strength [1]:

$$S \propto \frac{\gamma^3 B_0^2 \rho_0}{T} \quad 2.5$$

3. Magnetization Relaxation Effects

Immediately after RF pulse application, the established transverse magnetization begins to decay exponentially at a rate described by the time constant T_2*. This results from interactions between spins that cause local field variations and subsequent dephasing of the magnetization vector, and is dictated by local tissue properties. Additional decay is caused by inhomogeneity of the externally applied field by the time constant T_2' that can result from tissue susceptibility variations or main magnetic field errors that have not been properly addressed by shim gradients. The T_2 and T_2' effects define the overall T_2* relaxation time [1]:

$$\frac{1}{T_2^*} = \frac{1}{T_2} + \frac{1}{T_2'} \qquad 2.6$$

After spins are first exposed to the applied magnetic field or perturbed by an RF pulse to tip onto the transverse plane, recovery of longitudinal magnetization is described by the T_1 relaxation time. Spins in a magnetic field undergo interactions with the surrounding lattice environment as a result of thermal motion and vibrations, thereby losing energy and reorienting with the main magnetic field, B_0. The effects of relaxation times on the longitudinal and transverse magnetization, M_z and $M_\perp$, can generally be described by the Bloch equations to establish their behavior over time, where M_0 corresponds to the total equilibrium magnetization available [1]:

$$M_\perp(t) = M_0 e^{-t/T2} \qquad 2.7$$

$$M_Z(t) = M_0\left(1 - e^{-t/T1}\right) \qquad 2.8$$

4. Spatially Selective RF Pulses Using Gradients

The transverse magnetization generated by application of an RF pulse affects all spins in a volume that are on resonance with the pulse frequency. To provide

spatial localization of spin excitation, RF pulses are performed with simultaneously active gradients that induce an additional linear variation in magnetic field strength along a specific direction. By the Larmor relationship, this translates to a spatial variation in the spin frequency as determined by the achieved field along each direction, B_x, B_y, and B_z, in combination with the external field, M_0 [1]:

$$\omega(\vec{r}) = \gamma B_{eff} = \gamma\left(B_0 + B_X\hat{\imath} + B_Y\hat{\jmath} + B_Z\hat{k}\right) \quad 2.9$$

To excite spins only located within a specific slice width, an active linear gradient is applied in the slice direction that results in the spin frequency varying across the gradient profile. Restricting the RF pulse to a specific bandwidth causes only those spins within that frequency range to tip toward the transverse plane. To achieve a specific target slice thickness, Δz within which spins are excited, the gradient strength, G_Z, and RF pulse bandwidth, BW, must be adjusted accordingly [2]:

$$\Delta z = \frac{BW}{\gamma G_Z} \quad 2.10$$

The added effect of the applied gradient is not only a distribution of frequencies while it is active but also a variation in the phase of spins as they precess due to their altered frequencies. The specific phase encoded for a spin at a particular location within the gradient profiles is calculated from the gradient integral [1]:

$$\Delta\varphi(\vec{r}) = -\vec{r} \cdot \left[\gamma \int_0^t \vec{G}(t)\, dt\right] \quad 2.11$$

5. Pulse Sequence Design

Achieving targeted imaging of a specific plane in an object or person requires combining the selective capability of gradients and RF pulses with the spatial frequency and phase encoding described above. This is accomplished using pulse

sequences that describe the order of RF pulse and gradient activation relative to the time window over which signal information is acquired. A common approach for image formation and acquisition is the gradient echo imaging method, pictured in figure 2.1. This sequence initiates with simultaneous application of an RF pulse and slice selective gradient. Resulting phase variations across the slice profile are corrected by a subsequent refocusing gradient that has half the area but the opposite amplitude to the selective gradient to ensure spins are all in phase when it is complete. The subsequent applied gradients are used to perform both phase and frequency encoding of spins in the excited slice, with each spatial location in the plane possessing a unique phase and frequency value. In the k-space formulation, the area of the applied gradient over a specific duration corresponds to a specific spatial frequency or k-value along the orientation that the gradient is active [2]:

$$\vec{k}(t) = \frac{\gamma}{2\pi}\int_0^t \vec{G}(t)dt \qquad 2.12$$

The encoding performed by the combination of gradients along the x and y dimensions effectively provides coverage of the full spatial frequency definition of its

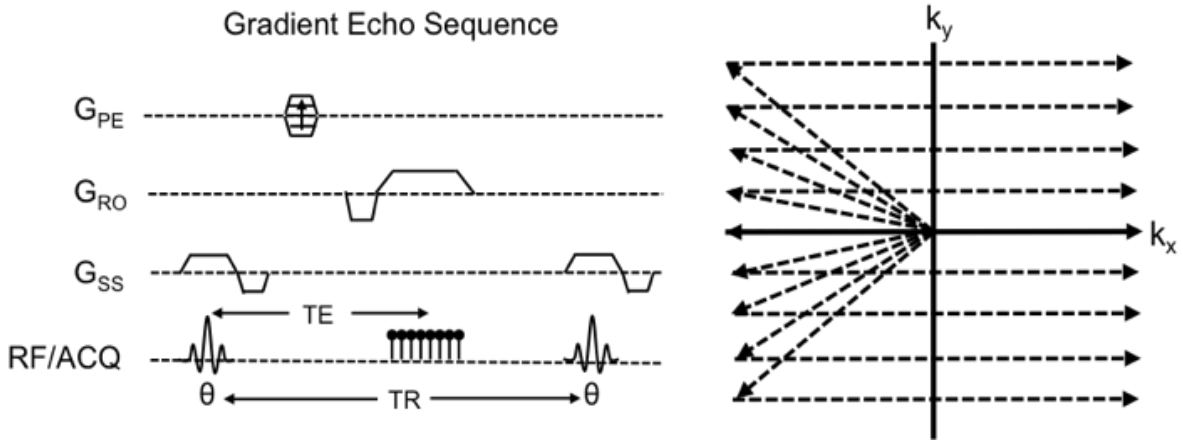

Figure 2.1 – Gradient echo pulse sequence demonstrating relative timing of slice selective RF pulse, refocusing, prephasing, phase encoding, and readout gradients. Readout trajectory through k-space with a single line along k_x acquired each TR.

image domain representation, which are related by Fourier transform [1]:

$$\rho_m(x,y) = \frac{1}{2\pi}\int_{-\infty}^{\infty} S_m(k_x,k_y)e^{i(k_x x+k_y y)}dk_x dk_y \qquad 2.13$$

Here, ρ_m corresponds to the image domain proton density and S_m is the measured signal amplitude at the k_x and k_y spatial frequencies. Specifically, acquiring the k-space information is achieved after slice selection by applying a phase encoding gradient with amplitude iteratively adjusted from $\pm G_y$ each readout to cover the range of spatial frequencies in that dimension by establishing specific phase distributions. The subsequent prephasing gradient along x dephases spins prior to readout, transitioning the acquisition to a minimum $-k_x$ value. This dephasing is refocused by the following readout gradient to form an echo, establishing a frequency variation along the x dimension. Each acquisition step while the readout is active corresponds to a step along the k_x spatial frequency axis. By properly defining the phase encoding, prephasing, and readout gradients, k-space is sampled to enable Fourier transformation of the acquired data to generate an image, with coverage of k-space in a cartesian sampling pattern depicted in figure 2.1. Each line is acquired after a single application of an RF pulse, with the time between RF pulses defined as the repetition time, or TR, and the time between the RF and echo formation at the center of the readout gradient specified as the echo time, or TE.

Alternatively, imaging can be described using a spin echo sequence as depicted in figure 2.2. This sequence incorporates an additional RF pulse after the initial excitation is performed that is also slice selective, but adjusted to a 180° flip angle. The purpose of this additional pulse is to refocus spins that have dephased due to field inhomogeneity or T_2* relaxation effects after excitation. By timing the

application of this refocusing pulse to correspond to a point at half the target echo time, the accumulated phase that has occurred since the initial RF pulse can be reversed to form an echo during readout, half the echo time later. The benefit of this approach is that it enables the image to be T_2 versus T_2* weighted, providing an alternate contrast or to address the sensitivity to field inhomogeneity effects.

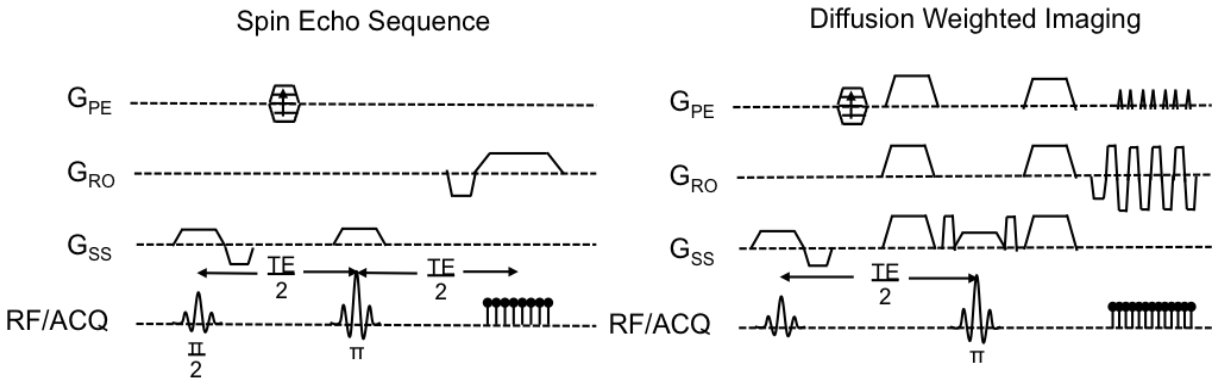

Figure 2.2 – Spin echo sequence diagram incorporating a 180° selective refocusing pulse prior to readout at half the echo time. Diffusion weighted spin echo scan with EPI readout.

6. Diffusion Tensor Imaging

As described, the spin echo pulse sequence can be modified to establish images weighted by tissue diffusion properties using a pair of balanced gradients that have been positioned around the applied refocusing RF pulse (figure 2.2). Water molecules that are stationary between these gradients will have proton spins first dephased and then refocused, with no overall change in signal strength. However, these molecules are free to diffuse in their local environment, following a random walk or Brownian motion. Proton spin spatial translations caused by diffusion will effectively result in spins achieving an altered position within each gradient, causing an overall dephasing effect the larger the diffusion distance to produce a corresponding loss in the observed signal magnitude [2]:

$$S = S_0 e^{-bD} \tag{2.14}$$

Here, S is the measured signal relative to the S_0 reference signal, D defines the diffusion constant along a specific physical dimension, and b is a function of the applied strength, G, of the gradient pair and their separation in time, Δ, and duration, δ, that can be customized to increase diffusion weighting [2]:

$$b = \gamma^2 G^2 \delta^2 (\Delta - \delta/3) \tag{2.15}$$

The local water molecule environment may possess a specific organization that constrains diffusion to favor specific directions. Adjusting the orientation of the applied gradients enables enhanced directional sensitivity. Repeating the sequence multiple times with different gradient orientations enables a tensor, $\overline{\overline{D}}$, to be estimated that contains information about the localized diffusion properties to describe preferential diffusion directions [2]:

$$\overline{\overline{D}} = \begin{bmatrix} D_{xx} & D_{xy} & D_{xz} \\ D_{xy} & D_{yy} & D_{yz} \\ D_{xz} & D_{yz} & D_{zz} \end{bmatrix} \tag{2.16}$$

The mean value of the trace of this matrix defines the apparent diffusion coefficient (ADC) that describes the magnitude of the diffusion properties. Translating to an alternate coordinate system that defines three axis of an ellipsoid is achieved by calculating the eigenvalues and eigenvectors from the tensor that correspond to the ellipsoid shape and orientation. These eigenvalues, λ_1, λ_2, λ_3, and eigenvectors provide mapping of the local anisotropy to demonstrate preferential diffusion directions that coincide with highly organized structures such as white matter fiber tracts that connect brain regions, quantified by fractional anisotropy (FA) values [3]:

$$FA = \sqrt{\frac{1}{2}} \cdot \sqrt{\frac{(\lambda_1 - \lambda_2)^2 + (\lambda_2 - \lambda_3)^2 + (\lambda_1 - \lambda_3)^2}{(\lambda_1^2 + \lambda_2^2 + \lambda_3^2)}} \quad 2.17$$

As described, Diffusion Tensor Imaging (DTI) provides unique contrast reporting on diffusion properties and underlying brain white matter organization. Diffusion weighting can additionally be used to assess tissue changes that can have specific pathologic implications. The challenge with this approach is a high sensitivity to bulk patient motion effects necessitating rapid acquisition strategies to minimize phase offset errors that induce image ghosting artifacts. Acquisition of multiple directions of diffusion weighted images that ranges from 6 to 30 also necessitates long scan durations on the order of 10 to 20 minutes, constraining resolution.

7. Image FOV and Resolution

As previously described, the acquisition performed during a pulse sequence corresponds to sampling of k-space points that represent the Fourier transform of the spatial domain image. Each step in k-space is accomplished by maintaining the gradient in that direction for an additional specific time step. The k-space step size corresponds to the field-of-view (FOV) of the image in the phase encode and readout directions, defining the overall spatial dimensions of the image [1]:

$$FOV_{PE} = \frac{1}{\Delta k_{PE}}, \qquad FOV_{RO} = \frac{1}{\Delta k_{RO}} \quad 2.18$$

Discrete sampling of the continuous object k-space is a convolution of the object image and the Fourier transform of the sampling function, diagrammed below for the 1D case (figure 2.3). This effectively replicates the object image at each transformed sample point in the spatial domain. The distance between each replicated spatial image is dictated by the image FOV, which corresponds to the

inverse of the k-space sampling step size. As a result, a reduction in Δk produces a larger acquired FOV and an increased separation between replications of the object in the image. Large steps in k-space however, result in a smaller FOV and separation distance, which at some point will cause object image overlap or 'aliasing'. The Nyquist criterion puts a constraint on the maximum step size to prevent the aliasing effect; essentially this corresponds to the step size that translates to a FOV that fully captures the spatial dimensions of the object.

For a specific FOV size, the length along a particular dimension and the number of discrete points sampled define the spatial resolution of the image. The spatial resolution can be related to the k-space spatial frequency by the FOV definition, where N points sampled at a Δk step to achieve a specific FOV size result in a definable maximum spatial k-space frequency being reached [1]:

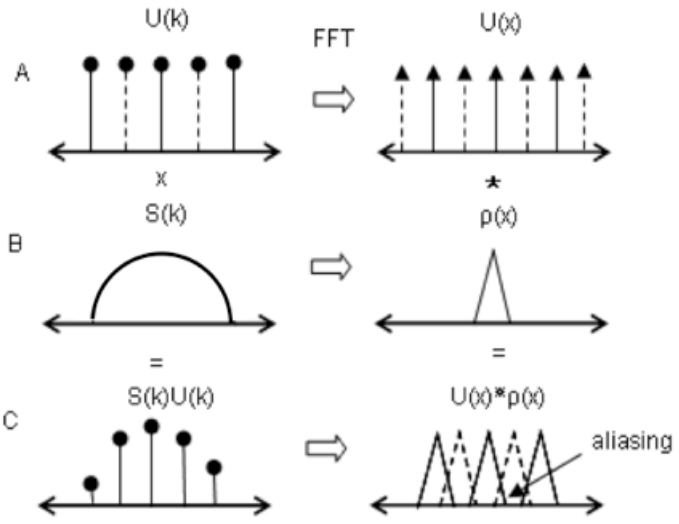

Figure 2.3 – 1D aliasing. Discrete sampling of the function S(k) is achieved by multiplying it with a train of impulses spaced according to the sampling rate. This corresponds to the convolution of the fourier transform (FT) of S(k) and the discrete sampling train FT. The function will alias causing fold-over if the sampling FT is narrowly spaced, indicating a low k-space sampling rate.

$$\Delta x = \frac{FOV}{N_x} = \frac{1}{\Delta k_x N_x} = \frac{1}{k_{max}} \qquad 2.19$$

In essence, the resolution is inversely proportional to the maximum k-space spatial frequency reached by the sampling pattern, with higher spatial frequencies resulting

in a smaller spatial resolution. High spatial frequencies in this case are intuitively necessary to define the sharp transitions in image spatial information that are apparent at the improved resolution. Sampling definition thus is based on the desired resolution and FOV size, which determines the number of points required along a specific dimension and the resulting sampling frequency for the sequence. These parameters additionally define the scan duration when used by the applied pulse sequence, with N_{PE} phase encoding lines acquired, one line each TR [2]:

$$T_{acq} = N_{PE}TR \tag{2.20}$$

8. The SNR Equation

Accounting for the discrete sampling of image signal information, generation and detection of magnetization, and signal corruption by various noise sources enables quantification of the overall image signal strength in excess of an established noise threshold. The signal-to-noise ratio (SNR) is a fundamental component of image quality and must be properly managed to establish usable or interpretable images. The signal fundamentally is driven by the established magnetization, with the underlying proton density within a voxel dictating the total regional magnetization available. The resolution of the image determines the dimensions of an individual voxel and thus dictates the maximum potential signal [1]:

$$s(k_x, k_y, k_z) = \iiint dxdydz\rho(x, y, z)e^{-i2\pi(k_x x + k_y y + k_z z)} \tag{2.21}$$

The source of noise in the image is primarily thermally induced signal fluctuations resulting from resistances in the elements responsible for signal generation or detection. The first of these includes resistances within the receptor coil circuitry, as well as interactions of the fluctuating magnetic field within the coil

and nearby conductive elements such as shielding or other coil elements. Second, the receiver channel and electronics have additional resistances in cabling, amplifiers, and A/D convertors. Third and finally, the subject is a conductive and lossy medium that interacts with the oscillating field. Each portion can be quantified by a specific resistance value that defines the total noise voltage signal that is impacted by sample temperature and the bandwidth of the voltage, Δf [4, 5]:

$$V_n = \sqrt{4kTR_{total}\Delta f} \tag{2.22}$$

$$R_{total} = R_{coil} + R_{subject} + R_{electronics} \tag{2.23}$$

From the corresponding ratio of factors contributing to signal and noise in a detected image, the SNR can theoretically be predicted for a given MR experiment based on selected scan parameters. Specifically, the SNR in a single voxel will be dependent on the voxel dimensions as defined by the image resolution (Δx, Δy, Δz), the image dimensions (N_{PE}, N_{RO}), the total number of acquisitions (N_{acq}) combined to improve SNR, and the bandwidth of the data sampling at readout [1]:

$$\frac{SNR}{voxel} \propto \Delta x \Delta y \Delta z \sqrt{\frac{N_{PE} N_{RO} N_{acq}}{BW}} \tag{2.24}$$

In general, MR imaging requires assessment of this equation to understand the impact of specific parameter choices that effect image quality, establishing a tradeoff between their values and the predicted SNR. Specifically, improvements in resolution correspond to an overall loss in SNR; a two-fold in plane resolution improvement induces a 65% reduction in the obtained SNR, with slice thickness factor changes inducing a matching loss. The extent to which resolution can be adjusted is dependent in part on the available signal to support it before the noise

threshold is reached and image quality is greatly diminished. Incorporating additional acquisitions into the specified scan can counter resolution SNR losses, however, it results in a factor increase in the total scan duration [1]:

$$T_{acq} = N_{PE} N_{acq} TR \qquad 2.25$$

As resolution is improved from millimeters to microns, matrix sizes can significantly inflate, theoretically reaching several thousand along the phase encoding dimension, producing long scan durations. Optimization of TR provides a degree of flexibility in scan duration but is constrained by desired contrast and limits on the energy deposited by RF pulses that induce heating effects. These effects are compounded by the need to incorporate acquisitions to address SNR losses as resolution improves, dependent on the minimum SNR required to obtain a usable image.

9. Ultra High Field MRI

A number of MRI advancements target the parameters that directly improve the achievable SNR, with the goal of improving resolution. Equation 2.5 above specifically predicts that signal is directly proportional to B_0^2, which has driven magnetic field strengths to be incrementally increased as technology warrants this improvement, with 3T systems now a common field strength for clinical diagnostic imaging. For general human studies, scanners at 7T are now available and applied for research use but are currently not FDA approved for clinical applications. 7T predicts a 2.33 fold in SNR relative to 3T from field strength improvement alone.

However, ultra high field MRI faces a number of technical challenges related to the change in frequency from 128 MHz at 3T to 300 MHz at 7T. First, the wavelengths at the higher field approach dimensions of the human head and induce

dielectric resonance or interference patterns in RF waveforms applied by transmit coils. The effect is a spatial variation in the achieved flip angle relative to that prescribed that can diminish observed signal in regions where the angle is substantially different. Second, tissue T2* values are shorter producing a rapid dephasing of spins compared to lower field strength, which can induce blurring and distortion image artifacts. Lastly, field strength increases the amount of power deposited to tissue when an RF pulse of a specific angle, θ, and bandwidth, Δf, is applied, as defined by the specific absorption rate (SAR), challenging the design of commonly used pulse sequences and RF pulses [1]:

$$SAR \propto B_0^2 \theta^2 \Delta f \qquad 2.26$$

10. Time-Dependent Imaging Artifacts

Beyond ensuring adequate signal for high-resolution imaging using parameter optimization or advanced ultra high field systems, a number of time dependent artifacts must be managed to obtain quality images. First, for *in vivo* human subject imaging, patient motion often occurs despite the best efforts of the subject to control or minimize. The specific sources of motion typically consist of head or body bulk movement, and physiological effects such as heartbeat, blood flow, swallowing, breathing, or blinking [6, 7]. The motion results in a specific region translating to another physical position where it experiences a different applied magnetic field between phase encodings. This results in a “ghosting” or blurring artifact dependent on the nature of the particular motion. Longer scans are required to obtain large matrix sizes for high resolution imaging and increase the opportunities for subject

motion effects to occur, thus making motion-based artifacts more prevalent in the final image. The result of these effects is an overall loss of image quality.

In addition to subject motion, artifacts can also be produced by localized variations in the magnetic field strength that are not due to actively applied gradients. These are often caused by regions of sharp susceptibility difference in the object such as that occurring between tissue and air interfaces near sinuses. The produced field variations cause a localized dephasing of spins that is in addition to normal T_2 effects, resulting in regions of signal voids or blurring depending on the T_2* relaxation time. The specific T_2* value determines the extent of the blurring or filtering effect that is characterized by a particular point spread function (PSF) with a full-width-half-max (FWHM) value dependent on the sampling duration, T_S, and target resolution along the specific direction sampled, Δx. Assuming a gradient echo scan, the predicted PSF effect in the readout or x dimension translates to [2]:

$$FWHM = \frac{\sqrt{3}}{\pi}\left(\frac{T_S}{T_2^*}\right)\Delta x \qquad 2.27$$

The blurring that results hinders the maximum possible resolution, significant for sampling times that exceed T2* as can occur when the matrix size is large for high resolution imaging. In addition to this effect on image quality, localized variations in the magnetic field translate to errors in the position encoding during a scan, resulting in geometric distortions in the final image that alter the apparent shape of an object. The shift of any point x can be characterized by the gradient in the magnetic field established by susceptibility variation, G_v relative to the applied gradient, G_x [2]:

$$x_{shift} = x\left(1 + \frac{G_v}{G_x}\right) \qquad 2.28$$

11. Rapid Imaging Techniques

Necessary temporal and spatial resolution increments as well as the impact of time dependent artifacts caused by susceptibility variations and physiological and bulk movement, have resulted in a number of techniques to diminish overall scan times. Partial Fourier methods typically cut scan times in half by acquiring half the k-space data, using k-space symmetry to fill in missing information [8]. Recent efforts have explored sampling patterns below Nyquist limits using so-called compressed sensing (CS) techniques that rely on sparsity of the data set and an incoherent sampling pattern to prevent a coherent aliasing of the undersampled data [9], but are computationally intensive and require further validation. Most common of the rapid imaging approaches are echo planar imaging (EPI) readouts and parallel imaging methods, with similar reduction achieved using smaller imaging FOV sizes.

12. Echo Planar Imaging

The gradient and spin echo sequences described previously can be modified to incorporate a rapid readout strategy that obtains the full k-space information in a single acquisition using the EPI approach, providing significant reduction in the overall scan duration (figure 2.4) [2]. After readout prephasing, the readout gradient

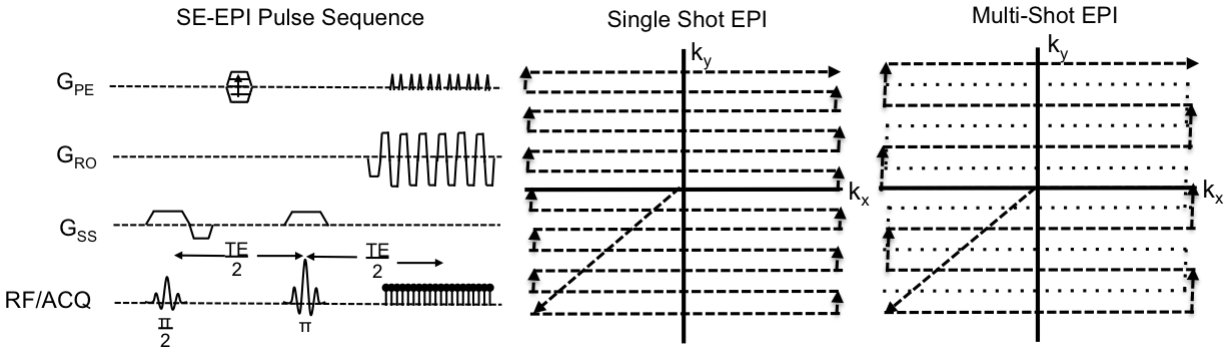

Figure 2.4 – SE scan with EPI readout using blipped phase encoding and oscillating readout gradients. Single shot EPI covers full k-space after single RF pulse; multi-shot acquires a fraction of total k-space each TR, demonstrated here for two shots.

is modified to perform a waveform that alternates in polarity. In this configuration, the positive and negative gradient sections correspond to acquisitions along the x dimension to obtain a single line of k-space. This polarity shift effectively alternates the readout direction, with an echo formed at the center of each acquisition window. The phase encoding gradient is additionally replaced with a prephasing gradient to initialize the acquisition to $-k_{max}$ in the y direction, followed by a series of blips that occur between each readout polarity switch. The blips effectively adjust the acquisition to alternate k_y lines until k-space is fully sampled (figure 2.4). Using one excitation before full k-space acquisition describes single shot EPI, with an alternate multi-shot method acquiring a fraction of the k-space lines after each RF pulse.

As described, EPI is characterized by the spacing between echoes established by each gradient polarity shift, and the total time necessary to acquire all lines of k-space for one excitation, or the echo train length. The minimum echo spacing (t_{esp}) is defined by the number of readout points (N_x), the readout dimension FOV (FOV_x), the maximum readout gradient strength (G_x), and slew rate (S_R) [2]:

$$t_{esp} = \frac{2\pi N_x}{\gamma FOV_x G_x} + \frac{2G_x}{S_R} \qquad 2.29$$

The echo spacing and echo train length for single shot EPI establishes a limit for the repetition time, which defines the scan time for a single slice acquisition. For multi-shot EPI, the scan time is dependent on the TR and the number of shots, N_{shot}, which is defined by the total number of k-space lines in the phase encoding dimension, N_{PE}, and the factor of phase encoding lines acquired each shot, f_{epi} [2]:

$$T_{scan} = TR \times \left(N_{PE}/f_{epi}\right) = TR \times N_{shot} \qquad 2.30$$

The relationships defined for echo spacing, echo train length, and scan duration have specific implications on the effects of image resolution increments. Achieving the minimum echo spacing to maintain an overall short train length necessitates a broader readout bandwidth which yields lower SNR yet reduced sensitivities to T_2* blurring and distortion effects described previously. EPI is highly sensitive to T_2* effects due the echo centered on each line of k-space occurring at a different TE times compared to a conventional cartesian readout where every line of k-space has a matched TE. The disparity in echo times for for EPI increases the greater the number of points necessary to cover the full echo train length, increasing the echo spacing. Generally, the echo spacing defines the phase encoding dimension bandwidth that is impacted by the number of shots performed [2]:

$$BW_{PE} = \frac{N_{shot}}{t_{esp}} \tag{2.31}$$

Increasing the number of shots to greater than one results in a multi-shot configuration, where the bandwidth is effectively increased to reduce phase encoding artifact sensitivity, however at a cost of longer overall scan time. The bandwidth is typically much smaller than the readout direction, as a result the geometric distortion artifacts are more apparent along the phase encoding dimension. To effectively apply EPI, proper balance must be achieved between the total acceleration based on the number of shots, resolution for the target FOV size, gradient limitations, and resulting artifacts in the final obtained image. The potential acceleration enabled by this approach acquires a single image in fractions of a second; however, typically requires millimeter resolutions to prevent image artifacts.

Improvements in EPI performance have been demonstrated using parallel imaging methods that lower the number of points sampled for shorter echo train lengths [10].

13. Parallel Imaging Methods

Rapid acquisition using parallel imaging is accomplished by implementing multi-channel receiver coils for signal detection [11]. The individual elements are spatially positioned to provide coverage of unique portions of the object, defined by the individual coil sensitivity profile across the image plane. From a signal perspective, receiver array technology is preferable to volume coil reception due to the relative shorter distances and areas over which the small coil elements are sensitive to, integrating less noise in the detected signal. Proper coil organization enables the combined elements to provide the same overall coverage as a volume coil by combining the individual signals from each receiver channel.

The distinct spatial weighting achieved by the sensitivity of each coil element has additionally been used for image acceleration. As described previously, the object dimensions dictate the necessary step size along each k-space direction specified by the Nyquist criteria to prevent an aliasing artifact. This artifact results in a superposition of intensities from distinct locations in the object, predicted by the sampling pattern used to acquire the image. Skipping every alternate line of k-space for a two-fold reduction, for example, results in two points superimposing at every image location. Each coil element has a corresponding weight applied to these points in the image that is unique based on the defined sensitivity profile for a distinct element. The superimposed points are thus a result of the combined underlying proton densities and effect of the coil profile at the locations

superimposed. With multiple elements, a set of equations can be defined for any superimposed points that incorporate the spatial weights applied by each coil. Calculating the underlying proton density, ρ, requires solving:

$$S(x,y) = C(x,y)\rho(x,y) + N(x,y) \quad 2.32$$

Here, S corresponds to the superimposed signal intensity detected by each coil element, C the individual coil sensitivities at the overlapped point locations, and N the signal noise. Using the Sensitivity Encoding (SENSE) approach [10], ρ is solved for by least squares regression, accounting for coil noise correlation, Ψ, with H corresponding to the transposed complex conjugate of the coil sensitivities:

$$\rho = (C^H \psi^{-1} C)^{-1} C^H \psi^{-1} S \quad 2.33$$

To insure sufficient degrees of freedom to perform the unfolding process, the number of points superimposed must not exceed the number of coil elements, constraining the total reduction to the size of the array. However, the SENSE reconstruction process by least squares results in an amplification of noise in the original aliased data set that is reflected in the final image. The extent of this noise amplification is dictated by the so-called “geometry factor”, or g-factor as it is dependent on coil and object geometry, and increases with the reduction factor. The measured SNR is decreased by the g-factor and the reduction factor, R [10]:

$$SNR_{SENSE} = \frac{SNR_{FULL}}{g\sqrt{R}} \quad 2.34$$

As a result of the g-factor penalty to total SNR when using parallel imaging, SENSE based acceleration is typically limited to two to four fold reductions in the phase encoding dimension for human imaging applications at 3T and lower field strengths. The g-factor value however, is diminished as the field strength and number of coil

elements increases for a specific reduction factor targeted, potentially enabling higher accelerations for 7T systems and large array sizes [12].

14. Reduced-FOV Methods

Rather than unfold the aliased image as performed in the parallel reconstruction approach, reduction of imaging data sets can similarly be accomplished by restricting signal excitation to localized areas using reduced-FOV techniques to prevent the fold-over artifact. The principles behind this method are built off of the same techniques applied to achieve slice selectivity with RF pulses for standard imaging sequences. In this case, the orientation of the RF pulse is applied along different spatial dimensions to achieve desired localization by adjusting the orientation of the simultaneously applied gradient. This can effectively achieve phase encoding and readout direction selectively, with the gradient strength adjusted relative to the applied pulse bandwidth for a specific selection dimension width.

Practical implementation of the described reduced-FOV pulse selectivity is typically accomplished using two different approaches. The first set of techniques selectively excite spins in the target FOV only where imaging is to be localized. In the second approach, excitation is performed in slabs external to the imaging FOV, with the excited signal then dephased by applying large gradients using so-called outer-volume suppression methods. The end result is ideally preserved signal in the target area for subsequent readout with all signal external to that region absent. In either case, multiple pulses may be applied to spatially localize the signal within a specific volume or to sufficiently suppress spins external to that region. After

localization, standard imaging methods can typically be performed with the FOV diminished to the new boundaries achieved by the reduced-FOV preparation.

A number of authors have explored this concept using a variety of techniques across applications. Selective excitation was initially achieved using an inner-volume imaging (IVI) approach that sequentially excited perpendicular planes for signal localization, demonstrated at 0.35 T for brain, chest and spine imaging [13]. A number of investigators have adapted this method to achieve two dimensions of localization with a single RF pulse using a formulation first described by Pauly and Hardy [14, 15] along spiral and blipped EPI trajectories through k-space [16-18]. Additional selective excitation has been performed using Stimulated Echo Amplitude Modulated (STEAM) and Point Resolved Spectroscopy (PRESS) techniques [19, 20] that apply a combination of three RF pulses to localize signal to a volume, with STEAM adapted for human brain and cardiac imaging [21]. The OVS suppression based technique that removes spins in slabs outside the FOV of interest has been applied at 3T to measure regional anisotropy and apparent diffusion coefficients in the cervical spine [22], and for cardiac cycle imaging at 1.5T [23]. A B1 Insensitive Train to Obliterate Signal (BISTRO) permutation of OVS was developed using adiabatic pulses for excitation to decrease sensitivity to B1 inhomogeneity effects such as that caused by surface coils, implemented at 4T and later demonstrated at 7T for functional studies [24, 25].

The benefit of these techniques is diminished scan durations for a fixed resolution as a result of the diminished FOV size, necessitating fewer acquired points. However, it requires confining the imaging to restricted portions of an object.

As with SENSE, phase encoding FOV reduction incorporates a loss in SNR by $\sqrt{R}$. Many of the selective techniques also result in saturation of off-slice locations for multi-slice scans as a result of the non-slice selective RF pulses affecting spins at nearby slice locations. A number of authors have implemented adaptations to these techniques incorporating additional RF pulses or 2D confined pulses to minimize or restrict these effects for improved multi-slice SNR performance.

In sum, the techniques to date have primarily demonstrated application at 1.5T and 3T for brain, spine, and cardiac based studies, with resolutions as low as 0.5 mm achieved. A significant number have been used specifically for spinal cord DTI protocols sensitive to motion [17, 22, 26, 27]. In some cases, the results suffered from poor image quality due to low SNR, which may hinder the impact of reduced-FOV for these particular field strengths. However, largely undemonstrated is a comprehensive study of performance at ultra-high field across similar applications or anatomical regions. The higher signal obtainable combined with implementation of parallel imaging hardware previously not available for early studies may prove substantial enough to push achievable resolutions well below 1 mm with proper optimization or introduction of new scan and reduced-FOV methods.

15. High Resolution Human Brain and Spine Imaging

To date, specific demonstration of high-resolution imaging at ultra high field using primarily traditional scan approaches has been performed across a variety of human brain studies. At 7T in particular, investigators initially focused on post mortem *ex vivo* imaging to obtain the highest resolutions recorded over long scan durations. Soria performed multiple sclerosis (MS) lesion imaging in a postmortem

sample using a combination of T1 weighted and DTI scans to obtain 150 μm^2 resolutions with 0.6 mm slice thickness in 1 hour and 59 minutes [28]. Similarly, Geyer investigated post mortem cortical structure achieving 330 μm^3 in 3 hours 50 minutes [29]. Using hippocampus specimens, Weishmann obtained 64 μm^2 resolutions with a 1 mm slice thickness using a T2 weighted sequence and a 65 mm FOV, with images compared against 1.5T 469 μm^2 *in vivo* results. The analysis demonstrated that at 7T the resolution provided visibility of layers not observed at 1.5T [30]. Augustinack obtained similar resolutions while imaging an autopsied human entorhinal layer, achieving 70 μm in a 36 mm FOV that enabled identification of entorhinal islands verified by histology. The investigators predicted that similar *in vivo* results were possible using a combination of parallel imaging methods and motion correction to support the required longer scan durations [31].

The bulk of published high-resolution 7T human *in vivo* imaging studies have primarily occurred in the last few years, with resolutions as low as 200 μm reported. A number of these investigations have targeted specific assessment of MS lesions with comparison against similar measurements at lower field strengths to determine relative lesion counts, microvascular organization, and lesion appearance using different contrast types such as susceptibility and proton density weighting [32-35]. Resolutions have ranged from 200 μm^2 with a 1.5 mm slice thickness in 8:22 minutes, to 330 μm^2 and 1 mm thickness in 10:18 minutes. Cho and Abosch separately achieved similar resolutions of 250 μm^2 and 375 μm^2 at 2 and 1 mm slice thicknesses, respectively, to assist placement of deep brain stimulation (DBS) electrodes for Parkinson's Disease therapy [36, 37]. Among the highest *in vivo*

resolution results, Breyer demonstrated 200 μm^2 to study hippocampus sclerosis in epilepsy patients using a 2:45 minute T2* weighted scan combined with parallel imaging [38]. Investigators have also explored use of 3D single shot EPI scans to achieve 0.5 to 1.5 mm isotropic resolution for full brain functional studies [39-41].

Additional application of EPI has been achieved for human DTI studies targeting both the brain and spinal cord. At 7T, Heidemann obtained 0.7x0.7x3 mm^3 DTI resolutions in the brain using EPI with a segmented readout combined with the GRAPPA parallel imaging method, demonstrating a reduction in susceptibility based blurring and distortion artifacts [42]. Comparing results against 1.5T and 3T, Polders acquired 2 mm isotropic brain DTI data, with SNR at 7T higher than the other field strengths by an amount greater than predicted from the field increment alone [43]. A number of additional authors have combined SENSE with DTI in the whole brain at 3T [44-46], observing reduced T2* effects and distortions at resolutions as low as 0.8x0.8x3 mm^3. Similar findings were obtained at 2T in 50 diffusion weighted brain slices using a half-fourier acquisition approach to obtain 1.5 mm isotropic data [47].

For spinal cord diffusion imaging, imaging accelerations were primarily achieved using reduced-FOV methods without EPI. At 1.5T, Saritas obtained axial images with 0.62x0.62x5 mm^3 resolutions [27], and at 3T, Finsterbush achieved 0.5x0.5x5 mm^3 [26], both using an IVI technique with a 2D selective RF pulse. 7T results are confined to anatomical imaging only, with preliminary images by Sigmund demonstrating 180 and 220 μm at a 3 mm slice thicknesses without using reduced-FOV methods [48]. The images provided excellent grey and white matter contrast using a single surface coil with resolutions exceeding recent 600 μm results obtained

with a 32 channel spine and brain array at 3T [49]. However, shading and distortion artifacts were apparent in the high-resolution 7T results using a TSE scan.

Overall, the human studies performed to date indicate that 7T supports acquisitions targeting resolutions previously not attainable at lower field strengths, with distinctions specifically shown against 1.5T and 3T. In some cases, this was accomplished with reasonable scan times ranging from approximately 3 to 10 minutes. However, a number of these investigations required as much as 1024x1024 points to achieve the resolutions targeted, with artifacts reported near regions of high susceptibility variation. In general, scan times appeared to be minimized by applying primarily a gradient echo susceptibility weighted sequence with short TR and TE less than 25 ms. Spin echo scans were less common and of those, primarily proton density weighted. EPI scans suggested higher resolutions than similar 3T studies, but lower than the anatomical scans described at and greater than 0.5 mm isotropic. As indicated by the postmortem imaging results, resolutions beyond the *in vivo* human imaging studies required scan times measured in hours versus minutes. For a number of studies, investigation was localized to regions much smaller than the full FOV size such as the hippocampus and motor areas, necessitating the large data array sizes. The results indicated the benefits of data reduction using parallel imaging, partial fourier methods, and reduced-FOV techniques at 3T and lower field, diminishing artifacts and scan times for anatomical, functional, and DTI based imaging studies.

16. Summary

In sum, improvement in MRI resolution beyond prior investigations that approaches histological quality remains a realistic and worthwhile goal for clinical and research based human studies. A variety of potential solutions exist that combat the current challenges faced when obtaining high-resolution data. Reduced-FOV imaging, in particular, enables the imaging experiment to focus on the target anatomy of interest, restricting the amount of data required to achieve a specific resolution. This results in scan time reduction, lowering of time-based artifacts induced by susceptibility, motion, and physiological effects, while simultaneously enabling improvement in temporal resolution for functional studies.

Combined with the use of ultra-high field strengths such as 7T, the potential exists for high resolutions to be obtained in a variety of human studies, to improve image quality for resolutions currently achieved, or to reduce overall scan durations. In the area of human brain imaging, both anatomical and functional localization, as well as feature contrast will potentially benefit from the improvement in obtained information, ultimately leading to progress in the diagnosis, understanding, and treatment of pathologies and disease. As such, demonstrating and advancing reduced-FOV methods for human imaging at ultra-high field strength serves as the focus of the specific aims of this work.

17. References

[1] E.M. Haacke, Magnetic resonance imaging : physical principles and sequence design, J. Wiley & Sons, New York, 1999.

[2] M.A. Bernstein, K.F. King, X.J. Zhou, Handbook of MRI pulse sequences, Elsevier Academic Press, Burlington, MA, 2004.

[3] P.J. Basser, C. Pierpaoli, Microstructural and physiological features of tissues elucidated by quantitative-diffusion-tensor MRI, Journal of magnetic resonance. Series B, 111 (1996) 209-219.

[4] O.F. Haase A, Kienlin V, et. al., NMR Probeheads for In Vivo Applications, Concepts in Magnetic Resonance Part B (Magnetic Resonance Engineering), 12 (2000) 361-388.

[5] J. Mispelter, M. Lupu, A. Briguet, NMR probeheads for biophysical and biomedical experiments : theoretical principles & practical guidelines, Imperial College Press ;Distributed by World Scientific, LondonHackensack, NJ, 2006.

[6] A.M. Aisen, G.M. Glazer, P.L. Carson, D.O. Hearshen, Motion artifacts in quantitative magnetic resonance imaging, Magn Reson Imaging, 4 (1986) 207-213.

[7] M.L. Wood, R.M. Henkelman, MR image artifacts from periodic motion, Med Phys, 12 (1985) 143-151.

[8] Y. Xu, E.M. Haacke, Partial Fourier imaging in multi-dimensions: a means to save a full factor of two in time, Journal of magnetic resonance imaging : JMRI, 14 (2001) 628-635.

[9] M. Lustig, D. Donoho, J.M. Pauly, Sparse MRI: The application of compressed sensing for rapid MR imaging, Magn Reson Med, 58 (2007) 1182-1195.

[10] K.P. Pruessmann, M. Weiger, M.B. Scheidegger, P. Boesiger, SENSE: sensitivity encoding for fast MRI, Magn Reson Med, 42 (1999) 952-962.

[11] M. Weiger, K.P. Pruessmann, C. Leussler, P. Roschmann, P. Boesiger, Specific coil design for SENSE: a six-element cardiac array, Magn Reson Med, 45 (2001) 495-504.

[12] F. Wiesinger, P.F. Van de Moortele, G. Adriany, N. De Zanche, K. Ugurbil, K.P. Pruessmann, Potential and feasibility of parallel MRI at high field, NMR Biomed, 19 (2006) 368-378.

[13] D.A. Feinberg, J.C. Hoenninger, L.E. Crooks, L. Kaufman, J.C. Watts, M. Arakawa, Inner volume MR imaging: technical concepts and their application, Radiology, 156 (1985) 743-747.

[14] C.J. Hardy, et al, Spatial Localization in Two Dimensions Using NMR Designer Pulses, Journal of Magnetic Resonance, 82 (1989) 647-654.

[15] J. Pauly, et al, A k-space Analysis of Small-Tip-Angle Excitation, Journal of Magnetic Resonance, 81 (1989) 43-56.

[16] J. Finsterbusch, Fast-spin-echo imaging of inner fields-of-view with 2D-selective RF excitations, J Magn Reson Imaging, 31 1530-1537.

[17] E.K. Jeong, S.E. Kim, J. Guo, E.G. Kholmovski, D.L. Parker, High-resolution DTI with 2D interleaved multislice reduced FOV single-shot diffusion-weighted EPI (2D ss-rFOV-DWEPI), Magn Reson Med, 54 (2005) 1575-1579.

[18] D. Mitsouras, R.V. Mulkern, F.J. Rybicki, Strategies for inner volume 3D fast spin echo magnetic resonance imaging using nonselective refocusing radio frequency pulses, Med Phys, 33 (2006) 173-186.

[19] P.A. Bottomley, Selective Volume Method for Performing Localized NMR Spectroscopy, in, General Electric Company, United States, 1984.

[20] J. Frahm, H. Bruhn, M.L. Gyngell, K.D. Merboldt, W. Hanicke, R. Sauter, Localized high-resolution proton NMR spectroscopy using stimulated echoes: initial applications to human brain in vivo, Magn Reson Med, 9 (1989) 79-93.

[21] J. Frahm, W. Hanicke, H. Bruhn, M.L. Gyngell, K.D. Merboldt, High-speed STEAM MRI of the human heart, Magnetic resonance in medicine : official journal of the Society of Magnetic Resonance in Medicine / Society of Magnetic Resonance in Medicine, 22 (1991) 133-142.

[22] B.J. Wilm, J. Svensson, A. Henning, K.P. Pruessmann, P. Boesiger, S.S. Kollias, Reduced field-of-view MRI using outer volume suppression for spinal cord diffusion imaging, Magn Reson Med, 57 (2007) 625-630.

[23] P. Le Roux, R.J. Gilles, G.C. McKinnon, P.G. Carlier, Optimized outer volume suppression for single-shot fast spin-echo cardiac imaging, J Magn Reson Imaging, 8 (1998) 1022-1032.

[24] Y. Luo, R.A. de Graaf, L. DelaBarre, A. Tannus, M. Garwood, BISTRO: an outer-volume suppression method that tolerates RF field inhomogeneity, Magn Reson Med, 45 (2001) 1095-1102.

[25] J. Pfeuffer, P.F. van de Moortele, E. Yacoub, A. Shmuel, G. Adriany, P. Andersen, H. Merkle, M. Garwood, K. Ugurbil, X. Hu, Zoomed functional imaging in the human brain at 7 Tesla with simultaneous high spatial and high temporal resolution, Neuroimage, 17 (2002) 272-286.

[26] J. Finsterbusch, High-resolution diffusion tensor imaging with inner field-of-view EPI, J Magn Reson Imaging, 29 (2009) 987-993.

[27] E.U. Saritas, C.H. Cunningham, J.H. Lee, E.T. Han, D.G. Nishimura, DWI of the spinal cord with reduced FOV single-shot EPI, Magn Reson Med, 60 (2008) 468-473.

[28] G. Soria, M. De Notaris, R. Tudela, G. Blasco, J. Puig, A.M. Planas, S. Pedraza, A. Prats-Galino, Improved Assessment of Ex Vivo Brainstem Neuroanatomy With High-Resolution MRI and DTI at 7 Tesla, Anat Rec (Hoboken), 294 (2011) 1035-1044.

[29] S. Geyer, M. Weiss, K. Reimann, G. Lohmann, R. Turner, Microstructural Parcellation of the Human Cerebral Cortex - From Brodmann's Post-Mortem Map to in vivo Mapping with High-Field Magnetic Resonance Imaging, Front Hum Neurosci, 5 (2011) 19.

[30] U.C. Wieshmann, M.R. Symms, J.P. Mottershead, D.G. MacManus, G.J. Barker, P.S. Tofts, T. Revesz, J.M. Stevens, S.D. Shorvon, Hippocampal layers on high resolution magnetic resonance images: real or imaginary?, J Anat, 195 (Pt 1) (1999) 131-135.

[31] J.C. Augustinack, A.J. van der Kouwe, M.L. Blackwell, D.H. Salat, C.J. Wiggins, M.P. Frosch, G.C. Wiggins, A. Potthast, L.L. Wald, B.R. Fischl, Detection of entorhinal layer II using 7Tesla [corrected] magnetic resonance imaging, Ann Neurol, 57 (2005) 489-494.

[32] Y. Ge, V.M. Zohrabian, R.I. Grossman, Seven-Tesla magnetic resonance imaging: new vision of microvascular abnormalities in multiple sclerosis, Arch Neurol, 65 (2008) 812-816.

[33] K. Kollia, S. Maderwald, N. Putzki, M. Schlamann, J.M. Theysohn, O. Kraff, M.E. Ladd, M. Forsting, I. Wanke, First clinical study on ultra-high-field MR imaging in patients with multiple sclerosis: comparison of 1.5T and 7T, AJNR Am J Neuroradiol, 30 (2009) 699-702.

[34] E.C. Tallantyre, P.S. Morgan, J.E. Dixon, A. Al-Radaideh, M.J. Brookes, P.G. Morris, N. Evangelou, 3 Tesla and 7 Tesla MRI of multiple sclerosis cortical lesions, Journal of magnetic resonance imaging : JMRI, 32 (2010) 971-977.

[35] J.M. Theysohn, O. Kraff, S. Maderwald, M.U. Schlamann, A. de Greiff, M. Forsting, S.C. Ladd, M.E. Ladd, E.R. Gizewski, The human hippocampus at 7 T--in vivo MRI, Hippocampus, 19 (2009) 1-7.

[36] Z.H. Cho, H.K. Min, S.H. Oh, J.Y. Han, C.W. Park, J.G. Chi, Y.B. Kim, S.H. Paek, A.M. Lozano, K.H. Lee, Direct visualization of deep brain stimulation targets in Parkinson disease with the use of 7-tesla magnetic resonance imaging, J Neurosurg, 113 (2010) 639-647.

[37] A. Abosch, E. Yacoub, K. Ugurbil, N. Harel, An assessment of current brain targets for deep brain stimulation surgery with susceptibility-weighted imaging at 7 tesla, Neurosurgery, 67 (2010) 1745-1756; discussion 1756.

[38] T. Breyer, I. Wanke, S. Maderwald, F.G. Woermann, O. Kraff, J.M. Theysohn, A. Ebner, M. Forsting, M.E. Ladd, M. Schlamann, Imaging of patients with hippocampal sclerosis at 7 Tesla: initial results, Acad Radiol, 17 421-426.

[39] O. Speck, J. Stadler, M. Zaitsev, High resolution single-shot EPI at 7T, Magma, 21 (2008) 73-86.

[40] B.A. Poser, P.J. Koopmans, T. Witzel, L.L. Wald, M. Barth, Three dimensional echo-planar imaging at 7 Tesla, Neuroimage, 51 (2010) 261-266.

[41] J.J. Zwanenburg, M.J. Versluis, P.R. Luijten, N. Petridou, Fast high resolution whole brain T2* weighted imaging using echo planar imaging at 7T, Neuroimage, 56 (2011) 1902-1907.

[42] R.M. Heidemann, D.A. Porter, A. Anwander, T. Feiweier, K. Heberlein, T.R. Knosche, R. Turner, Diffusion imaging in humans at 7T using readout-segmented EPI and GRAPPA, Magnetic resonance in medicine : official journal of the Society of Magnetic Resonance in Medicine / Society of Magnetic Resonance in Medicine, 64 (2010) 9-14.

[43] D.L. Polders, A. Leemans, J. Hendrikse, M.J. Donahue, P.R. Luijten, J.M. Hoogduin, Signal to noise ratio and uncertainty in diffusion tensor imaging at 1.5, 3.0, and 7.0 Tesla, Journal of magnetic resonance imaging : JMRI, 33 (2011) 1456-1463.

[44] K.M. Hasan, A. Kamali, L.A. Kramer, Mapping the human brain white matter tracts relative to cortical and deep gray matter using diffusion tensor imaging at high spatial resolution, Magn Reson Imaging, 27 (2009) 631-636.

[45] T. Jaermann, G. Crelier, K.P. Pruessmann, X. Golay, T. Netsch, A.M. van Muiswinkel, S. Mori, P.C. van Zijl, A. Valavanis, S. Kollias, P. Boesiger, SENSE-DTI at 3 T, Magn Reson Med, 51 (2004) 230-236.

[46] T.K. Truong, B. Chen, A.W. Song, Integrated SENSE DTI with correction of susceptibility- and eddy current-induced geometric distortions, Neuroimage, 40 (2008) 53-58.

[47] J.J. Wang, R. Deichmann, R. Turner, R. Ordidge, 3D DT-MRI using a reduced-FOV approach and saturation pulses, Magnetic resonance in medicine : official journal of the Society of Magnetic Resonance in Medicine / Society of Magnetic Resonance in Medicine, 51 (2004) 853-857.

[48] E.E. Sigmund, C. Hu, G. Suero, J. Helpern, High resolution anatomical imaging of the spinal cord at 7 T, in: Proc. Intl. Soc. Magn. Reson., Stockholm, Sweden, 2010, pp. 449.

[49] J. Cohen-Adad, A. Mareyam, B. Keil, J.R. Polimeni, L.L. Wald, 32-Channel RF coil optimized for brain and cervical spinal cord at 3 T, Magnetic resonance in medicine : official journal of the Society of Magnetic Resonance in Medicine / Society of Magnetic Resonance in Medicine, (2011).

CHAPTER III

SPECIFIC AIMS

1. SPECIFIC AIM 1

The primary objective of this aim is to develop and compare multiple reduced-FOV methods for use at 7 Tesla to determine the optimal approach for ultra-high field, high resolution imaging in the human. Relative performance will be based on the ability to locally excite target regions, suppress unwanted signal, minimize power deposition, produce superior or comparable SNR in localized regions, and prevent artifacts caused by the selective pulses or fold-over of unsuppressed signal. Behavior and optimization in the presence of high B1 and susceptibility variation at 7T are also of consideration, as well as relative performance between techniques when used with multi-slice protocols. Ideal methods would demonstrate consistent ability to reduce the FOV for a variety of target FOV sizes, orientations, and subjects, while providing flexibility in imaging parameters and use of sequence types to achieve various contrast weightings. This analysis will show optimization at 7T, demonstrate relative performance, and serve as the basis for the applied techniques used in the subsequent aims that are focused on *in vivo* human imaging.

2. SPECIFIC AIM 2

In this aim, the optimized methods determined from the relative comparison in the first aim will be applied to obtain high resolution images in the human brain. The primary goal is to achieve reduced scan times and comparable or superior image

quality to full-FOV acquisitions with resolutions targeted in the range of 160 μm to 500 μm. Here, the resolutions achieved would represent the highest published to date using a 7T or lower field system. Along with reduced-FOV, the aim explores a combination of rapid imaging techniques including EPI and SENSE based parallel imaging to obtain the highest accelerations possible. Relative benefits of these approaches to obtain high quality images devoid of artifacts and blurring with maximized SNR will be explored, with comparison against traditional full-FOV scans. Performance across resolutions with T2 and T2* weighting using highly accelerated single slice, multi-slice, and 3D volume image sets will also be explored. Additional comparisons will be made to demonstrate the benefits of the highly accelerated reduced-FOV protocol to achieve reduced artifacts using single and multi-shot EPI protocols across a range of target resolutions. Improvements in feature visibility and contrast will be investigated at the maximal resolutions accomplished in this aim.

3. SPECIFIC AIM 3

In the final aim, the optimized human reduced-FOV imaging protocol will be applied for localized DTI and spinal cord imaging applications that are highly sensitive to motion and susceptibility artifacts. Use of accelerated imaging approaches will be applied to achieve high resolution acquisitions and demonstrate a reduction in artifacts as a result of obtaining smaller data set sizes in a localized FOV. Specific targeting of regions previously only imaged in full-FOV scans will be performed throughout the brain to measure diffusion properties, with comparison at multiple resolutions and isolated to specific tract features. Spinal cord imaging will attempt 300 to 500 μm resolutions localized to the cervical region.

CHAPTER IV

COMPARISON OF REDUCED-FOV TECHNIQUES FOR 7 TESLA IMAGING

ABSTRACT

A comprehensive analysis of a variety of reduced-FOV techniques suitable for 7T imaging has been performed. STEAM, PRESS, OVS, BISTRO, and multiple versions of IVI were each implemented, optimized and tested. IVI approaches included a standard spin echo method, the implementation of a composite RF pulse to address effects of B_1 inhomogeneities, use of a two dimensional Gaussian RF pulse for excitation along a spiral trajectory, and a double off-slice excitation method to diminish multi-slice losses. Comparisons between methods focused on measurements of relative signal to noise ratio (SNR), power deposition (specific absorption rate, SAR), suppression of unwanted signal, artifact strength and prevalence, and sensitivity to B_1 variation in slabs and small FOV excitations. Additionally, qualitative comparisons were performed between *in vivo* human scans. Multi-slice performance was assessed for STEAM, PRESS, and IVI by simulating the expected impact on signal in out-of-slice locations with various methods and pulse orders. The predictions were verified experimentally, and potential solutions explored to diminish measured losses. The ability to scale RF pulses applied in reduced-FOV methods to correct for B_1 inhomogeneities was also demonstrated.

The combined results provide a basis for optimization and application of reduced-FOV techniques for imaging small inner volumes with high spatial resolution at 7T.

1. INTRODUCTION

Increments in magnetic field strengths to 7T and beyond theoretically provide an increase in signal that may be used to improve image resolution in MRI. However, high-resolution imaging necessitates that a large array of data be acquired dependent on the object size. Longer image acquisition times constrain the temporal resolution for functional studies, result in greater occurrence of physiological and motion based artifacts, signal blurring, distortion, and dropout induced by susceptibility effects, especially for single-shot EPI type scans. A number of solutions have been developed to reduce scan times for applications sensitive to these effects. Multi-channel receive arrays combined with parallel imaging methods such as SENSE and GRAPPA enable undersampling of phase encoded data typically by a factor of two to four in human studies [1, 2]. Surface coils constrain the signal intensity to localized regions to restrict overall FOV sizes and scan durations [3]. Partial Fourier methods rely on k-space symmetry to reduce the amount of data required to reconstruct an image [4, 5]. Recent efforts in compressed sensing use intrinsic MRI data set sparsity to incoherently sample a limited number of image points [6]. By contrast, reduced-FOV (rFOV) methods restrict signal excitation to smaller regions in order to lower acquisition times [7-21].

Common to all of these methods is an intrinsic reduction in the sampling pattern that corresponds to a FOV size smaller than the object dimensions. Typically, this induces an aliasing or fold-over artifact because the Nyquist sampling criteria are not satisfied. The solution to the aliasing problem distinguishes these methods; accomplished either through proper encoding of data to calculate missing k-space information or by suppressing signal that would induce this artifact. In all cases, SNR is diminished in order to achieve the desired acceleration, which must be weighed against the diminished artifacts or improved efficiency, and the ability of the method to address aliasing without causing fold-over effects.

Reduced-FOV imaging has been explored previously and may be implemented using various techniques that each exploit the spatial selectivity of RF pulses combined with a gradient to restrict excitation of spins to localized volumes. Selective excitation can be extended beyond the simple slice selection exploited in conventional imaging by also restricting effects along the phase encoding or readout dimensions. The approaches used to achieve this may be generally divided into two categories: selective excitation methods that use multiple pulses for volume localization using methods such as STEAM, PRESS, and IVI [7, 12, 22, 23], and suppression-based methods that apply bands to saturate signal external to the target FOV such as OVS and BISTRO [15, 16]. Additional permutations have been developed to address losses in SNR caused by the excitation methods in out-of-slice locations for multislice scans [10, 11, 13]. The performance for all techniques has largely been demonstrated at field strengths from 0.35 T to 3 T.

The challenges with all these methods are a combination of decreased SNR due to smaller FOV (and, usually, voxel) sizes, the need for adequate suppression of signals from outside the FOV to prevent residual aliasing artifacts, restrictions on the imaging sequences that can be used to achieve a desired contrast, the introduction of additional RF pulses that increase power deposition (specific absorption rate, SAR), and the relative scan efficiency compared to other approaches. With increased use of 7T human systems, the application of these methods and various other rapid imaging sequences may be more justified in order to achieve smaller voxel sizes and improve spatial resolution beyond that readily achievable with lower field systems. However, 7T introduces a number of other field dependent challenges, such as increased B_1 inhomogeneity, higher power deposition (SAR), and changes in relaxation parameters. The combination of these factors necessitates a revised optimization of reduced-FOV imaging methods previously implemented at lower fields to fully benefit from their application in high-resolution high field imaging. Here, we demonstrate how a variety of reduced-FOV techniques potentially of interest for 7T studies may be implemented and optimized, with a critical comparison performed using STEAM, PRESS, OVS, BISTRO, and IVI. Specific emphasis is placed on evaluations of the relative achieved SNR, suppression of unwanted signal, achieved SAR, residual artifacts, sensitivity to and correction of B_1 variations, and applicability with multi-slice protocols.

2. METHODS

2.1. STEAM Selective Excitation Method

The Stimulated Echo Acquisition Mode (STEAM) technique was implemented by the sequence shown in figure 4.1 to achieve reduced-FOV imaging based on the description provided by Frahm [12, 24]. Localization for this method relies on the subsequent application of multiple 90° RF pulses and gradient pairings to restrict excited signal to within a specific volume of interest, with three pulses applied sequentially to affect different dimensions independently. For this implementation, the order of pulses was set to perform excitation along the phase encoding dimension first, followed by readout and then slice selection. To optimize STEAM for reduced-FOV imaging at 7T, various pulse shapes were empirically explored for the selective pulses applied in the phase encoding and readout dimensions. Specific emphasis was placed on minimization of ripple effects in the pulse passband and sidelobe regions, achieving a sharp roll-off, confining the pulse duration to less than 6 ms for a 90° flip angle, and demonstrating an appearance in the excited region consistent with that obtained using a spin echo sequence and no STEAM preparation. In this case, the optimal pulse was determined to be a five-lobe SINC with a 15 μT amplitude and a 3.92 ms duration. Spoiling gradients after readout were matched with those between the first two pulses and separated by half the echo time to form the desired stimulated echo centered on the acquisition window. All three spoilers were maximized to the 40 mT/m system limit with a 4 ms duration that was determined to establish sufficient dephasing to minimize residual signal in

the sideband regions. Based on the applied pulse shape and spoiling gradient durations, the pulse 'mixing time' delay, TM, was 11.38 ms. The STEAM preparation was performed prior to the imaging sequence gradients, with a loss of half of the SNR expected due to the stimulated echo only refocusing half of the magnetization.

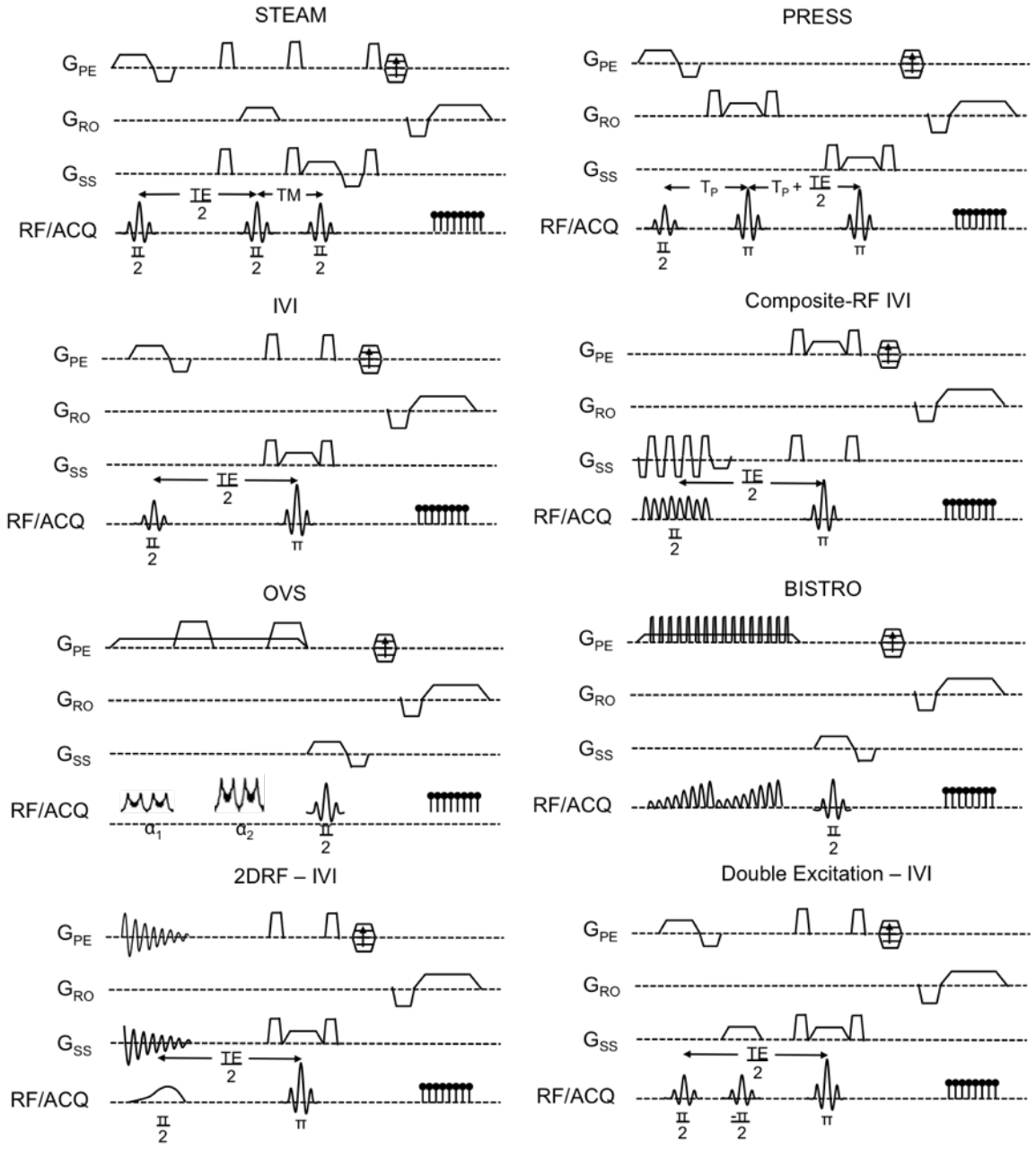

Figure 4.1 - Pulse sequence diagrams for applied reduced-FOV imaging methods: STEAM, PRESS, IVI, IVI with composite RF pulse to address B1 inhomogeneity, OVS, BISTRO, IVI using 2D RF spiral Gaussian excitation, and IVI with double off-slice excitation to address multi-slice imaging losses (used for simulation only).

2.2. PRESS Selective Excitation Method

Point Resolved Spectroscopy (PRESS) for reduced-FOV imaging was implemented following the description provided by Bottomley [7] adapted for imaging. As with STEAM, PRESS uses three pulses to localize the excited signal, in this case, a 90° excitation followed by two 180° refocusing pulses, with the order of the pulse directions the same as STEAM. The complete PRESS combination ensures that only those regions that have experienced all three pulses will have refocused and unspoiled signal at acquisition. A similar optimization of the pulse definitions was performed here to define the refocusing pulses, which required an alternate shape due to the expected bandwidth narrowing that would occur with a SINC when increased to a 180° flip angle. For this implementation, pulses optimized for spin echo refocusing with short echo times as defined in the scanner library were applied for both 180° pulses. Each was specified to have 15 μT amplitudes and 5.40 ms durations with the shape based on observed minimization of ripple effects and sharp excitation boundaries. Symmetrical crushers surrounding both refocusing pulses were matched with 40 mT/m amplitudes and 4 ms durations as used for spoiling in the STEAM sequence. For the initial phase encoding excitation, the previously optimized five-lobe SINC was applied. The duration between the excitation and the first refocusing pulse was minimized based on the RF pulse, gradient refocusing, and spoiler lengths, for a total pulse delay of 10.98 ms.

2.3. OVS Saturation Band Method

The Outer-Volume Suppression (OVS) technique [21] was implemented using two repetitions of RF pulses combined with gradients to saturate regions outside a

targeted FOV in the phase encoding direction. The pulse RF frequencies were set to target regions on either side of the desired imaging FOV. To prevent overlap of these regions with the target image FOV, the frequency offsets were defined as:

$$\Delta f_o = \pm BW_{RF} / \left(\left(w_{slab} - \frac{w_{rfov}}{2} \right) \cdot G_{PE} \cdot \gamma \right) \quad 4.1$$

The excited signals produced from the outer volume were then suppressed using large spoiling gradients after each repetition of the OVS pulses. The widths of the outer suppressed regions, w_{slab}, were set to 10 cm using a frequency modulated RF pulse from the scanner pulse library that had a linear phase profile, with a 90° flip angle for the first pair of pulses and 160° for the second, labeled α_1 and α_2, respectively (fig. 4.1). Peak B_1 amplitudes for each pulse were 8.32 μT and 15 μT, with 8.63 ms durations. The angles were empirically determined based on minimization of OVS band suppression in an FBIRN phantom, with angles iteratively adjusted from an initial 90°/90° combination. Applied spoiling gradient amplitudes were similarly optimized to 40 mT/m, 16 ms in length, corresponding to the maximum system gradient limit, with the duration empirically adjusted to visibly diminish fold-over artifacts in a reduced-FOV phantom scan. To assist with intra-pulse spoiling, a single slice selective gradient was used for all suppression band pulses, with a total OVS duration of 76 ms.

2.4. BISTRO Saturation Band Method

As with OVS, B_1 Insensitive Train to Obliterate Signal (BISTRO) localizes signal by establishing suppression bands outside the targeted FOV [16]. The technique uses a sequence of adiabatic hyperbolic secant pulses with amplitudes scaled by half a secant profile to diminish sensitivities of the suppression to B_1

inhomogeneity. Significant B_1 variations would result in poor suppression and aliasing of residual signal into target regions. The implementation of BISTRO developed here used eight hyperbolic secant pulses each having a 5.6 ms duration with a 15 μT amplitude for the eighth pulse. The remaining in a train of N pulses are scaled using the specified max amplitude, $B_{1,N}$, and a secant profile β value of 4:

$$B_{1,n} = B_{1,N} \cdot \mathrm{sech}[\beta \cdot (1 - n(t)/N)] \quad 4.2$$

A single phase encoding gradient was used to establish a 10 cm wide suppression slab, with the secant train repeated twice to define slabs on both sides of the target volume. The pulse frequency modulation was inverted every alternate pulse to help minimize unwanted echo formation. Additional spoiling gradients were placed between each individual pulse with amplitudes of 35 mT/m and duration of 1 ms for additional signal dephasing, with an overall BISTRO duration of 103 ms.

2.5. IVI Method 1 – Spin Echo Selective Excitation

Inner-Volume Imaging (IVI) was implemented as first described by Feinberg [9]. With IVI, the number of combined pulses used is reduced to two versus the STEAM and PRESS methods, restricting excitation along the phase encode and slice directions only. The combination of pulses ensures spins are appropriately refocused at acquisition only for a volume that experienced both. This implementation of IVI differs from that described previously [9] by initiating with a phase-encoding excitation. Pulse shape and duration were optimized using the same analysis performed for STEAM and PRESS to define the 90° phase-encoding direction excitation and the 180° slice selection refocusing pulse, which consisted of a five-lobe SINC with a 15 μT amplitude and 3.92 ms duration, and a scanner pulse

optimized for spin echo refocusing with a 15 μT amplitude and 5.40 ms duration, respectively. The time between excitation and refocusing was set to half the echo time, with crusher gradients matched at a 40 mT/m strength and a 4 ms duration.

2.6. IVI Method 2 - 2D RF Pulse for Spiral Gaussian Excitation

Simultaneous selective excitations in both the phase encoding and slice select directions were accomplished using a modified IVI technique that replaced the initial selective 90° excitation with a two-dimensional RF pulse. Previous applications of this 2D RF approach have been developed to minimize the impact to off-slice locations by restricting excitation to the target slice [8, 10, 11, 14, 17, 19]. For this implementation, the target excitation profile followed the formulation described by Pauly and Hardy [13, 25], and comprised a 2D Gaussian in the x-z plane excited along a spiral trajectory. For any underlying magnetization, ρ($\vec{r}$) that contributes to the image, a weighting function, W($\vec{r}$) can be defined with a value of 1 to localize signal within a specified dimensional constraint, which Fourier transforms into its spatial frequency form, W(K):

$$\mathcal{F}\{W(\vec{r}) \cdot \rho(\vec{r})\} \Longrightarrow W(K) * P(K) \qquad 4.3$$

W provides the phase and amplitude information for each spatial frequency necessary to establish the desired excitation pattern, and can be discretely and temporally sampled along a specific k-space trajectory, S(t):

$$W\{K(t)\} = W(K) \cdot S(t) \qquad 4.4$$

The trajectory through excitation k-space can take a number of forms, including cartesian, spiral, or blipped EPI type trajectories [10, 11, 17]. The target k-space points are translated into a time-varying gradient waveform for both dimensions,

G(t), and then combined with the weighting information, W{K(t)}, to define the necessary $B_1(t)$ function that will achieve the target spatial pattern:

$$B_1(t) = W\{K(t)\} \cdot |G(t)| \quad 4.5$$

For the purposes of this study, the target excitation pattern was a 2D Gaussian with distinct σ_z and σ_x values to enable compression and extension along both the phase encode and slice select dimensions, scaled by α to achieve a specific flip angle:

$$W\{K(t)\} = \alpha \cdot e^{-\beta^2\left(\frac{k_z^2}{\sigma_z^2}+\frac{k_x^2}{\sigma_x^2}\right)} \quad 4.6$$

For this implementation, σ_y and σ_z where selected to be 1.2 and 1.5, respectively for a narrower Gaussian dimension in the slice dimension, which achieved a full-width-half-max (FWHM) value of 45.9 mm and 37.2 mm respectively. This pattern was sampled using an eight-pass spiral with maximum gradient strength of 8 mT/m that terminates at a (k_x,k_z) = (0,0) to ensure the pulse is self-refocusing. The corresponding $B_1(t)$ calculated from this trajectory and target pattern had a peak amplitude of 2.5 μT and a duration of 6.4 ms to achieve a 90° flip angle. The Gaussian excitation was followed by a slice selective 180° RF pulse as per the IVI method between matched crusher gradients.

2.7. IVI Method 3 - Composite RF Pulse for Uniform Excitation

Methods that compensate for the spatial variations in achieved flip angles caused by B_1 inhomogeneities at high field strengths have recently been described using composite RF pulses optimized for uniform excitation over a range of typical ΔB_0 and B_1^+ values [26, 27]. These composite pulses are constructed using a specific number of pulses of either block or Gaussian profiles each with fixed and matched durations. A minimization algorithm is applied to iteratively adjust the

individual pulse amplitudes and phases. The achieved flip angles at each iteration point are determined within specific ΔB_0 and B_1^+ limits and compared against a target angle to calculate the error in the established angle at any spatial location. Local minimization is achieved when the incremental difference in the updated and target angle is below a specified threshold. The applied non-linear constrained minimization algorithm takes into account maximum B_1 and pulse duration constraints based on MR hardware, with the range of ΔB_0 and B_1^+ defined from values measured in human brain and phantoms at 7T.

This technique was applied to replace the selective SINC pulse executed at the start of the IVI reduced-FOV imaging sequence to achieve localization and uniform excitation [27]. In this case, the pulse was altered to be slice selective followed by a phase encoding selective 180° refocusing pulse. Eight pulses each with a Gaussian profile were chosen for the RF pulse composite definition assuming a maximum B_1 amplitude of 15 μT and 1.06 ms duration for each individual pulse. Slice selection employed trapezoidal gradients during each composite element in the train with a strength of 22 mT/m to achieve a target 3 mm slice thickness, and a positive and negative amplitude alteration between neighboring sub-pulses. An additional refocusing gradient followed the composite train prior to the phase encode selective refocusing pulse between crusher gradients with 40 mT/m strength and 4 ms duration. As with the standard IVI, the duration between the composite and 180° refocusing pulse was half the echo time taken from the center point of the pulse train. After optimization, the entire duration of the composite RF pulse was 12 ms.

2.8. IVI Method 4 - Small FOV RF Scaling to Reduce B_1 Inhomogeneity Signal Loss

Additional corrections for B_1 inhomogeneity effects in IVI, which take advantage of the small dimensions relevant for reduced-FOV experiments, were investigated. For a given object which experiences an RF pulse, the resulting flip angle distribution within a target plane has a measurable and predictable pattern dependent on the object shape and RF frequency, with localized regions of peak and diminished intensity. Figure 4.2A depicts the pattern observed in a 17 cm agar gel phantom using a standard SE sequence, and the measured profile (fig. 4.2B). Within restricted regions of the object, the total variation can potentially be much less than that experienced across the whole object, as demonstrated in regions 1 and 2. For the purposes of reduced-FOV imaging, correction of inhomogeneity concerns itself with only addressing the variation experienced in the localized region. If the overall flip angle measured in a target area are reasonably uniform but too low or high, an RF scaling adjustment may be sufficient to compensate for corresponding

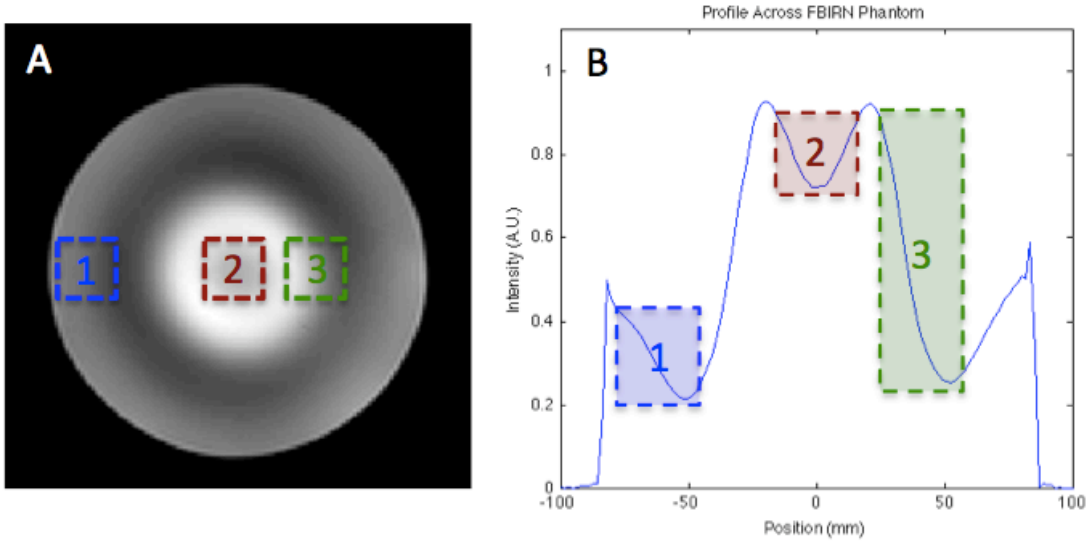

Figure 4.2 – A.) Agar gel phantom SE image with regions depicting three inhomogeneity areas. B.) Profile of phantom image through center with regions identified demonstrating relative signal variation in each voxel.

signal loss in those locations by a factor unique to that area. In the case of human or phantom imaging, the nature of the inhomogeneity potentially reduces to a small set of necessary scaling factors to address: 1.) low flip angle regions (area 1) 2.) high flip angle regions (area 2), and 3.) transitions between the two (area 3). To investigate the potential for signal recovery by RF scaling in small regions, IVI was implemented to enable adjustment of both its excitation and refocusing pulses.

2.9. IVI Method 5 – Double Off-Slice Excitation for Improved MS Performance

Reduced-FOV methods that rely on the intersection of excitation planes along each dimension such as STEAM, PRESS, and IVI, are known to adversely affect off-slice positions for interleaved, multi-slice scans. This occurs particularly when excitation or refocusing pulses are used to accomplish localization in the phase encoding dimension. The off-slice spins experience these pulses, which perturb magnetization at these positions. Full recovery of this magnetization for subsequent scans of those slice locations is required to ensure maximal signal from the slice, and the recovery is dependent on the T_1 relaxation times. Increasing the number of slices interleaved in an MS scan will produce additional losses for each slice.

To address this, IVI was modified to apply a second excitation pulse with a -90° flip angle immediately after the initial excitation is gradient refocused (fig. 4.1). The additional pulse is selective in the slice direction and acts on the off-slice location only. This restores longitudinal magnetization, enabling T_1 recovery during the remainder of the interleave without impacting the current slice localization. Depending on the interleave sampling pattern, the position of the additional excitation can be localized to the next slice only, or to a block of off-slice positions in

ascending or descending patterns where the remaining slices reside on only one side of the current interleave slice location (fig. 4.3). The feasibility of this technique to address MS signal losses was characterized in simulations described in the subsequent experimental methods.

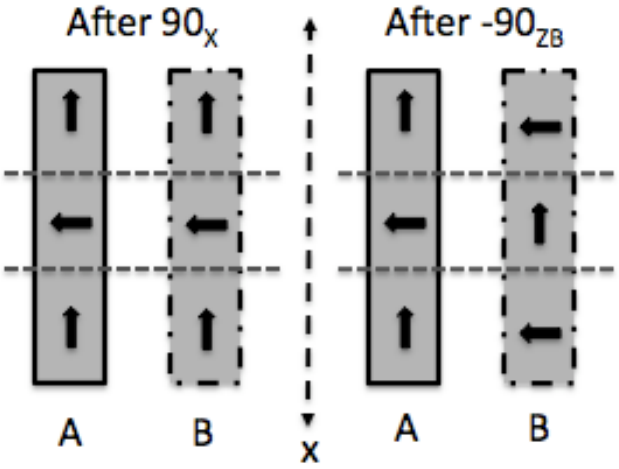

Figure 4.3 – Spin impact for proposed double excitation approach to address off-slice signal loss with IVI for MS scans. A and B depict two distinct slice locations, A corresponding to the current imaging slice, B the out of slice position. After the initial 90_X, spins in all slices are tipped in the transverse plane. A subsequent -90_Z acting only on the off-slice position restores longitudinal magnetization in the target voxel.

3. EXPERIMENTAL METHODS

3.1. Phantom Experiments Configuration

Comparisons between these methods were performed using a 60 cm bore Philips 7T Achieva system (Philips Healthcare, Best, The Netherlands) with a 32 channel Nova parallel head array for reception (Nova Medical, Wilmington, MA), and a single channel volume coil for transmission. The system has a maximum gradient strength, slew rate, and coil peak B_1 amplitude of 40 mT/m, 200 mT/m/ms, and 15 μT, respectively. Phantom experiments were performed using a 17 cm spherical agar gel FBIRN (Functional Biomedical Information Research Network) [28].

3.2. Comparison 1 – Method Slab Excitations

The implemented reduced-FOV methods were first compared in terms of the relative SNR in a localized signal region, the suppression of unwanted signal external to this region, the power deposition as determined by the SAR used, the relative intensity of image artifacts, and the sensitivities of each method to overall B_1 inhomogeneity effects. For each of the methods, the phase encoding selection pulses and gradients were adjusted to achieve a 42 mm thick slab, with scan parameters for acquired spin echo images summarized in Table 1A. Noise was estimated by acquiring 10 "images" of noise only data by executing the SE scan with no active RF. The scanner calculated SAR value was recorded for each acquisition, expressed as a percentage of the 3 W/kg limit for the head.

3.3. Comparison 1 – Method Slab Excitation Analysis Metrics

The SNR was measured by dividing each slab image pixel by the standard deviation of the noise across the 10 noise acquisitions. The final SNR map was expressed as a percentage of the maximum SNR calculated for the full SE image:

$$SNR_{i,slab} = 100 \cdot \left(\frac{S_{i,slab}/\sigma_{i,noise}}{SNR_{SE,max}}\right) \quad 4.7$$

A map of the suppression achieved outside the selected slab was determined by taking the difference between the full and reduced-FOV images and converted to a percentage of the full image signal, where 100% indicates complete suppression:

$$SP = 100 \cdot \left(\frac{S_{SE}-S_{slab}}{S_{SE}}\right) \quad 4.8$$

Artifact power (AP) maps were calculated from the squared difference between the slab image for each method and the expected slab intensity, S_{base}, which is predicted to produce equal values across the slab due to the uniformity of

the FBIRN phantom. The calculation was confined to the slab region only, with mean AP values subtracted to eliminate SNR differences between the slab and uniform base signal estimate. A similar AP map was generated for the scan without preparation, with all rFOV maps expressed as a percentage of its maximum AP. The complete calculation is summarized as follows:

$$AP_{slab} = \left(\frac{100}{AP_{SE,max}}\right) \cdot \left(\left|\sqrt{\frac{(S_{slab}-S_{base})^2}{S_{base}^2}}\right| - \overline{AP}_{slab}\right) \quad 4.9$$

The mean SNR and AP values were calculated for each method confined to pixels within the slab, with mean suppression determined for object regions external to the central 42 mm width that excluded the image background. The standard deviation of the slab image signal was also calculated to provide a measure of relative image intensity uniformity as potentially impacted by B_1 inhomogeneities.

3.4. Comparison 2 – Reduced-FOV Method Analysis in Small FOV Sizes

Additional comparisons between methods were made by applying each rFOV technique to obtain a 60x60 mm image within the FBIRN phantom center. All seven methods used intrinsic anti-aliasing filters to minimize the readout dimension, with images acquired using a spin echo sequence (Table 1B). A full image SE scan was also performed with matched resolution and imaging parameters for method comparisons, as well as noise only data captured by performing 10 acquisitions with no active RF and matched dimensions to the 60x60 mm area. SNR and AP were both calculated as described previously, with the reference corresponding to a matched sized square with value of 1 at all locations, representing an ideal uniform intensity in the small region. Mean SNR, AP, and standard deviation were all determined from the derived maps.

Table 1 – Experimental Methods Scan Parameters

	Test	Scan	FOV *(mm x mm)*	TR *(ms)*	TE *(ms)*	NSA	Resolution *(mm x mm x mm)*	WFS *(pixels) / (Hz/pixel)*	Slices	R
A	Slab	SE	210 x 210	1000	40	1	1.0 x 1.0 x 3	12 / 84.5	1	1.0
B	Reduced	SE	60 x 60	1000	40	1	0.5 x 0.5 x 3	12 / 84.5	1	1.0
C	Multislice	SE	210 x 210	1700	40	1	2.2 x 2.2 x 3	6 / 169	1,3,5,7,9	1.0
D	Scaled-RF	SE	210 x 210	250	32	1	0.5 x 0.5 x 3	6 / 169	1	1.0
E	Human	SE-EPI	210 x 210	2000	76	3	0.5 x 0.5 x 3	35.2/28.8	1	2.5

Table 1 – Scan parameters for the various experimental tests of the reduced FOV techniques: A.) 42 mm slab excitation, B.) 60x60 mm FOV reduction, C.) Impact of multi-slice scans on off-slice SNR, D.) SNR impact of IVI RF scaling, and E.) human imaging reduced-FOV slab excitations (EPI factor = 9).

3.5. Comparison 3 - Simulation of Reduced-FOV Method Off-Slice Effects

To assess the multi-slice impact on out-of-slice signal using selective rFOV approaches, the longitudinal magnetization was simulated using Matlab (Mathworks, Natick, MA) for STEAM, PRESS, and IVI preparations. The simulation assumed a TR = 1700 ms, nine interleaved slices, and a T_1 value of 370 ms (as measured for the FBIRN phantom). Magnetization was predicted for only the first pass through the sequence (prior to steady state). For comparison, off-slice M_Z was simulated for each method starting with a slice selective excitation versus the described phase encoding localization. IVI was additionally simulated to predict the effect of a second 180° refocusing pulse as described by Jeong to minimize loss [14] and the double off-slice excitation proposed here in the methods. The impact of relative changes in M_Z caused by brain T_1 variation was also assessed by repeating simulations at TR values of 250, 500, 1000, 2000, 3000, and 5000 ms for gray and white matter, assuming T_1 values of 1500 and 500 ms, respectively. Contrast was then predicted by calculating their M_Z difference.

3.6. Comparison 4 - Measurement of Reduced-FOV Method Off-Slice Effects

To verify the simulated rFOV impact on multi-slice magnetization in off-slice locations, an MS-SE scan was executed with STEAM, PRESS, and IVI, that incorporated 1 to 9 interleaved slices (Table 1C). For relative SNR comparisons, a standard SE scan without preparation was also executed, with a noise matrix recorded as described previously. SNR was calculated in the central slice for each slice stack, with a mean SNR derived from the percentage SNR maps. The IVI imaging experiment was repeated at TR values of 900, 1000, 2000, and 3000 ms to verify the simulated TR effects. To demonstrate potential minimization of MS off-slice effects with the 2DRF-IVI approach, the spiral Gaussian σ_Z values were incremented and the resulting slice profile measured.

3.7. Comparison 5 –SNR Assessment of IVI Using Scaled RF Pulses

To test the feasibility of RF pulse scaling to locally correct for errors in the applied RF, three different regions were individually imaged using the standard IVI method. Each region was confined to a 40x40 mm area and targeted the phantom center, the periphery not overlapping the edge, and a transition region between the edge and center where the signal variation due to B1 inhomogeneity had a non-uniform profile. For each region, the IVI refocusing pulse was maintained at 180° and a single image acquired (Table 1D). The same sequence was then repeated with refocusing angles of 135° and 270°. For each region, the mean signal was calculated and normalized against the 180° mean for the matched location, expressed as percentage.

3.8. Comparison 6 – Reduced-FOV Method Human Imaging

As a final comparison, the seven reduced-FOV methods were applied to human brain imaging using the 7T Philips Achieva and the 32 channel parallel receive array with single volume coil transmission. A healthy human subject provided informed consent prior to scanning per an existing Institutional Review Board protocol approved by the Vanderbilt University Medical Center (Nashville, TN). Each rFOV method was individually applied to establish a 42 mm wide slab along the phase encode dimension that targeted a transverse view through the head at the level of the ventricles with a SE scan (Table 1E). An additional image was acquired with no preparation using a standard SE sequence. Comparisons between techniques were qualitative only, denoting appearance of slab boundaries, artifacts, suppression, visible noise, and relative contrast.

4. RESULTS

4.1. Comparison 1 – Method Slab Excitations

Images for each reduced-FOV method and a standard SE scan, along with calculated suppression, SNR, and AP maps are shown in Fig. 4.4, and mean statistics and measured SAR values are summarized in Table 2.1. In terms of SNR, STEAM was lowest as expected due to losses that occur with stimulated echo formation, measured below 50%. The use of three pulses for STEAM versus two for an SE scan also provides a compounding effect of B_1 errors that results in the underlying observed intensity variation. The three IVI methods had SNR values

consistent with the SE sequence as both used the same number of pulses, timings, and flip angles. The standard IVI and 2DRF produced the highest mean SNR values of all techniques, with OVS, BISTRO, and PRESS 15% to 30% lower than the standard scan. Inspection of the intensity and SNR maps reveals regions of signal dropout that exceed the other approaches. PRESS in particular, as with STEAM, is sensitive to compounding errors caused by the extra pulse applied for localization, in this case, two refocusing pulses along the phase encode and readout directions. BISTRO also appears to show an additional signal loss towards the center of the object in a region of high non-uniformity. Overall, with the exception of STEAM and BISTRO, the signal deviation was fairly consistent between approaches; lower STEAM and BISTRO variation is consistent with both techniques having lower SNR than the other approaches within the excited slab.

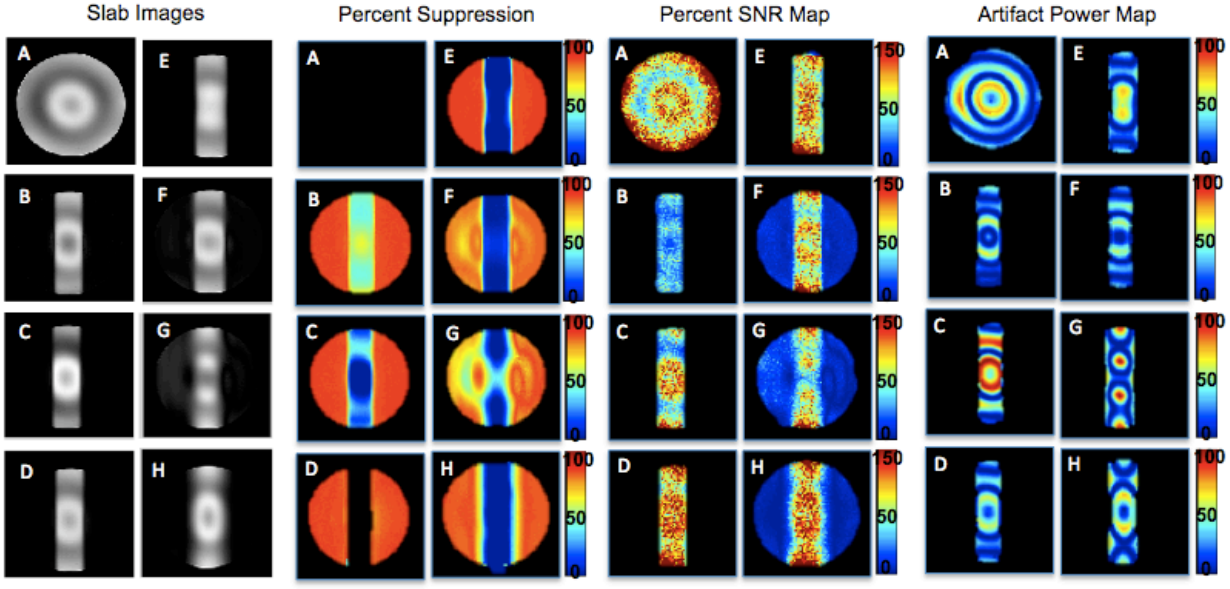

Figure 4.4 – Measured reduced-FOV image intensity in excited slab, percentage suppression of external signal, SNR in slab region, and artifact power using and FBIRN phantom and the following methods: A.) SE scan with no rFOV preparation, B.) STEAM, C.) PRESS, D.) IVI, E.) Composite RF IVI, F.) OVS, G.) BISTRO and H.) IVI with a 2D RF spiral Gaussian excitation.

Method	Table 2.1 - Slab Excitation - 210x210mm					Table 2.2 - 60x60mm		
	SNR (%)	Sup (%)	SAR (%)	AP (%)	Signal Deviation	SNR (%)	AP (%)	Signal Deviation
SE	100	0	9	100	0.207	100	100	0.190
STEAM	40	99	14	60	0.089	18	70	0.075
PRESS	75	99	19	157	0.253	47	108	0.236
IVI	107	98	12	80	0.262	56	100	0.246
Comp-IVI	95	98	32	85	0.238	76	142	0.434
2DRF-IVI	107	89	8	94	0.229	37	144	0.210
OVS	85	90	90	89	0.209	45	69	0.157
BISTRO	69	84	91	100	0.183	33	131	0.166

Table 2 – Measured SNR, percent suppression, power deposition (SAR), artifact power, and standard deviation of signal in an excited slab and 60x06mm reduced-FOV region for tested reduced-FOV imaging methods compared to the standard SE scan.

In general, the selection based methods STEAM, PRESS, and IVI have higher suppression and lower SAR values than the slab saturation methods OVS and BISTRO. With the exception of 2DRF-IVI, selective excitation methods produce near 100% suppression and SAR values approximately twice that experienced with the SE scan. Lowered 2DRF-IVI suppression was attributed to Gaussian roll-off along the phase encode direction versus the sharper transitions of the other approaches, visible in the Gaussian slice plane profile (fig. 4.5A), slab width profiles (fig. 4.5B), and suppression maps (fig. 4.4) as broad edge transitions. OVS produced a higher suppression with similar SAR to BISTRO, both with SAR values more than 10 times a SE and near system limits due to large flip angles required for saturation bands. The suppression maps were also asymmetric when comparing suppression levels on both sides of the slab, visible in slab width profiles (fig. 5B), greater for BISTRO. For both techniques, saturation bands are performed sequentially targeting first the left side then the right, repeated for OVS. The time between the final pulse application for a particular side and readout provides a delay

for T_1 recovery of the saturated signal, with OVS and BISTRO each having long preparation times relative to the other techniques at 76 ms and 103 ms, respectively. In particular, the left slab in BISTRO experiences the longest delay before acquisition and experiences greater recovery. This effect is diminished with OVS due to the relatively shorter preparation time and slab repetition.

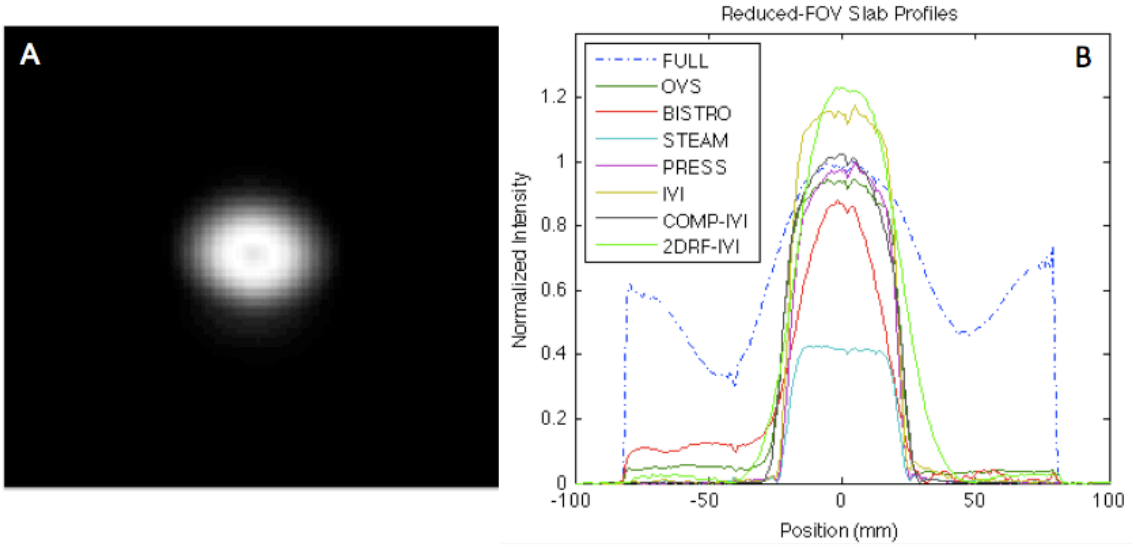

Figure 4.5 – A.) Slice plane excitation distribution for IVI using a 2D RF spiral Gaussian excitation. B.) Central profile across 42 mm excited slab for each tested reduced-FOV method and the full object with an SE scan using no preparation.

The AP maps and mean AP values largely reflected the impact of B_1 inhomogeneity on the measured signal, which was the dominant contributor to the artifacts identified. PRESS produced the highest AP values that peaked towards the center of the slab and above and below center. These correspond to increased intensity at the object center and dropout beyond, reflecting again errors introduced by using multiple refocusing pulses. STEAM had the lowest measured AP, with a similar but diminished pattern to PRESS. Among the IVI approaches, the composite seemed to have the broadest central intensity region, which reflects a

margin of intensity correction, but it did not span the entire length of the slab. The refocusing pulse in this case is not designed for diminished B_1 inhomogeneity effects and can corrupt the profile in the same manner as the other IVI techniques. In addition, the composite pulse is intended to address variation in the pulse excitation profiles only and not non-uniformity intrinsic in the coil reception profile. Lastly, BISTRO saw a higher AP than OVS that reflected a pattern of intensity peaks and dropout through the slab not observed with OVS.

4.2. Comparison 2 – Reduced-FOV Method Analysis in Small FOV Sizes

The 60x60 mm images and corresponding SNR and AP maps are presented in figure 4.6, with statistics summarized in Table 2.2. Overall, a 60 mm FOV size corresponds to a reduction of the FOV by a factor of 3.5 compared to the full 210 mm image, which alone is expected to diminish the SNR to 53%. Standard IVI produced an SNR closest to this value, with the remaining techniques generally having similar relative SNR values that were observed in the slab comparison. The exception in this case was primarily the composite IVI approach, which produced an SNR 35% higher than the standard IVI approach, 43% higher than what is expected from FOV reduction. This reflects the correction of B_1 variations that cause the central dropout visible with all other methods and the normal SE image. This central dropout was most pronounced in the images and SNR maps for BISTRO and the 2DRF pulse resulting in lowered SNR and higher AP values. However, the composite IVI approach was also determined to have the highest mean AP. Inspection of the AP map demonstrates a general roll-off from a peak center to the edge versus the dropout observed with other methods. This reflects the

performance of the phase encode refocusing five-lobe SINC pulse used for this experiment, which has a narrower effective bandwidth when used as a 180° pulse resulting in a narrowed and rounded profile. Close inspection of BISTRO and OVS reveals slight aliased edge effects throughout the images and AP effects not present with the other approaches caused by inferior suppression with these methods.

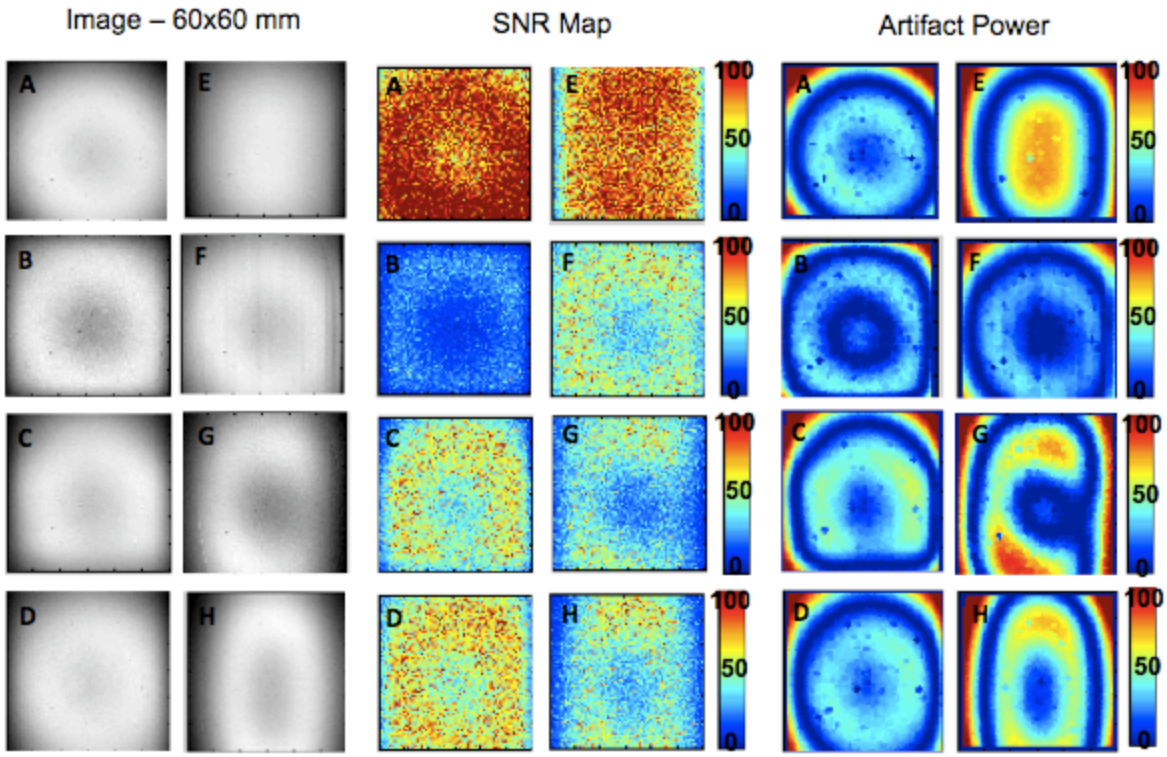

Figure 4.6 – Measured image intensity, percentage SNR, and artifact power for a 60x60 mm reduced-FOV in an FBIRN phantom using A.) SE scan (cropped) B.) STEAM, C.) PRESS, D.) IVI, E.) Composite RF IVI, F.) OVS, G.) BISTRO and H.) 2DRF-IVI.

4.3. Comparison 3 - Simulation of Reduced-FOV Method Off-Slice Effects

Matlab simulation results for off-slice longitudinal magnetization behavior in an interleaved multislice scan are summarized in fig. 4.7 for PRESS, STEAM, and IVI. In all cases, the applied pulse order is expected to produce a drop in the available M_Z for subsequent excitations performed on a slice for imaging. For PRESS (fig. 4.7A), the preparation is initiated with an x selective excitation that

results in a zeroing of the magnetization with a short T_1 recovery by the time of the subsequent y-selective refocusing pulse, which inverts recovered magnetization. M_Z undergoes additional recovery for the remainder of the 188 ms prior to the next interleave, lowered by 33% after one pass. Modifying the sequence to initiate with z-selective excitation has no effect initially on the off-slice position, but then results in

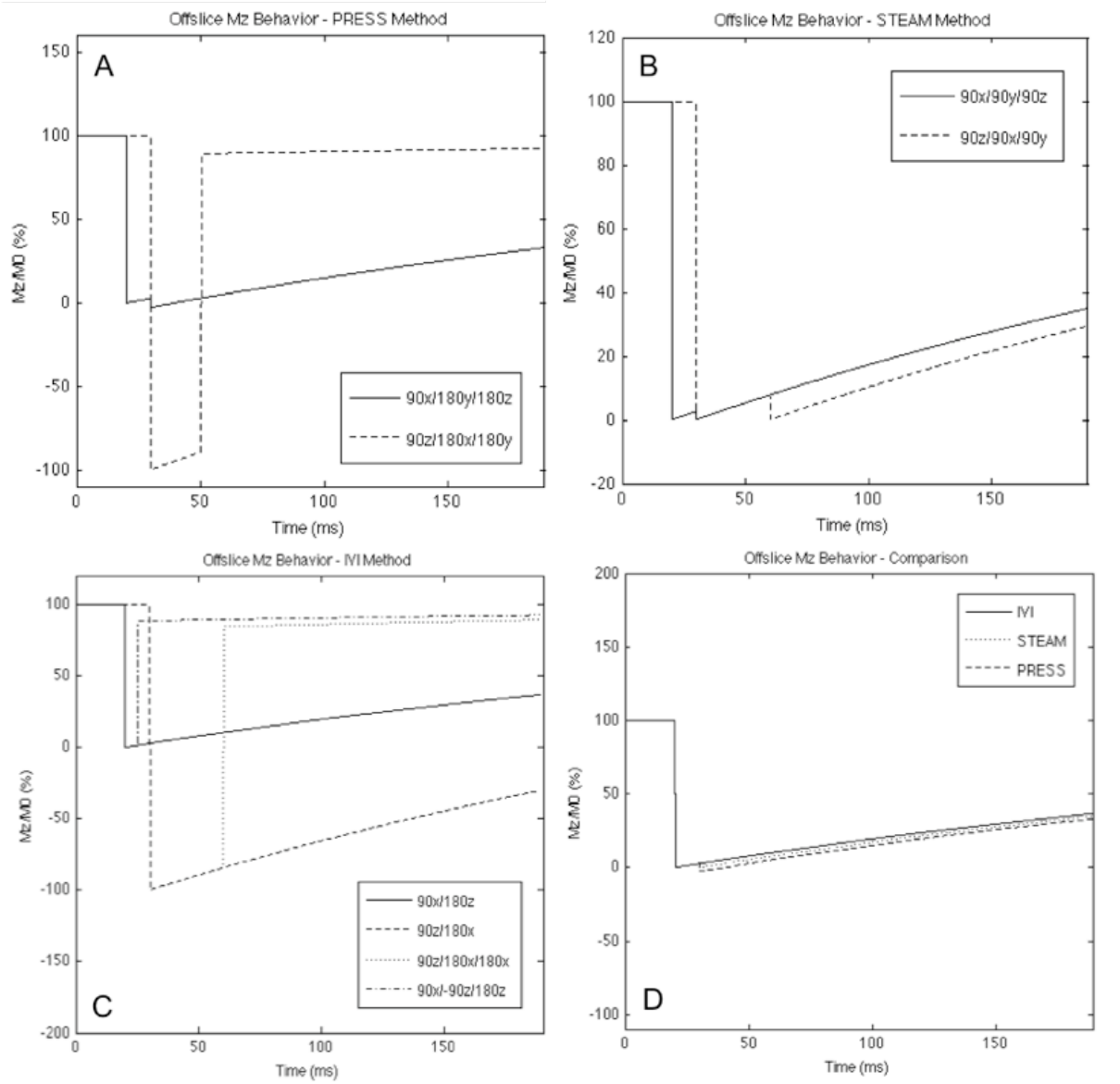

Figure 4.7 – Simulated M_Z for off-slice position during a nine slice interleaved scan, using A.) PRESS, B.) STEAM, and C.) IVI. All comparisons assume a TR of 1700 ms, TE of 60, T_1 of 370 ms, T_2* of 40 ms. Includes simulation based on initial x or z selection and introduction of double refocus and double off-slice excitation for IVI. D.) STEAM, PRESS and IVI compared for the pulse order sequence used during imaging experiments.

an inversion of the magnetization two times due to the subsequent x and y refocusing pulses, ending aligned with B_0. M_Z will undergo a margin of loss due to inversion recovery during the delay between the first and second refocusing pulse, but ends at 89% of its initial value after one interleave.

STEAM follows a similar progression to PRESS (fig 4.7B) when initiated with a 90_X, affectively zeroing M_Z followed by T_1 recovery. In this case, the second 90_Y pulse zeroes the magnetization assuming the transverse component was sufficiently dephased prior to application of the pulse. The final slice select pulse has no effect on the off-slice position, with T_1 recovery restoring the M_Z to 34% at the start of the next interleave. Reordering of the pulses to a 90_Z results in a slight decrease in the magnetization by delaying the zeroing of M_Z provided by the x and y selective pulses providing less time for it to regrow prior to the next interleave, ending 29% of start.

For IVI (fig. 4.7C), an initial 90_X results in zeroing of M_Z as with the other two methods. However, it spends the remainder of the time recovering over a longer duration than PRESS or STEAM, ending at approximately 36% of its starting value. Reordering to a 90_Z affectively inverts the longitudinal magnetization, which then undergoes an inversion recovery with M_Z decreasing to -30% over this time. Corrections in the initial z-selective configuration as demonstrated by Jeong using an additional 180_X after readout [14], restores the magnetization along the positive z direction for additional regrowth via T_1 recovery to 89%. Similarly, use of a second off-slice excitation pulse as described in the methods restores M_Z to approximately 90%, with a longer recovery duration compared to the double refocus technique.

Overall, the simulation results for PRESS, STEAM, and IVI with similar pulse orders demonstrate that M_Z in off-slice positions is less impacted by a small margin using IVI, followed by STEAM, then PRESS (fig. 4.7D). However, all three suffer approximately a 65% loss in M_Z after the first interleave. Increments in TR are simulated to diminish this loss substantially (fig. 4.8A), lowered from 70% to 20% by increasing from 1000 to 3000 ms. Tissue T_1 differences are also predicted to

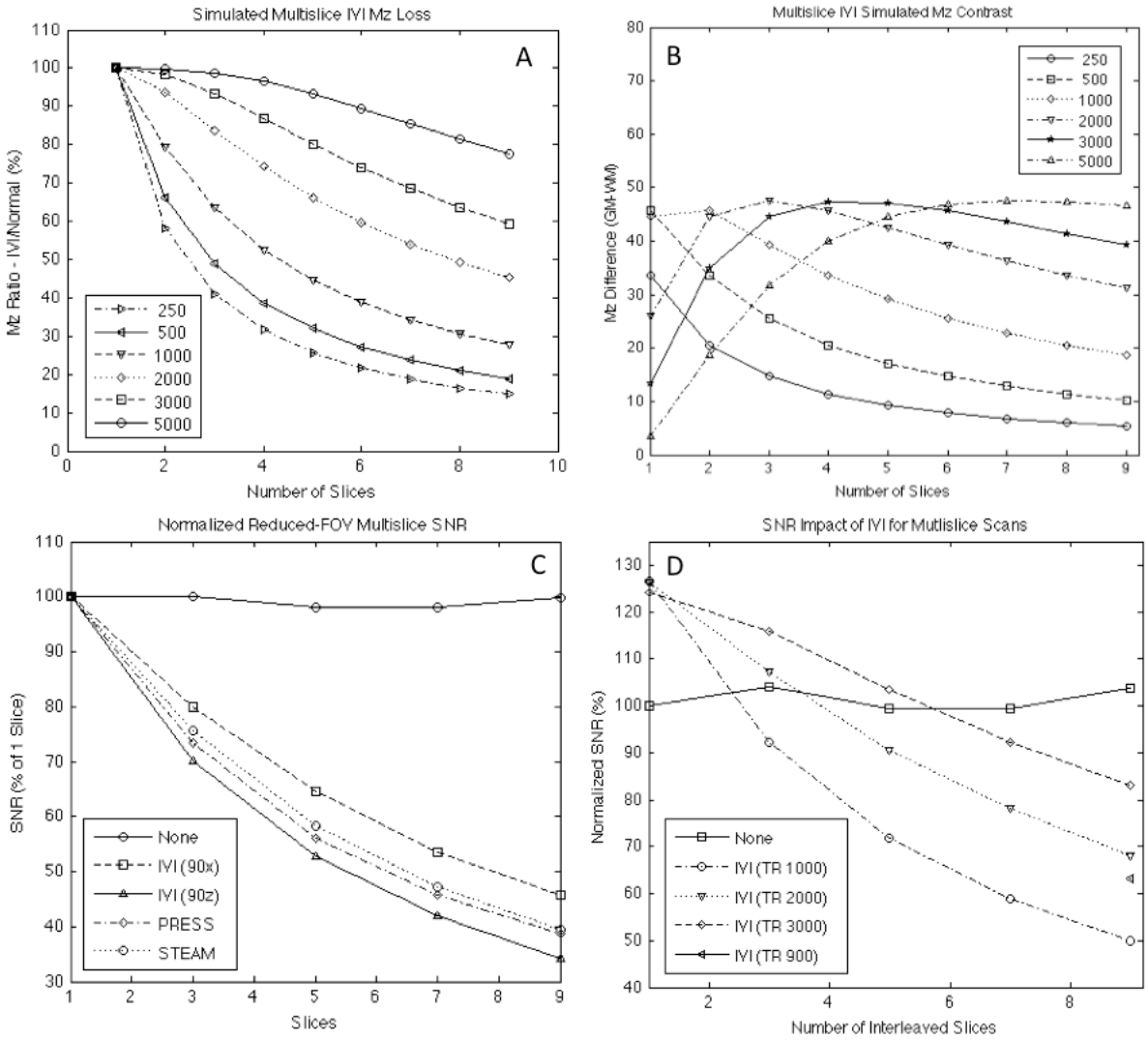

Figure 4.8 – A.) Simulated affect of TR on IVI offslice M_Z loss as the number of slices is increased. B.) Predicted M_Z difference between gray and white matter across TR for various number of slices in a multi-slice scan using IVI. C.) Comparison of measured SNR loss with incremental number of slices using STEAM, PRESS, and IVI, all SNR values normalized to the one slice SNR measurement for each method. D.) Measured IVI SNR for a multi-slice scan with incremental number of slices and a range of TR values.

encode gray and white matter contrast based on the number of slices and TR values (fig. 4.8B), with as much as a 50% difference in the expected residual M_Z using IVI.

4.4. Comparison 4 - Measurement of Reduced-FOV Method Off-Slice Effects

Multi-slice simulations were confirmed via imaging and are summarized in fig. 4.8. All methods show a decrease in the measured SNR as the number of slices in a single interleave are increased, by as much as 40% to 50% with nine slices (fig. 4.8C). The relative behavior matches well with predicted simulation results (fig. 4.7D), with IVI measured to have a higher SNR profile than STEAM and PRESS, and IVI (90_X) superior to IVI (90_Z). STEAM also showed a slightly lower SNR drop than PRESS from starting values as simulated. Improvement in the SNR profiles was demonstrated for IVI with incremental steps in TR (fig. 4.8D), increasing from 50% to 80% by using a TR of 3000 ms versus 1000 ms. Likewise, forcing an additional interleave package by dropping the TR to 900 ms resulted in a 15% increase in SNR at nine slices relative to the 1000 ms case due to the increased separation time between interleaves. Attempts to lower 2D RF slice profiles with higher σ_Z values to restrict off-slice affects produced notable profile reductions, with FWHM values of 37.2 mm, 26.3 mm, and 6.6 mm (fig. 4.9). However, side lobes and ringing effects were observed at the narrower FWHM.

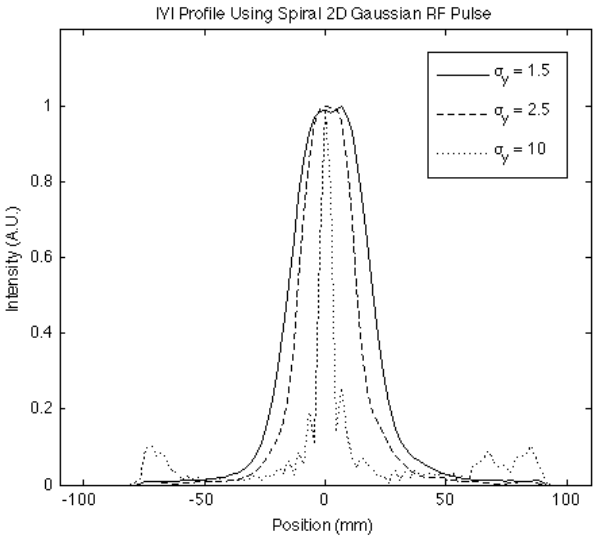

Figure 4.9 – Measured slice profile using 2D RF spiral Gaussian excitation with incremental steps in σ_Y value achieving 37.2 mm, 26.3 mm, and 6.6 mm FWHM values.

4.5. Comparison 5 –SNR Assessment of IVI Using Scaled RF Pulses

Comparisons of the mean signals between regions with the FOV reduced to 40x40 mm using standard IVI are summarized with three different angles for the slice selective refocusing pulse (fig. 4.10). For each targeted location, a distinct improvement in signal was observed at specific refocusing angles. For the center region, 135° provided a 35% improvement in mean signal versus the targeted 180° angle. For the edge, the optimal flip angle for refocusing transitioned to 270°, here, 29% better than using 180°. For the 'mix' region which contained portions of the object center and edge, 180° proved slightly better than the other two tested options, 4% better than 135°, 19% better than 270°.

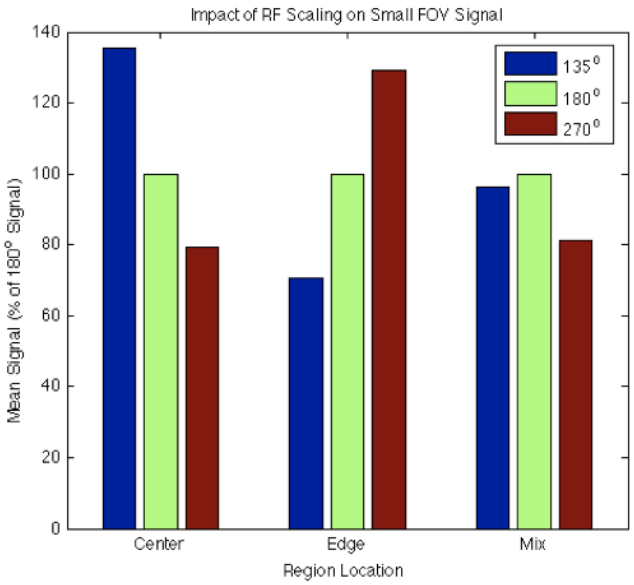

Figure 4.10 – Measured mean signal in three distinct 40x40 mm regions selected using IVI with three different refocusing angles.

4.6. Comparison 6 – Reduced-FOV Method Human Imaging

In human brain scans, the reduced-FOV methods produced distinct localization of defined slabs with no visible signal in suppression bands (fig. 4.11). Contrast was consistent between each method and the normal SE scan image with no notable signal dropout, blurring, or distortion of slab boundaries or intensities within the localized region. STEAM had a notable lower signal with visible noise throughout the slab, and BISTRO demonstrated slight residual signal along the brain

edge in the left targeted suppression area, which was observed in phantom slabs to have lower suppression. The 2DRF IVI had a slightly more diffuse boundary than the other techniques, though slab intensity was distinct from suppressed areas.

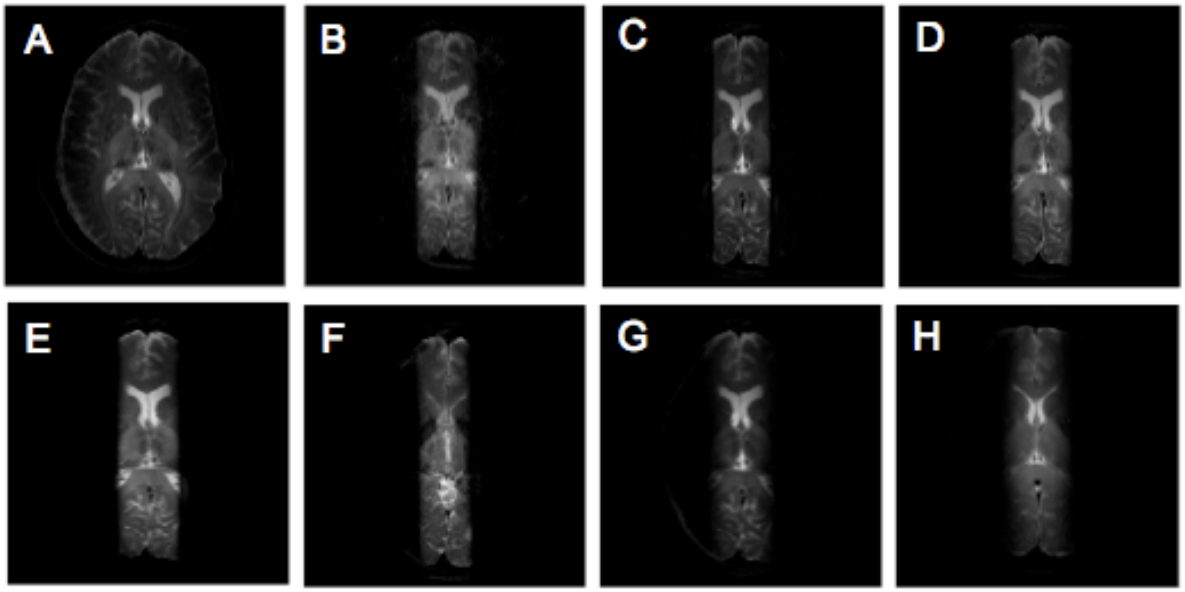

Figure 4.11 – Acquired 0.50 x 0.50 x 3 mm *in vivo* human images with TR of 3000 ms, TE of 64 ms, and 42 mm wide slabs, using: A.) SE scan, B.) STEAM, C.) PRESS, D.) IVI, E.) OVS, F.) Composite-IVI, G.) BISTRO, and H.) 2DRF-IVI.

5. DISCUSSION

Each reduced-FOV method tested demonstrated the ability to localize signal in the specified target regions, but several important differences between the techniques considered became apparent in the various metrics used for comparisons. Slab saturation based methods OVS and BISTRO both did not suppress unwanted signals as well as the other selective excitation approaches, as much as 10% to 12% lower. The high SAR of OVS and BISTRO is largely a result of an attempt to improve suppression results by using higher flip angles and

numbers of pulses in the presence of B_1 inhomogeneties. The need to keep SAR within limits translates to constraints on the minimum TR, at 950 ms for OVS, and 1200 ms for BISTRO. Additional optimization of these preparations for improved suppression did not readily produce a significant change in performance despite doubling SAR output levels beyond those recorded here. In contrast, the selective methods can use a much lower minimum TR of 150 to 250 ms at greater than 98% suppression, and still stay within SAR limits, with higher SAR for PRESS and STEAM compared to the IVI methods due to requiring an additional pulse for selectivity along a third dimension. The 2DRF-IVI approach produced a lower SAR than the standard SE scan due to the overall low amplitude and duration of the 2D pulse. Overall, unwanted signal must be suppressed enough to prevent aliasing artifacts in the reduced image. These artifacts were not visible in images or AP maps with the selective methods, and were marginally observed with OVS and BISTRO at 90% suppression.

From an SNR standpoint, it is expected that STEAM will lose half of its SNR because it refocuses only half of the magnetization. All other methods, however, are expected to produce comparable SNR measurements. However, the SNR values achieved in practice are in part, complicated by B_1 errors that affect the accuracy of both the excitation 90° and refocusing 180° pulses. The particular phantom tested demonstrated high variations in B_1 with a central dip caused by refocusing errors. These corresponded to high variations in the AP maps. Methods such as PRESS that use multiple refocusing pulses see a compounding effect of both pulses having erroneous angles with additional peripheral loss and complex AP patterns. The

SNR in the Composite-IVI case improved notably beyond the remaining methods, but would benefit from extension to both the excitation and refocusing pulse to achieve better uniformity for larger FOV sizes or regions of high variation. In this context, scaling of RF provided a way to improve SNR in small regions without using such pulses, by as much as 35%. This improvement correlated well with the measured SNR increase achieved with the composite pulse in the 60x60 mm region, suggesting the composite similarly improved signal performance. Overall, scaling of the RF combined with use of fewer pulses to achieve localization, such as with the IVI approach, produces superior SNR and diminished AP performance due to fewer compounding errors.

Despite generally superior SAR, suppression, and AP measurements, the STEAM, PRESS, and IVI based methods constrain the contrast to a spin echo weighting, with T_2 decay initiated at the beginning of all of these preparations. OVS and BISTRO, on the other hand, do not affect the contrast weighting of the sequence they precede, except to the extent to which the TR is appropriate based on staying within SAR limits. Additionally, the suppression-based approaches enable other target flip angles for selection within the primary sequence to be optimized to the desired Ernst angle or specific contrast desired. Methods such as STEAM and PRESS also induce additional constraints on the minimum TE possible due to the additional pulses required to prevent overlap between neighboring pulse pairs and gradients. With the SINC pulses applied for excitation and refocusing in these cases, this minimum TE value was 24 ms, which constrains scans optimized

for shorter values. In general, OVS and BISTRO synergize well with a variety of scan types since the preparation is separated from the imaging scan.

The multi-slice performance establishes a significant distinction between the various methods and potential uses at 7T. As implemented, the STEAM, PRESS, and IVI based approaches produce up to a 65% loss in available longitudinal magnetization for a nine slice interleaved acquisition. However, as demonstrated, the extent of the loss is largely dependent on the TR value, number of slices, and T_1 of the tissue being imaged. Longer TR settings and shorter T_1 or fewer interleaves can substantially reduce the off-slice impact of the selective excitation approaches. This property also has an impact on the contrast within a slice that has experienced these preparations because of T_1 differences between tissues in a target region, which could be exploited to achieve specific contrast, but primarily demonstrates the impact of rFOV for MS imaging.

The simulated results demonstrate the potential improvement provided by methods that correct for this effect, including the addition of a second refocusing pulse for IVI techniques initiated with a slice selective excitation to reduce off-slice losses [14], and the use of a second excitation to restore magnetization in impacted slices. The combination of two refocusing pulses in this case closely resembles the PRESS approach, which also predicts improved MS performance when initiated with a slice select 90°, reducing loss to only 10% for the configuration simulated. The benefit of the PRESS versus the double refocus IVI sequence is that the final inversion occurs earlier in the interleave time frame, prior to readout, allowing for greater signal recovery before the next interleave occurs. 2DRF pulses offer an

ideal approach to improve MS performance by preventing saturation of the interleaved slices with narrow profiles in the slice direction. The method implemented here requires additional optimization to achieve this, either through further adjustment to the Gaussian scaling or use of rectangular functions.

In sum, the reduced-FOV method selected for any application is based first on the desired contrast and imaging parameter constraints. When spin echo weighting is acceptable, for single slice or 3D scans, an IVI based approach puts the fewest limits on TE and TR, has the lowest SAR, and introduces no negative SNR impact such as STEAM. Though it is designed only to constrain the FOV in the PE dimension, readout reduction is readily accomplished using anti-aliasing filters. Combining the IVI approach with composite RF pulses and scaling of the RF amplitudes provides a means to further improve selectivity while simultaneously correcting for B_1 inhomogeneity in the target area. However, if gradient echo based sequences are required to produce T_2*contrast, suppression methods are the primary option using OVS. Compared to BISTRO, the implementation here produced better suppression, lower SAR, and fewer artifacts. OVS is also preferential for MS scans because other approaches suffer from off-slice affects as long as SAR constraints produce acceptable TR values and interleave slice numbers. Otherwise, PRESS or IVI compensated with additional pulses or 2D RF with narrow slice profiles offer preferable alternatives.

6. CONCLUSIONS

The analysis described here provides the first comprehensive assessment of a variety of reduced-FOV techniques for imaging localization at 7T. Specific optimizations are uniquely defined for techniques such as OVS and IVI. A number of potential improvements for reduced-FOV multi-slice performance are also identified. The SNR, suppression, SAR, AP, signal distribution, and MS behavior combined provide a foundation for improved reduced-FOV development and application for 7T high- resolution studies that would benefit from its use.

7. ACKNOWLEDGEMENTS

This work is supported by NIH grant number R01EB000461. The authors acknowledge Marcin Jankiewicz of the Vanderbilt University Institute of Imaging Science (VUIIS) for his assistance with implementation of 2D spiral excitation.

8. REFERENCES

[1] M.A. Griswold, P.M. Jakob, R.M. Heidemann, M. Nittka, V. Jellus, J. Wang, B. Kiefer, A. Haase, Generalized autocalibrating partially parallel acquisitions (GRAPPA), Magn Reson Med, 47 (2002) 1202-1210.

[2] K.P. Pruessmann, M. Weiger, M.B. Scheidegger, P. Boesiger, SENSE: sensitivity encoding for fast MRI, Magn Reson Med, 42 (1999) 952-962.

[3] P.B. Roemer, W.A. Edelstein, C.E. Hayes, S.P. Souza, O.M. Mueller, The NMR phased array, Magn Reson Med, 16 (1990) 192-225.

[4] J. Finsterbusch, J. Frahm, Half-Fourier single-shot STEAM MRI, Magnetic resonance in medicine : official journal of the Society of Magnetic Resonance in Medicine / Society of Magnetic Resonance in Medicine, 47 (2002) 611-615.

[5] Y. Xu, E.M. Haacke, Partial Fourier imaging in multi-dimensions: a means to save a full factor of two in time, Journal of magnetic resonance imaging : JMRI, 14 (2001) 628-635.

[6] M. Lustig, D. Donoho, J.M. Pauly, Sparse MRI: The application of compressed sensing for rapid MR imaging, Magn Reson Med, 58 (2007) 1182-1195.

[7] P.A. Bottomley, Selective Volume Method for Performing Localized NMR Spectroscopy, in, General Electric Company, United States, 1984.

[8] N.G. Dowell, T.M. Jenkins, O. Ciccarelli, D.H. Miller, C.A. Wheeler-Kingshott, Contiguous-slice zonally oblique multislice (CO-ZOOM) diffusion tensor imaging: examples of in vivo spinal cord and optic nerve applications, J Magn Reson Imaging, 29 (2009) 454-460.

[9] D.A. Feinberg, J.C. Hoenninger, L.E. Crooks, L. Kaufman, J.C. Watts, M. Arakawa, Inner volume MR imaging: technical concepts and their application, Radiology, 156 (1985) 743-747.

[10] J. Finsterbusch, Fast-spin-echo imaging of inner fields-of-view with 2D-selective RF excitations, J Magn Reson Imaging, 31 1530-1537.

[11] J. Finsterbusch, High-resolution diffusion tensor imaging with inner field-of-view EPI, J Magn Reson Imaging, 29 (2009) 987-993.

[12] J. Frahm, H. Bruhn, M.L. Gyngell, K.D. Merboldt, W. Hanicke, R. Sauter, Localized high-resolution proton NMR spectroscopy using stimulated echoes: initial applications to human brain in vivo, Magn Reson Med, 9 (1989) 79-93.

[13] C.J. Hardy, et al, Spatial Localization in Two Dimensions Using NMR Designer Pulses, Journal of Magnetic Resonance, 82 (1989) 647-654.

[14] E.K. Jeong, S.E. Kim, J. Guo, E.G. Kholmovski, D.L. Parker, High-resolution DTI with 2D interleaved multislice reduced FOV single-shot diffusion-weighted EPI (2D ss-rFOV-DWEPI), Magn Reson Med, 54 (2005) 1575-1579.

[15] P. Le Roux, R.J. Gilles, G.C. McKinnon, P.G. Carlier, Optimized outer volume suppression for single-shot fast spin-echo cardiac imaging, J Magn Reson Imaging, 8 (1998) 1022-1032.

[16] Y. Luo, R.A. de Graaf, L. DelaBarre, A. Tannus, M. Garwood, BISTRO: an outer-volume suppression method that tolerates RF field inhomogeneity, Magn Reson Med, 45 (2001) 1095-1102.

[17] D. Mitsouras, R.V. Mulkern, F.J. Rybicki, Strategies for inner volume 3D fast spin echo magnetic resonance imaging using nonselective refocusing radio frequency pulses, Med Phys, 33 (2006) 173-186.

[18] J. Pfeuffer, P.F. van de Moortele, E. Yacoub, A. Shmuel, G. Adriany, P. Andersen, H. Merkle, M. Garwood, K. Ugurbil, X. Hu, Zoomed functional imaging in the human brain at 7 Tesla with simultaneous high spatial and high temporal resolution, Neuroimage, 17 (2002) 272-286.

[19] L. Pisani, R. Bammer, G. Glover, Restricted field of view magnetic resonance imaging of a dynamic time series, Magn Reson Med, 57 (2007) 297-307.

[20] E.U. Saritas, C.H. Cunningham, J.H. Lee, E.T. Han, D.G. Nishimura, DWI of the spinal cord with reduced FOV single-shot EPI, Magn Reson Med, 60 (2008) 468-473.

[21] B.J. Wilm, J. Svensson, A. Henning, K.P. Pruessmann, P. Boesiger, S.S. Kollias, Reduced field-of-view MRI using outer volume suppression for spinal cord diffusion imaging, Magn Reson Med, 57 (2007) 625-630.

[22] A. Haase, J. Frahm, D. Matthaei, W. Hanicke, H. Bomsdorf, D. Kunz, R. Tischler, MR imaging using stimulated echoes (STEAM), Radiology, 160 (1986) 787-790.

[23] R. Turner, M. von Kienlin, C.T. Moonen, P.C. van Zijl, Single-shot localized echo-planar imaging (STEAM-EPI) at 4.7 tesla, Magnetic resonance in medicine : official journal of the Society of Magnetic Resonance in Medicine / Society of Magnetic Resonance in Medicine, 14 (1990) 401-408.

[24] J. Frahm, W. Hanicke, H. Bruhn, M.L. Gyngell, K.D. Merboldt, High-speed STEAM MRI of the human heart, Magnetic resonance in medicine : official journal of the Society of Magnetic Resonance in Medicine / Society of Magnetic Resonance in Medicine, 22 (1991) 133-142.

[25] J. Pauly, et al, A k-space Analysis of Small-Tip-Angle Excitation, Journal of Magnetic Resonance, 81 (1989) 43-56.

[26] J. Moore, M. Jankiewicz, H. Zeng, A.W. Anderson, J.C. Gore, Composite RF pulses for B1+-insensitive volume excitation at 7 Tesla, J Magn Reson, 205 50-62.

[27] J. Moore, M. Jankiewicz, A.W. Anderson, J.C. Gore, B1+-insensitive slice-selective pulses constructed from optimized non-selective composite waveforms, Proc. Int. Soc. Magn. Reson. Med., 19 (2011) 2912.

[28] L. Friedman, G.H. Glover, Report on a multicenter fMRI quality assurance protocol, Journal of magnetic resonance imaging : JMRI, 23 (2006) 827-839.

CHAPTER V

HIGH RESOLUTION BRAIN IMAGING WITH REDUCED SCAN TIMES COMBINING REDUCED-FOV, PARALLEL IMAGING, AND EPI AT 7T

ABSTRACT

In this study, we describe the combination of SENSE parallel imaging and reduced-FOV techniques with echo planar imaging (EPI) to rapidly obtain high-resolution images of the human brain at 7T. EPI is attractive because of the significant reduction in scan durations possible versus standard readouts. However, achievable resolution is limited due to geometric distortion, signal blurring, and dropout artifacts that compound as resolution increases because of sensitivity to susceptibility variations and T_2* losses. By combining SENSE and reduced-FOV, the number of phase-encoding lines can be restricted to shorten echo train lengths and minimize these effects, while also reducing patient motion or physiological noise artifacts. Use of a 7T field strength provides additional signal to counter losses due to the resolution increase and use of the SENSE and reduced-FOV methods. Reduced-FOV provides the added benefit of performing higher accelerations not possible with SENSE alone, which is constrained in practice by g-factor noise amplification. Here, IVI and OVS methods are specifically developed and tested with SENSE for imaging in a variety of human brain regions at 160 to 500 μm resolutions using single and multi-shot EPI, and combined to provide rapid 3D EPI

images. Compared to full scan approaches, SENSE-IVI demonstrates a lowering of motion, susceptibility, and distortion artifacts. The contrast allows high-resolution visualization of a variety of features in small regions, including localized imaging of the hippocampus. Scans are performed in 2 to 15 minutes with acceleration factors of 122 to 1,400 in acquisition times compared to full-FOV protocols. The results support wide application of the combined approach for human brain imaging.

1. INTRODUCTION

Echo planar imaging (EPI) techniques enable rapid acquisition of a significant portion of k-space within a single readout time. In a single-shot configuration, full k-space is covered potentially in small fractions of a second; in a multi-shot approach, a fraction of the total image is acquired each shot as determined by the specified EPI factor, and the time between shots may dominate the total scan time. The achievable reductions in imaging duration obtained using an EPI readout with an entire image acquired in a very short time has resulted in the widespread adoption of this method for diffusion imaging and for functional MRI studies that attempt to temporally resolve the BOLD activation in the brain resulting from external stimulus. However, applications to high resolution anatomical imaging face challenges that constrain its use. This is primarily due to the nature of the acquisition, which can often result in degraded image quality due to geometric distortions, blurring, and signal dropout induced in regions of high susceptibility variation. These effects are compounded as the resolution is increased due to the resulting increment in the

echo train length relative to tissue T2* values. As such, the resolution achieved with this technique is often limited to greater than a millimeter scale where contrast and feature definition may be diminished.

Simultaneous application of parallel imaging based methods such as SENSE with EPI can result in a reduction in the observable artifacts [1, 2]. Parallel methods use the extra encoding provided by the additional coil elements in parallel receive arrays to reduce the number of lines of k-space that are required to generate an image. Typically, this would result in an aliasing or fold-over artifact, because the FOV is lowered to within the object dimensions. This effect is removed by proper reconstruction of the undersampled data using knowledge of coil sensitivities and the aliasing pattern. Acquisition of fewer lines of k-space results in shorter echo train lengths for EPI relative to T2* values, enabling higher resolutions before susceptibility based artifacts are similarly apparent. The parallel approach, however, comes at the cost of diminished SNR by the square root of the reduction factor. Additional loss is also caused by amplification of noise attributed to the reconstruction method quantified by the “geometry factor”, so-called because of its dependence on coil and object geometries, which increases the higher the reduction value. For this reason, SENSE based accelerations are typically constrained to two to four fold reductions to minimize g-values.

Similar reductions in image acquisition have also been obtained by constraining signal to localized regions using reduced-FOV (rFOV) imaging techniques. These methods apply a combination of RF pulses that each select along different dimensions to spatially localize excitation to restricted areas.

Specifically, Inner Volume Imaging (IVI) techniques apply phase encoding excitation and slice selective refocusing to achieve two dimensional signal restrictions [3, 4]. Likewise, with Outer Volume Suppression (OVS), multiple pulses are applied external to the region of interest with the excited signal then dephased while preserving signal intensity located in the target area for subsequent imaging [5]. The end result of both methods enables the FOV to be reduced to the new signal dimensions without inducing aliasing effects. Though it also results in a loss in SNR, the benefit over SENSE based acceleration is the absence of a g-factor loss at higher reduction values, constrained by dimensions of regions targeted.

The combination of parallel and reduced-FOV imaging together may potentially be used synergistically with rapid EPI scans [6-8], enabling it to used in a number of high resolution studies that target either specific anatomical or functional applications. The use of ultra-high field 7T is motivated in part to improve resolution by providing the additional signal strength required when voxels are small. Increasing the number of parallel array elements also serves as a source of additional signal, and provides improved SENSE performance due to lowered g-factor values. Ultra high fields, however, face a number of challenges such as increased B1 inhomogeneity and shorter T_2* values. In addition, high-resolution acquisitions necessitate acquisition of large array sizes that create efficiency constraints and introduce greater sensitivity to physiological and motion artifacts that corrupt image quality. These are mitigated by the combination of parallel and reduced-FOV to diminish data sizes and lower imaging times.

Despite these challenges, a number of investigators have demonstrated the benefits of 7T to achieve improvements in resolution approaching 200 to 400 μm in the brain, with specific application in hippocampus and multiple sclerosis lesion imaging [9-12]. In this study, we aim to demonstrate the benefits of synergistically combining SENSE and reduced-FOV imaging with multi-shot and single-shot EPI to achieve 160 to 500 μm resolutions in localized brain regions using a 7 Tesla system with reduced imaging times. The method will be compared with standard scans specifically applying IVI and OVS reduced-FOV methods to demonstrate image quality improvement at high resolution and scan time reductions for spin echo and gradient echo scans. Specific applications of small FOV hippocampal imaging will also be demonstrated where resolution improvements enable identification of hippocampal sub-regions. Lastly, IVI and OVS will be combined with EPI and SENSE to perform efficient high-resolution 3D imaging in localized brain volumes.

2. METHODS

2.1 SNR Analysis of Reduced-FOV Methods for High Resolution Imaging at 7T

The combination of methods applied in this study incorporate a number of potential sources of signal improvement compared to traditional scans at 3T to support resolution enhancement. B_0 Field strength increases to 7T in particular, theoretically provide an increase in achieved SNR versus, for example, 3T imaging:

$$f_{field} = \frac{B_{0,new}}{B_{0,old}} = \frac{7T}{3T} = 2.33 \qquad 5.1$$

7T imaging in the human brain, however, is challenged by an increase in B1 inhomogeneity due to so-called “dielectric resonance” or interference effects that result in spatial variation of the achieved flip angle, θ, causing a reduction in the achieved SNR when comparing the actual versus target angle. At 7T, this error has been determined to produce as much as a 31% loss in achieved SNR [13]:

$$f_{B1} = \frac{\sin(\theta_{actual})}{\sin(\theta_{target})} = 0.69 \qquad 5.2$$

SNR performance of parallel arrays used for imaging experiments has been demonstrated to improve as the number of receiver elements increases [14]. The SNR adjustment corresponds to the relative SNR for each individual array size. From simulations provided by de Zwart, the mean SNR of 15.32 and 3.64 were calculated for a 32 channel and 8 channel parallel array, respectively, for a ratio of:

$$f_{coil} = \frac{SNR_{32}}{SNR_{8}} = \frac{15.32}{3.64} = 4.21 \qquad 5.3$$

Parallel receive arrays enable SENSE based imaging acceleration, with SNR lowered due to established undersampling of k-space and g-factor based noise amplification [1]. The magnitude of this factor has both receiver array size and field strength dependence, diminishing as both increase enabling potential SNR improvements over 3T use [15-17]. Simulation results from these studies predict mean g-values of 1.13 and 1.86 at an R-value of 4, for an increase in SNR:

$$f_{SENSE} = \left(\frac{SNR_{7T,32}}{\sqrt{R}g_{7T,32}}\right)\Big/\left(\frac{SNR_{3T,8}}{\sqrt{R}g_{3T,8}}\right) = \frac{g_{3T,8}}{g_{7T,32}} = \frac{1.86}{1.13} = 1.65 \qquad 5.4$$

Image accelerations can also be accomplished using the described reduced-FOV signal localization technique that does not have a g-factor component to the resulting SNR loss. In this case, SNR is diminished by the factor reduction of the

phase encoding FOV, which can be countered by increasing the number of acquisitions. Relative to a SENSE only acceleration, rFOV combined with SENSE to lower g-values improves SNR as defined by the relative g-factors, SENSE acceleration R, Z-factor FOV reduction, and reduced and full acquisition numbers, NA_{RFOV} and N_{FULL}. Assuming equal R and Z values to achieve a total reduction of four and equal acquisition numbers, the electrodynamic simulations predict [15, 16]:

$$f_{RFOV} = \frac{g_{SENSE}}{g_{RFOV}} \sqrt{\frac{NA_{RFOV} \cdot R}{NA_{SENSE} \cdot Z}} = \frac{1.20}{1.00}\sqrt{1} = 1.20 \qquad 5.5$$

Applying SENSE or reduced FOV imaging with an EPI readout results in a reduction in the applied echo train length, enabling the center of k-space to occur at a shorter echo time shifted by ΔTE, establishing lowered T2* blurring effects and reduced distortion. The readout lengths are also shortened translating to a broader sampling bandwidth, BW_{RFOV}, compared to the full acquisition, BW_{FULL} [18-20]. For a diffusion weighted single shot EPI protocol using SENSE, Jaermann demonstrated up to a 1.7 factor increase in achievable SNR due to reduction of the loss effects:

$$f_{EPI} = e^{-\Delta TE/T2*} \sqrt{\frac{BW_{FULL}}{BW_{RFOV}}} = 1.70 \qquad 5.6$$

Lastly, applying reduced-FOV with EPI can potentially diminish motion or physiological effects due to shorter acquisition times [21]. Prior studies demonstrated as much as an 8.8% SNR improvement using partial fourier methods to diminish data sizes [22], dependent on the relative extent of physiological noise, σ_{RFOV} and σ_{FULL}, and the relative number of points obtained for each acquisition:

$$f_{motion} = \frac{SNR_{RFOV}}{SNR_{FULL}} = \frac{\sigma_{FULL}\sqrt{N_{FULL}}}{\sigma_{RFOV}\sqrt{N_{RFOV}}} = 1.088 \qquad 5.7$$

In sum, the combination of these described factors translate to a total potential impact on the established image SNR that is based on their product:

$$f_{total} = f_{field} \cdot f_{B1} \cdot f_{SENSE} \cdot f_{EPI} \cdot f_{RFOV} \cdot f_{motion} \quad 5.8$$

This factor describes the SNR improvement for a 7T system using a 32 channel array when combined with SENSE, reduced-FOV techniques, and EPI, relative to that obtained with a 3T system using an 8 channel coil, SENSE, and EPI, assuming comparable resolutions. The factor improvement in SNR can be translated into: 1.) a higher in-plane resolution by taking the square root of this value, 2.) a direct improvement in the slice thickness or achieved SNR for a fixed resolution, or 3.) a reduction in the scan duration by using higher SENSE or rFOV factors or lowering the number of acquisitions. Table 1 predicts potential values for f_{total} assuming comparable signal contribution from relaxation effects and applying described theoretical values, predicting as high as a four-fold resolution improvement. The scan duration depends upon the TR, SENSE and reduced FOV factors that lower the number of phase encoding lines, and number of acquisitions:

$$T_{scan} = TR \cdot NA \cdot N_{PE}/(R \cdot Z) \quad 5.9$$

Table 1 –SNR Factors for 7T Parallel Reduced-FOV Imaging

	f_{field}	f_{coil}	f_{B1}	f_{sense}	f_{rfov}	f_{epi}	f_{motion}	f_{total}
A	2.33	1.00	0.69	1.00	1.00	1.00	1.00	1.61
B	2.33	1.10	0.69	1.65	1.20	1.00	1.00	3.50
C	2.33	1.10	1.00	1.10	1.10	1.10	1.10	3.75
D	2.33	4.21	1.00	1.65	1.20	1.70	1.09	15.45

Table 1 – Factors adjustment in SNR for 7T with 32 channel coil, SENSE-IVI-EPI versus 3T with an 8 channel coil, using SENSE-EPI. Factors assume A.) field strength dependent improvement only with B1 inhomogeneity loss, B.) Moderate improvement due to lowered g-factor values, C.) 10% improvement for all factors with B1 correction, D.) maximum anticipated values based on published theoretical results.

2.2 SNR Efficiency of Reduced-FOV Approach for High Resolution Imaging

The SNR efficiency of rapid imaging methods such as SENSE are known to be less than standard imaging approaches due to compounding g-factor values that increase the higher the SENSE acceleration [23]. However, efficiency has been demonstrated to be greater for similar rapid imaging methods that rely on half scan or partial k-space sampling when it results in diminished physiological and motion based effects [22]. Similar noise reduction is predicted for use of the described SENSE-IVI approach by potentially lowering distortions that occur with high-resolution rapid EPI scans. Assuming SENSE-IVI combined with EPI for multi-slice imaging, the SNR efficiency for this combination and for a SENSE only protocol are:

$$SNR_{RFOV} = (\Delta x \Delta y \Delta z / g_{RFOV})\sqrt{TR/BW} \quad 5.10$$

$$SNR_{SENSE} = (\Delta x \Delta y \Delta z / g_{SENSE})\sqrt{TR/BW} \quad 5.11$$

The relative efficiency of these approaches then translates to:

$$\frac{SNR_{RFOV}}{SNR_{SENSE}} = \frac{g_{SENSE}}{g_{RFOV}} \quad 5.12$$

This comparison indicates that using SENSE-IVI or IVI only versus SENSE predicts superior SNR efficiency as long as the established g-factor value for SENSE-IVI is lower for similar accelerations that use only SENSE. For high reduction factors, the difference could be significant, with g-factor values potentially inflating two to four-fold for SENSE when accelerations increase [15, 16]. In either case, compared to a standard scan, incorporating potential reduction of physiological and patient motion effects, as well as distortion and signal dropout, SNR efficiency is potentially enhanced for SENSE-IVI, based on the extent of established g-factor values:

$$\frac{SNR_{RFOV}}{SNR_{MS}} = \frac{f_{motion} \cdot f_{EPI} \cdot f_{B1}}{g_{RFOV}} \qquad E5.13$$

This equation also incorporates a factor improvement resulting from reduced B1 variations across a smaller FOV. In small regions, the B1 variation is potentially less than that experienced across the entire object, and correctable using localized power calibration or RF scaling techniques [24]. In sum, the value of the combined three factors can vary based on the location within the brain, subject compliance with the scan, and physical dimensions of the region. However, these improvements need only exceed the established g-value for SENSE-IVI, which can be minimized by using a lower contribution to the acceleration by SENSE. Figure 5.1 plots the potential improvement in SNR efficiency based on the magnitude of the combined factors, assuming 0% to 30% potential improvement for each to cover the theoretical range predicted previously for each, over a range of g-values spanning from 1.0 to 1.6. Here, significant improvement in efficiency is realistically achievable if the g-factor is well managed, with relative efficiencies greater than one indicating superior performance for implementation of reduced-FOV techniques. A 10% improvement in SNR at a g-value of 1.1 is sufficient to demonstrate greater SNR efficiency.

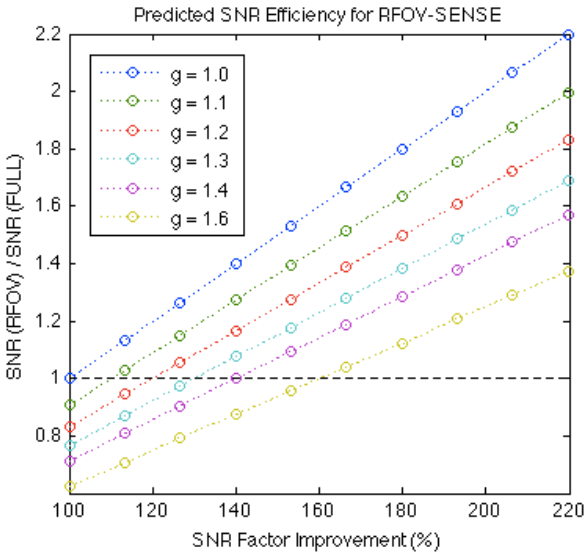

Figure 5.1 – Simulated SNR efficiency using a combination of reduced-FOV and SENSE across g-factor values ranging from 1.0 to 1.6 and combined improvements of B1 inhomogeneity, reduction in geometric distortion and physiological noise. A combined SNR factor of 220% corresponds to a 30% improvement in each. A ratio of one indicates superior SNR efficiency using rFOV imaging versus a full acquisition.

2.3 IVI Reduced-FOV Method for 7T Human Imaging

The Inner-Volume Imaging (IVI) reduced-FOV technique was implemented as described by Feinberg (Fig. 5.2) using a combination of a 90° selective and 180° refocusing pulse applied along orthogonal directions to achieve signal localization in a restricted region [3]. Spins in a volume that have experienced both pulses as dictated by their corresponding bandwidths and simultaneously applied gradients will be appropriately excited and refocused. The region is defined by the intersection of two planes; for this implementation, the excitation pulse is restricted to selectivity in the phase encode dimension, and refocusing is confined to the slice profile.

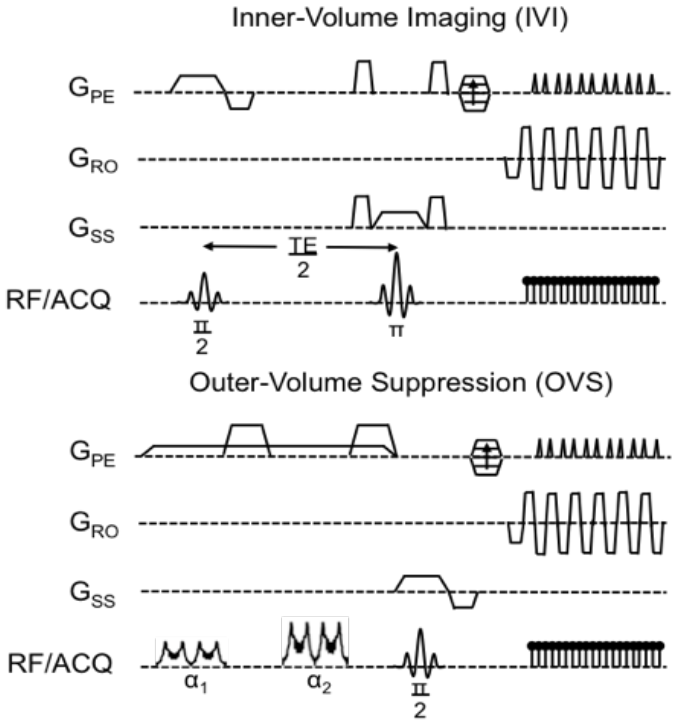

Figure 5.2 – Pulse sequence diagrams for IVI and OVS methods. IVI incorporates intersection of phase encode selective 90 and slice selective refocusing. OVS applies saturation pulses external to target FOV to localize signal.

To optimize IVI for reduced-FOV imaging at 7T, a variety of pulse types were empirically explored for excitation and refocusing for a range of localization dimensions spanning 1 to 200 mm. Specific emphasis was placed on minimizing ripple effects in the pulse passband and sideband regions and obtaining sharp profile roll-off. This corresponded to a five-lobe SINC pulse for x-dimension

selectivity with a 15 μT amplitude and 3.92 ms duration, and a 5.40 ms duration pulse for refocusing with the same amplitude. The refocus pulse was performed between two balanced crusher gradients maximized to the 40 mT/m system strength limit and 4 ms durations to ensure all unwanted signal was sufficiently spoiled. As described, IVI was executed prior to imaging phase encoding and readout gradients.

2.4 OVS Reduced-FOV Method for 7T Human Imaging

Outer-Volume Suppression (OVS) was implemented as diagrammed in fig. 5.2 to achieve a suppression based reduced-FOV technique to enable T_2* weighted imaging. Here, two saturation bands were sequentially applied on both sides of the target region where localization is achieved by selectively exciting spins confined along the phase encoding dimension followed by large spoiling gradients to dephase the excited signal. To improve saturation performance, the pulse pairs were repeated twice with different flip angles. The OVS preparation was optimized using three different pulse types to explore relative suppression ability and achieved power deposition (specific absorption rate, SAR), including a frequency modulated (FM) pulse with a linear phase distribution, a SINC pulse optimized for 90° flip angles, and a REST slab developed for saturation techniques. These pulses were empirically optimized to reduce SAR, minimize sideband ripple that would affect localized region signal quality, achieve sharp edge roll-off, and demonstrate at least 90% signal suppression. Angles for the new pulses were determined by iteratively adjusting from a 90°/90° combination with each pulse type until signal suppression was minimized. The resulting angles were 90°/160°, 135°/135°, and 135°/135° for the FM, SINC, and REST pulse combinations, respectively. Spoiling gradient durations

were maximized to the 40 mT/m system limit and a duration of 16 ms to sufficiently dephase signal that potentially would produced fold-over artifacts. The achieved B_1 amplitudes and durations were 8.32 μT/15 μT with 8.63 ms durations for the FM pulses, 15 μT and 6.16 ms durations with SINC pulses, and 15 μT and 4.12 ms with REST. Respective preparations times for each case were 76, 52, and 60 ms.

2.5 Combination of OVS and IVI for Rapid 3D EPI Acquisitions

Reduced-FOV methods such as IVI are known to produce a loss in SNR for multi-slice acquisitions due to saturation of neighboring slice positions when localizing to a target region. However, this effect is not expected for 3D scans which excite the entire slice volume each acquisition within a specific repetition time. The additional obtained slices in 3D scans are beneficial not only due to the increased coverage provided, but also result in improved SNR. Phase encoding is also performed in two dimensions, which for some coils is readily accelerated in both directions using parallel imaging methods. However, 3D volumes if constrained within the object dimensions rely on sharp end profiles to prevent fold-over artifacts from occurring. Often, oversampling factors are applied to extend the obtained number of slices beyond the pulse restricted profile to account for pulse roll-off that could resulting in aliasing effects, increasing scans times by as much as 40% to 80%. In some applications, the entire object is sampled instead.

To address this, simultaneous constraint of the in-plane FOV and sharpening of end volume profiles is achieved by combining the described IVI and OVS techniques for 3D scans (Fig. 5.3). Here, the x-dimension profile is constrained by IVI, the y-dimension is restricted by use of intrinsic anti-aliasing filters, and the

volume profile is improved by adding OVS saturation bands at the end of the volume using the method described previously. This combination is intended to rapidly accelerate 3D scans by reducing the FOV in both the slice and in-plane phase encoding dimensions, further suppressing unwanted external slice signal that may otherwise fold into volume slices, with potential reduction of over-sampling factors [25]. The proposed technique potentially enables several slices to be obtained constrained within a smaller sub-volume of an object without relying on multi-slice scans where IVI performance may be degraded.

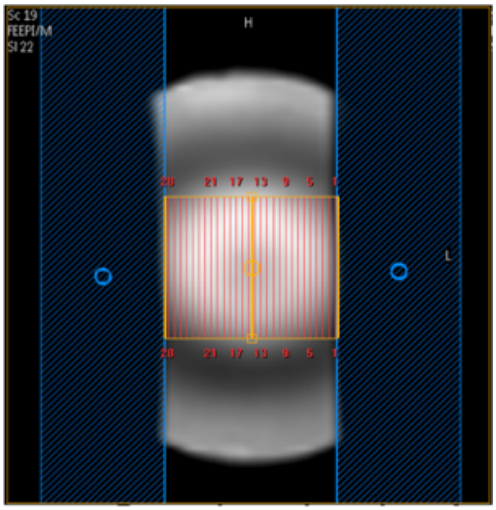

Figure 5.3 – Placement of OVS saturation bands at end of 3D volume using EPI confined by IVI, and SENSE along both phase encode dimensions.

3. EXPERIMENTAL METHODS

3.2 Human Imaging Experiments

All experiments were performed using a 7 Tesla Philips Achieva System (Philips Healthcare, Cleveland, Ohio) and a Nova 32 channel parallel receive head coil with separate quadrature volume transmission (Nova Medical, Wilmington, MA). The 7T system has a 60 cm bore size, maximum gradient strength of 40 mT/m, slew rate limit of 200 mT/m/ms, and the peak B_1 amplitude was limited to 15 μT. Human scans were performed on awake male and female healthy subjects between the ages of 20 and 54, with females of child-bearing age screened for a negative

pregnancy test result. Each subject provided informed consent as defined by the Institutional Review Board (IRB) protocol approved by the Vanderbilt University Medical Center (Nashville, TN). The phantom scans described for protocol optimization were performed using an agar gel FBIRN (Functional Biomedical Information Research Network) with a 17 cm diameter.

3.3 Assessment of SENSE and Reduced-FOV Combination for Rapid Imaging

Prior to performing human imaging scans, two phantom experiments were performed to compare parallel imaging and reduced-FOV techniques and synergistically optimize the combination of both rapid methods. In the first experiment, 10 independent acquisitions of a phantom were acquired across a range of SENSE factors, 'R', from 1 to 8 with no rFOV preparation. The same scan was then repeated reducing the phase encoding dimension size using IVI by a factor 'Z':

$$Z = \frac{FOV_{FULL}}{FOV_{RFOV}} \qquad 5.14$$

SNR was measured for both scans across the 10 acquisitions as the mean signal over the standard deviation at each pixel location. Mean SNR at each independent R and Z value was then computed in the non-zero pixel locations at each factor.

In the second experiment, SENSE and IVI based reductions were simultaneously applied to obtain a total reduction, R_{TOTAL}, of 8, which corresponds to the product of R and Z. The SENSE factor was incrementally increased from 1 to 8 and the IVI factor correspondingly decreased to always maintain the same R_{TOTAL}. As with the prior experiment, 10 independent acquisitions were acquired at each R and Z combination that spanned from fully SENSE to fully IVI accelerated. SNR was

calculated as described, with mean SNR values computed. The resulting profile across R and Z values was inspected to determine the point of maximal SNR.

3.4 High Resolution Imaging Using IVI Reduced-FOV

The optimized parallel imaging SENSE-IVI technique was applied with an EPI readout for human imaging experiments to achieve the following objectives:

1. Compare relative image quality between IVI rFOV imaging and full SE scan using multi-shot EPI at 500, 300, and 160 μm in various brain regions.
2. Compare relative image quality between IVI reduced-FOV scans and a full SE scan with single shot EPI at 500 and 300 μm in various brain regions.
3. Demonstrate image quality obtained by using IVI in high resolution scans ranging from 160 to 300 μm and with 1 to 2 mm slice thicknesses.
4. Apply SENSE-IVI and EPI to target the hippocampus using small 40x40mm FOV sizes for 160 to 500 μm image resolutions.

The regions targeted for the first two tests consisted of the frontal cortex, midbrain at the level of the substantia nigra, lentiform, thalamic region, and midbrain with bilateral coverage of the hippocampus, with imaging parameters summarized in Table 2. Full and reduced images collected with multi-shot and single-shot EPI were compared in these regions at the specified resolutions by cropping the full data to the same position and dimensions as the reduced data set. Both sets were acquired with parameters configured to result in approximately the same SNR and scan duration by adjusting the number of acquisitions. For multi-shot EPI, the applied EPI factor was matched between the two data sets, with the partial fourier halfscan percentage value maximized when necessary to achieve target TE values at higher

resolutions. Comparison focused on relative SNR, scan time, contrast, feature distinction, and presence of blurring, motion, or distortion artifacts in each image region between matched resolutions. A similar assessment was performed for the IVI high-resolution data in the range from 160 to 300 μm as well as the targeted hippocampus data to determine relative changes in image quality across the resolutions acquired. Hippocampus assessment focused additionally on identification of sub-regions or layers across the various resolutions. Where obtained, larger FOV bilateral midbrain hippocampal images were cropped to localize the hippocampus at the various resolutions for additional assessment of images and identification of hippocampus features.

Table 2 – Scan Parameters for Human Parallel Reduced-FOV EPI Scans

Region	TR/TE *(ms/ms)*	NSA	EPI *(F)*	SENSE *(R/S)*	IVI *(Z)*	R_{TOTAL} *(F•R•S•Z)*	Voxel Size *(mm x mm x mm)*	FOV Size *(PE x RO)*	WFS *(pixel)*	TA *(m:s)*
Ventricle	3000/76	22	23	2.0	3.50	161	300x300x3.0	60x60mm	55.57	4:33
	3000/76	6	23	2.0	1.00	46	300x300x3.0	210x210mm	68.28	4:39
Lentiform	3000/76	22	23	2.0	3.23	149	300x300x3.0	65x65mm	60.26	4:33
	3000/76	6	23	2.0	1.00	46	300x300x3.0	210x2100mm	72.31	4:39
Hippocampus	3000/76	18	23	2.0	2.63	121	300x300x3.0	60x80mm	50.36	4:35
	3000/76	6	23	2.0	1.00	46	300x300x3.0	210x210mm	68.28	4:39
Brainstem	3000/72	14	19	2.0	3.23	123	300x300x3.0	65x65mm	58.04	3:40
	3000/72	4	19	2.0	1.00	38	300x300x3.0	210x210mm	61.79	3:45
Cortex	3000/64	18	23	2.0	3.50	161	300x300x3.0	60x60mm	50.36	4:39
	3000/64	5	19	2.0	1.00	38	300x300x3.0	210x210mm	58.77	4:39
Transverse SS	2000/107	16	87	2.0	1.00	174	500x500x3.0	210x210mm	102.48	36s
	2000/110	20	25	2.0	4.88	244	500x500x3.0	210x43mm	30.83	44s
Thalamus SS	3000/80	28	214	2.0	1.00	428	500x500x3.0	210x210mm	377.73	1:30
	3000/80	28	63	2.0	3.50	441	500x500x3.0	60x60mm	93.26	1:29
	2000/85	49	129	2.0	3.50	903	240x240x3.0	60x60mm	359.92	2:28
Cortex SS	3000/68	90	107	2.0	4.20	899	240x240x3.0	50x50mm	296.15	4:29
OVS SS	500/14	180	63	2.0	3.50	441	500x500x2.0	60x60mm	113.67	1:31
OVS Regions	500/12	104	23	2.0	3.50	161	300x300x3.0	60x60mm	69.86	3:31
IVI-OVS MS	1238/76	5	23	2.0/2.0	3.50	322	300x300x3.0	60x60	55.57	5:40
	3000/76	2	23	2.0/2.0	3.23	297	500x500x3.0	65x65	41.54	2:55
IVI-OVS SS	3000/76	4	53	2.0/2.0	4.20	890	500x500x2.0	50x50	78.70	2:58
	3000/76	8	85	2.0/2.0	4.20	1428	300x300x2.0	50x50	210.09	6:44

Table 2 – Scan parameters for IVI reduced-FOV comparison using multi-shot EPI readout sequence in various human brain regions at 500, 300, and 160 μm.

3.5 Gradient Echo Imaging of the Human Brain Using OVS

Use of the three pulse options for OVS to reduce SAR applied was tested in human subjects to visibly determine that suppression was maintained. This was accomplished by collecting images in a 60x60 mm region centered on the lentiform using sequence with a single shot EPI readout. The frequency modulated, REST, and SINC pulses were individually applied with the scanner calculated SAR value recorded expressed as a percentage of the 3 W/kg limit for the head. This assessment was used to define the pulse applied for subsequent imaging of the head using OVS, which implemented the pulse that produced the lowest SAR values without any visible foldover in the collected images. The optimized OVS was applied with a gradient echo sequence using a multi-shot EPI readout and SENSE to collect 300 μm images of the brain targeting the lentiform, frontal cortex, and a cortical region overlapping the visual area. Regions were assessed for established contrast, visibility of features, and extent of diminished FOV artifacts in the localized area.

3.6 Rapid 3D Imaging Using a Combination of IVI and OVS

The described 3D imaging protocol was tested in human subjects using a mutli-shot and single-shot EPI readout. The imaged volume targeted separately 20 slices through transverse and sagittal views of the midbrain area, spanning across the ventricles and thalamus for the former, and down through the lentiform to the substantia nigra in the latter. Here, a 60x60 mm in plane FOV was constrained using the IVI method, with additional OVS saturation bands placed at the end of the 3D slice stack using the SINC pulse. For each region, 500 and 300 μm resolutions were acquired with 2 mm slice thicknesses and SENSE acceleration along both the

slice selective and x direction phase encoding dimensions. Oversampling factors were applied at values of 1.4 and 1.1. Slice images were inspected for residual fold-over artifacts, general contrast, and feature quality within each region.

4. RESULTS

4.2 Assessment of SENSE and Reduced-FOV Combination for Rapid Imaging

Both SENSE and reduced-FOV based acceleration produced comparable SNR losses up to a reduction of approximately five, beyond which, IVI had a higher SNR than SENSE, as much as seven times for 10-fold accelerations (fig. 5.4). This was a result of increasing g-factor values for SENSE, which was visible as high

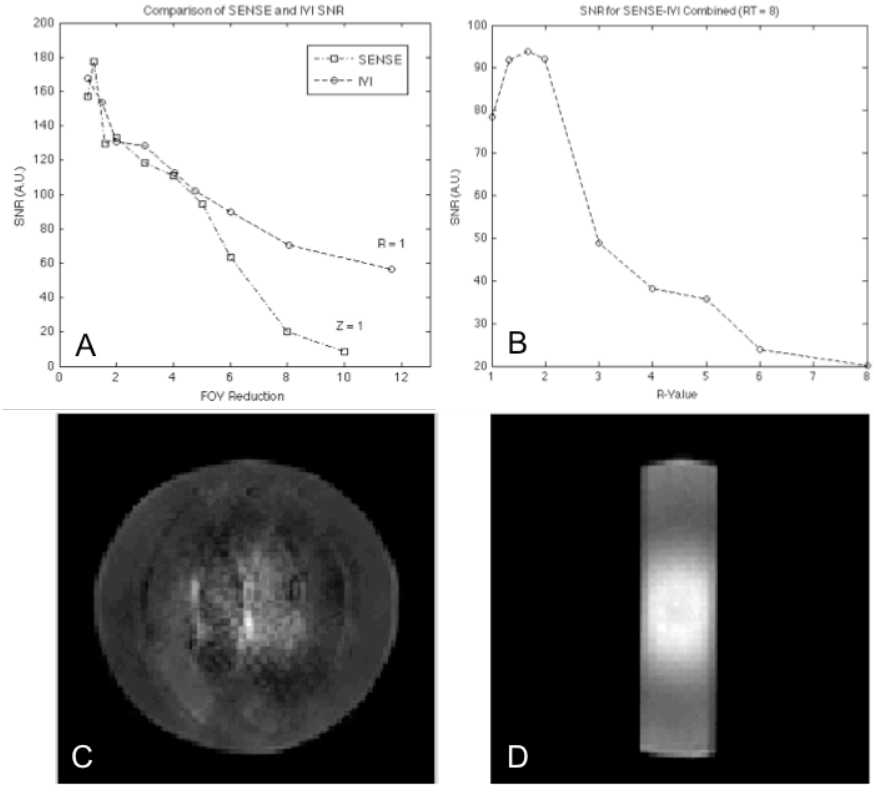

Figure 5.4 – A.) SNR measured across reduction using SENSE and IVI only. B.) SNR measured with combined SENSE and IVI to achieve total reduction of 8, with increasing contribution of SENSE. Phantom image with C.) R = 8, Z = 1. D.) R = 1.68, Z = 4.77

noise artifacts in the SENSE reconstructed image relative to the uniform appearance of rFOV images confined to narrow slabs (fig 5.4 C, D). Combining SENSE and IVI, the lowest SNR was observed with fully SENSE accelerated scans and no IVI FOV reduction. The highest SNR occurred at R = 1.68 and Z = 4.77, with SNR between R = 1.5 and 2.5 higher than the fully IVI accelerated case with R_{TOTAL} of 8 (fig 5.4B).

4.3 Comparison of Full-FOV and Reduced-FOV IVI for Human Imaging

Comparisons between IVI reduced-FOV images and full acquisitions are presented in figure 5.5. In sagittal midbrain images through the third ventricle and thalamus into the brain stem, cropped full acquisitions (figure 5.5 D-F) demonstrate notable motion artifacts that degrade visible features, significantly at 160 μm. Motion artifacts are in contrast absent from the IVI images across all resolutions. Specific contrast is achieved in the mammillary bodies, anterior commissure, red nucleus, pons, superior and inferior colliculus, and thalamic region, with fine vasculature apparent at 300 μm, diminished at 160 μm. Similar comparisons of transverse images of the lentiform region (Figure 5.5 G-L) demonstrate consistent appearance between the IVI and cropped full images across all three resolutions. No visible motion artifacts or distortions are apparent, with good contrast between the globus palidus, putamen, internal capsule, and pulvinar. Fine vasculature and internal capsule striations become visible at 300 μm, but are diminished at 160 μm.

The frontal cortex region demonstrates consistent image quality between the IVI and full data sets, with distinct contrast between gray and white matter, and cerebral spinal fluid. Fine white matter striations with local stripes of CSF become localized at 300 μm, as well as fine vessels passing through the ventricle not visible

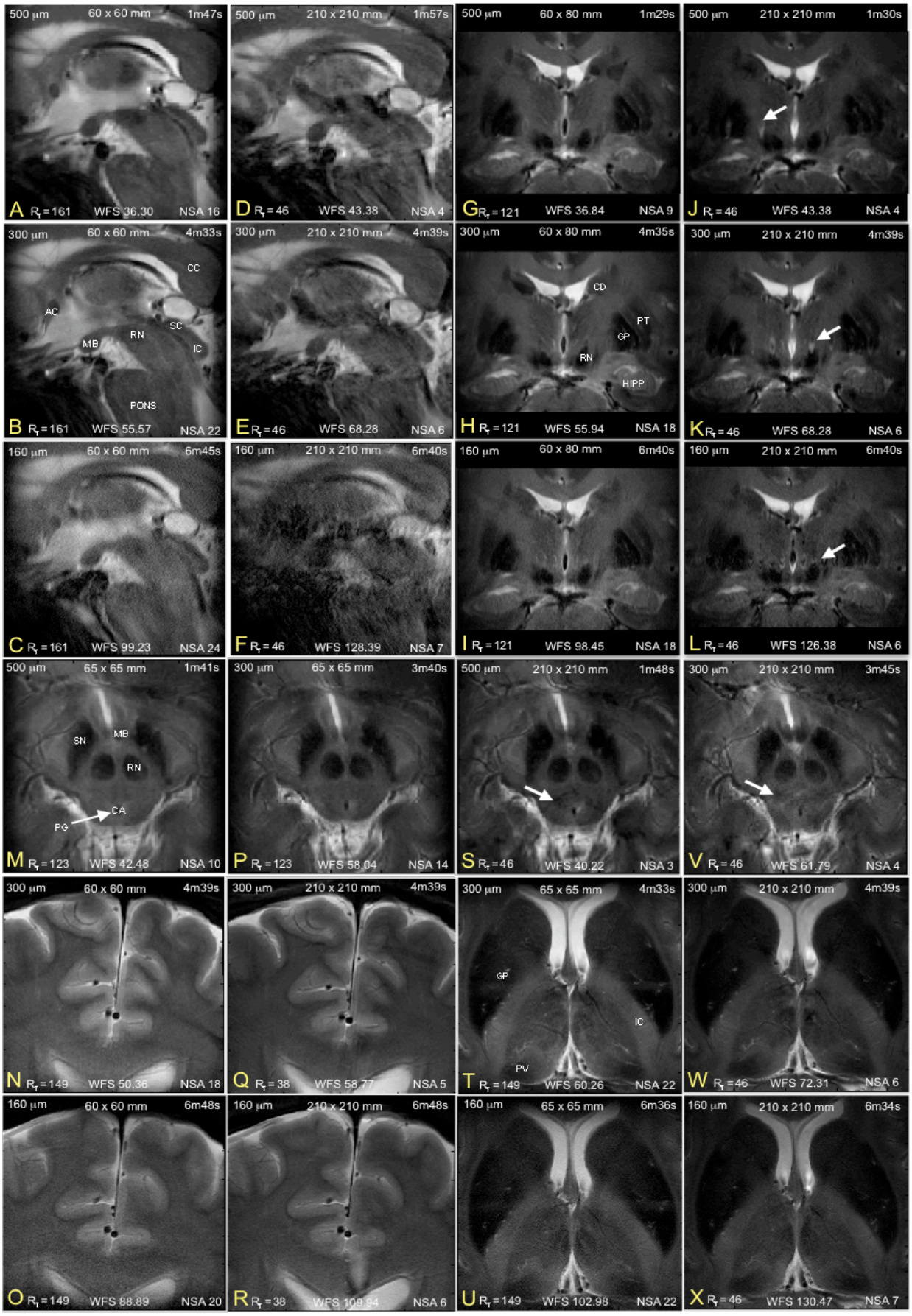
500 µm 60 x 60 mm 1m47s
A Rt = 161 WFS 36.30 NSA 16
500 µm 210 x 210 mm 1m57s
D Rt = 46 WFS 43.38 NSA 4
500 µm 60 x 80 mm 1m29s
G Rt = 121 WFS 36.84 NSA 9
500 µm 210 x 210 mm 1m30s
J Rt = 46 WFS 43.38 NSA 4
300 µm 60 x 60 mm 4m33s
CC
AC
SC
RN
MB
IC
PONS
B Rt = 161 WFS 55.57 NSA 22
300 µm 210 x 210 mm 4m39s
E Rt = 46 WFS 68.28 NSA 6
300 µm 60 x 80 mm 4m35s
CD
PT
GP
RN
HIPP
H Rt = 121 WFS 55.94 NSA 18
300 µm 210 x 210 mm 4m39s
K Rt = 46 WFS 68.28 NSA 6
160 µm 60 x 60 mm 6m45s
C Rt = 161 WFS 99.23 NSA 24
160 µm 210 x 210 mm 6m40s
F Rt = 46 WFS 128.39 NSA 7
160 µm 60 x 80 mm 6m40s
I Rt = 121 WFS 98.45 NSA 18
160 µm 210 x 210 mm 6m40s
L Rt = 46 WFS 126.38 NSA 6
500 µm 65 x 65 mm 1m41s
SN
MB
RN
CA
PG
M Rt = 123 WFS 42.48 NSA 10
300 µm 65 x 65 mm 3m40s
P Rt = 123 WFS 58.04 NSA 14
500 µm 210 x 210 mm 1m48s
S Rt = 46 WFS 40.22 NSA 3
300 µm 210 x 210 mm 3m45s
V Rt = 46 WFS 61.79 NSA 4
300 µm 60 x 60 mm 4m39s
N Rt = 149 WFS 50.36 NSA 18
300 µm 210 x 210 mm 4m39s
Q Rt = 38 WFS 58.77 NSA 5
300 µm 65 x 65 mm 4m33s
GP
IC
PV
T Rt = 149 WFS 60.26 NSA 22
300 µm 210 x 210 mm 4m39s
W Rt = 46 WFS 72.31 NSA 6
160 µm 60 x 60 mm 6m48s
O Rt = 149 WFS 88.89 NSA 20
160 µm 210 x 210 mm 6m48s
R Rt = 38 WFS 109.94 NSA 6
160 µm 65 x 65 mm 6m36s
U Rt = 149 WFS 102.98 NSA 22
160 µm 210 x 210 mm 6m34s
X Rt = 46 WFS 130.47 NSA 7

Figure 5.5 (Previous Page) – A-C) IVI sagittal ventricle at 500, 300, 160 μm, matching full images cropped (D-F). G-I) IVI coronal midbrain with bilateral hippocampus, 500, 300, 160 μm, matching full images cropped (J-L). M,P) IVI substantia nigra at 500 and 300 μm, matching full images cropped (S,V). N,O) IVI frontal cortex images at 300 and 160 μm, cropped full cortex images (Q,R). T,U) IVI transverse lentiform, 300, 160 μm, matching full images cropped (W,X). Noise apparent in full images in the sagittal ventricle, coronal midbrain with visible ghosting, and substantia nigra, absent or diminished in the IVI.

500 μm. Image quality is again distinct between full and IVI acquisitions when comparing coronal midbrain images with bilateral view of the hippocampi. Full images show a pronounced ghosting artifact of the ventricles across the slice, diminished in the IVI images. Here, the globus palidus, putamen, and internal capsule are again distinctly defined, as well as the red nucleus. The hippocampus in both hemispheres demonstrates visibility of layers pronounced at 300 μm in the IVI image, but degraded in the cropped full images.

Lastly, transverse images of the midbrain (figure 5.5, M, P, S, V) produce contrast of the substantia nigra, red nucleus, mammillary bodies, peduncles, cerebral aqueduct, and periaqueductal gray. The full images demonstrate a corrupting noise below the red nucleus that is absent with IVI images. As with the prior regions, this area shows primarily an improvement in vasculature visibility with resolution improvement. Specific use of SPIR fat suppression demonstrated no visible fat fold-over artifacts in the reduced IVI data sets. Overall across all regions, scan times ranged from 1m30s for 500 μm data, 4m 30s for 300 μm, and 6m 40s for 160 μm. The total achieved acceleration for the IVI reduced data was approximately 122 fold compared to a factor 46 acceleration for the full data set which applied SENSE and EPI only. FOV reduction accounted for additional 3.5 factor

acceleration in the scan times, with a single acquisition acquired in 57 sec for a full acquisition versus 17 sec for the reduced case at a resolution of 160 μm.

4.4 Comparison of Single-Shot EPI using Full-FOV and Reduced-FOV IVI

The relative performance of full image acquisition and use of IVI with a single shot EPI readout are presented in figure 5.6. Here, C-E demonstrate the relative appearance of the full transverse slice compared to 42 mm IVI slabs centered on the slice midline and left edge. The full image has notable geometric distortion pronounced at the object edges despite application of a SENSE factor of 2 that is visibly reduced in the IVI data with greater consistency to the expected shape in these regions. The 42 mm width corresponds to a five-fold reduction in the FOV, combined with the simultaneous SENSE factor of 2, results in a 10-fold total reduction, with the water-fat-shift (WFS) reduced 3.3 times and the EPI factor diminished to 25. Figure 5.6 also shows the relative image appearance in a sagittal view through the ventricles, comparing the full image (A), cropped (B) then imaged using IVI (F). The full and cropped image demonstrate significant distortion at the frontal cortex and brain stem, with visible stretching and hyper-intensity that results in loss of portions of the pons. This is notably reduced using IVI and SENSE in the 60x60 mm FOV, which corresponds to a 3.5 reduction factor, seven total due the combination with SENSE, with the WFS reduced 4 fold.

IVI across 500, 300, and 240 μm largely maintains quality of the ventricles, corpus collosum, thalamic area, and large blood vessels. However, stretching of the mammillary bodies is apparent as the resolution is increased with the pons and brain stem distorting to create the increasing hyper-intensity near the cerebellum. These

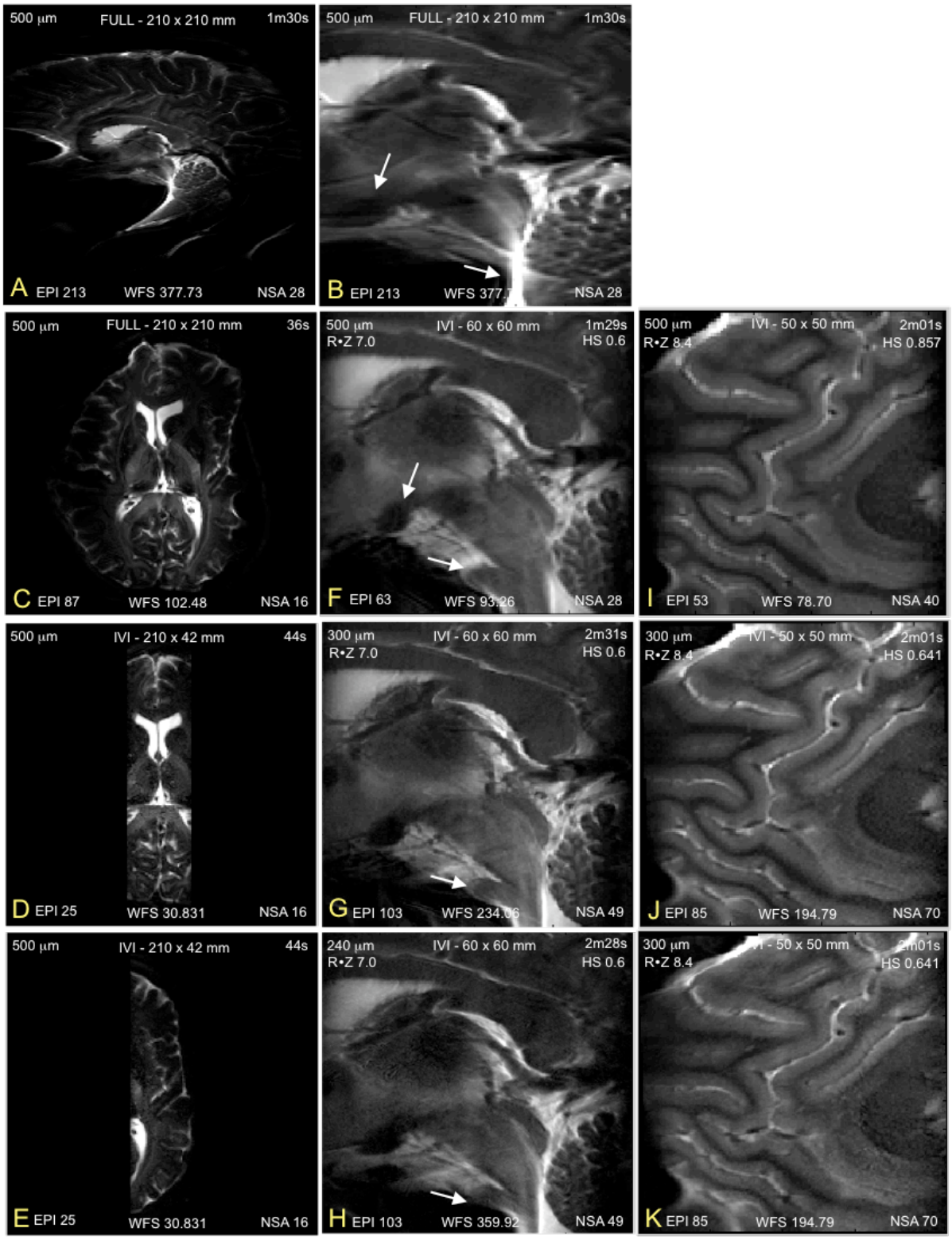

Figure 5.6 – A.) Full sagittal view using single shot EPI with SENSE R = 2, cropped (B).to region imaged using IVI at 500 μm (F), 300 μm (G), and 240 μm (H) with FOV reduced by factor of 3.5. Transverse single shot EPI image at full 210x210 mm FOV (C), imaged using IVI with 210x42 mm FOV centered on midline (D) and right edge (E). I-K) IVI images of sagittal frontal cortex at 500 and 300 and 240 μm with 50x50 mm FOV size.

effects with IVI up to 240 μm are less pronounced than the full image at 500 μm. Likewise, the frontal cortex acquired using the single shot EPI with IVI-SENSE in a 50x50 mm FOV demonstrates consistency again at 500, 300, and 240 μm resolutions, with good contrast between grey and white matter, as well as the CSF, with visibility of the corpus collosum and no notable distortion.

4.5 High Resolution Imaging of the Human Brain Using IVI with Multi-Shot EPI

Localized brain images with resolutions ranging from 160 to 300 μm and 1 to 2 mm slice thickness using SENSE-IVI with multi-shot EPI are presented in fig. 5.7. The imaging focuses on regions explored for the single and multi shot comparisons. Sagittal images of the medial hemisphere surface passing through the third ventricle provide coverage of the cingulate cortex with visibility of the pericallosal artery and branches. These branches are narrowly defined with a decrease in slice thickness as well as at the higher 180 μm resolution. Geometric distortion of the pons is apparent at all three resolutions, with visible contrast in the cerebellum, and definition of the choroid plexus at the center of the image. Likewise, the transverse images provide localization of the head of the caudate nucleus, anterior nucleus, thalamus, internal capsule, pulvinar and putamen. Hyper-intensities external to the third ventricle is indicative of Virchow-Robin spaces. These spaces are also well resolved in 160 μm frontal cortex images at three different slice thicknesses, with a diminished grey and white matter contrast. 200 and 240 μm images of the transverse midbrain again isolate the red nucleus and substantia nigra, with visibility of the internal carotid and posterior cerebral arteries. Scan times range from 2m54s to 12m01s, with the FOV reductions spanning factors from 2.1 to 3.5.

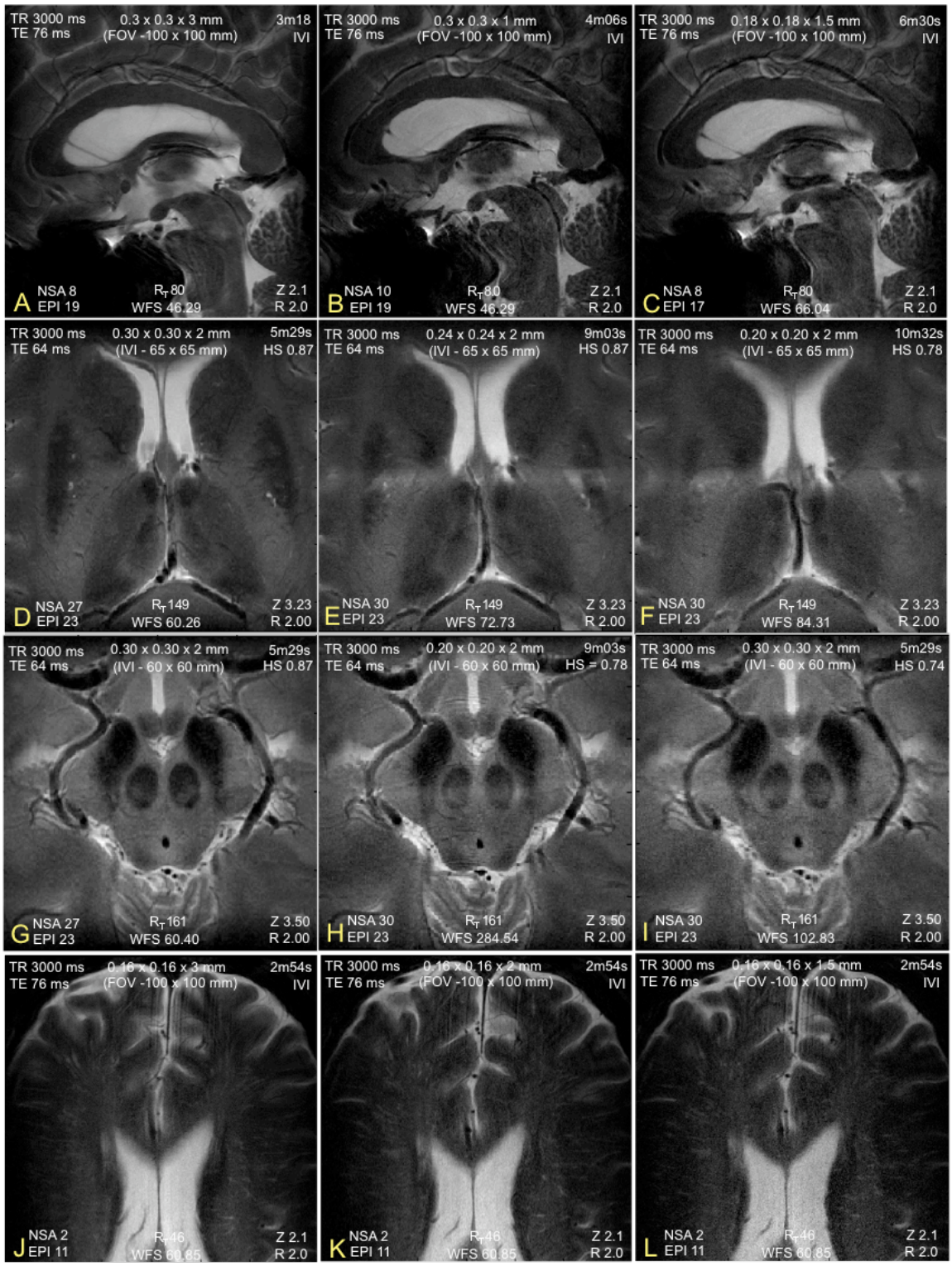

Figure 5.7 – High resolution IVI images: A) Sagittal view of midbrain at 0.3x0.3x3 mm, lowered to 1 mm slice thickness (B), and repeated at 0.18x0.18x1.5 (C). Lentiform imaged at 300 μm (D), 240 μm (E), and 200 μm (F). Transverse midbrain at 2 mm slice thickness and 300 μm (G), 200 μm (H), and 160 μm (I) resolutions. Frontal cortex with 160 μm resolution and 3 mm (J), 2 mm (K), and 1.5 mm (L) slice thicknesses.

4.6 Small-FOV High Resolution Hippocampus Imaging Using IVI

Multi-slice IVI acquisitions of coronal bilateral hippocampus images are presented in figure 5.8, with six slices obtained at 500 μm, and three slices at 350 μm. Slice numbers were maximized to that obtainable within SAR constraints while maintaining one interleave package. Despite expected signal losses with IVI due to saturation by selective pulses of spins in neighboring slices, both resolutions produced sufficient image quality to localize features identified in prior single slice acquisitions. However, imaging acquisition times were increased to compensate for diminished SNR from 1.5 minutes to 5 minutes and 4.5 minutes and 9 minutes for the 500 and 350 μm resolutions, respectively. Single slice images localized to one hippocampus in 40x40 mm FOV corresponding to a 5.25 reduction in the FOV combined with SENSE R of 2, produced images with no apparent distortions or

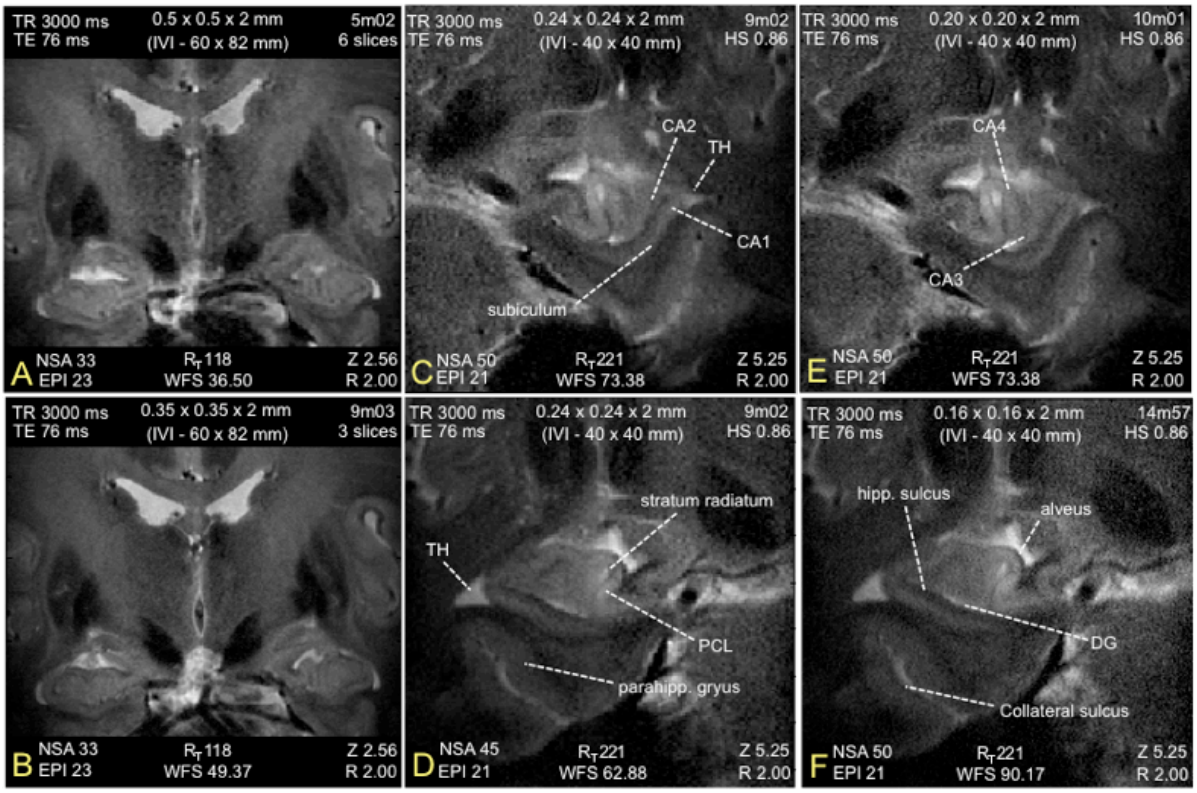

Figure 5.8 – A.) IVI 6 slice acquisition of coronal hippocampus at 500 μm, B.) three IVI slices at 350 μm. C.) 240 μm hippocampus with 2 mm slice thickness reduced to 40x40 mm using IVI, repeated at 160 μm (E). IVI contralateral hippocampus at 240 μm (D) and 160 μm (F).

motion artifacts with scan times ranging from 3 to 15 minutes (Figure 5.7), for 240 μm and 160 μm resolutions. Specific hippocampal features were identified in figures, as indicated by dashed lines (5.8 D,F - left hippocampus, 5.8 C,E - right) including the temporal horn, dentate gyrus, CA1 to CA4, collateral sulculs, alevus, subiculum, pyramidal cell layer, parahippocampal gyrus, and stratum radiatum [10, 26].

4.7 Gradient Echo Imaging of the Human Brain Using OVS

Reduced-FOV images acquired with the OVS technique using a gradient echo sequence are presented in figure 5.9. Comparisons between the FM, REST, and SINC pulses produce consistent appearance in the images with no visible residual fold-over artifacts. At a fixed TR of 1000 ms, the three pulses have SAR values of 87%, 78%, and 34%, respectively, enabling minimum TR values of 874

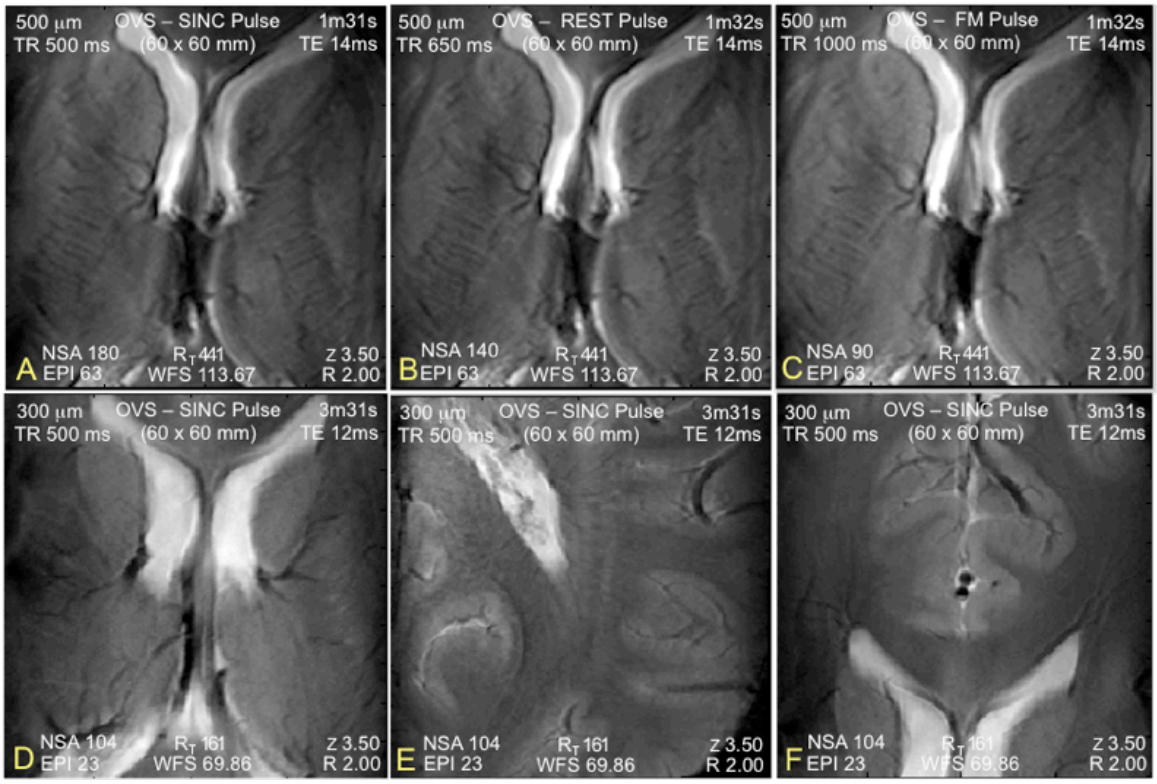

Figure 5.9 – A.) OVS 500 μm images of gradient echo lentiform using A.) FM pulse, B.) REST pulse, C.) SINC pulse, with no visible fold-over artifacts. Scan repeated with SINC pulse at 300 μm in C) lentiform, D.) visual cortex area, E.) frontal cortex.

ms, 564 ms, and 345 ms. Remaining images collected using the lower SAR SINC pulse (Figure 5.9 D-F) maintained performance at 500 and 300 μm resolutions, with T2* weighting established. Gray and white matter contrast is visible, with localization of a striated internal capsule, portions of the visual cortex, corpus collosum, head of the caudate, and the choroid plexus in the third ventricle. Resolution improvements enhanced definition of white matter striations, choroid plexus, and blood vessels passing through the brain midline as well as branches entering visible cortical regions. Scan times were 1.5 minutes and 3.5 minutes for 500 and 300 μm imaging, respectively, with 86 and 104 acquisitions performed.

4.8 Rapid 3D Imaging Using a Combination of IVI and OVS

Single and multi shot EPI images using the combination of SENSE with IVI and OVS for localized 3D imaging are presented in figures 5.10. For both data sets, the sagittal and transverse images demonstrate consistent quality across all 20 slices with sufficient signal at 300 μm to identify a number of features localized in the single slice acquisitions, including the red nucleus, substantia nigra, globus pallidus, putamen, hippocampus, and choroid plexus. The combined FOV reduction from SENSE along two dimensions and IVI is 14, accounting for MS and SS EPI factors, the achieved acceleration is 332 and 1,428, respectively. Additional reduction is provided along the slice dimension by restricting the number of slices to 20 versus full coverage of the object in that dimension. Reducing the OS factor from 1.4 to 1.1 produced consistent image performance with 500 μm 3D images acquired in 2m19s (fig. 5.10C). Likewise, single shot EPI acquisition in demonstrated no visible or additional distortion in this particular region (fig. 5.10D).

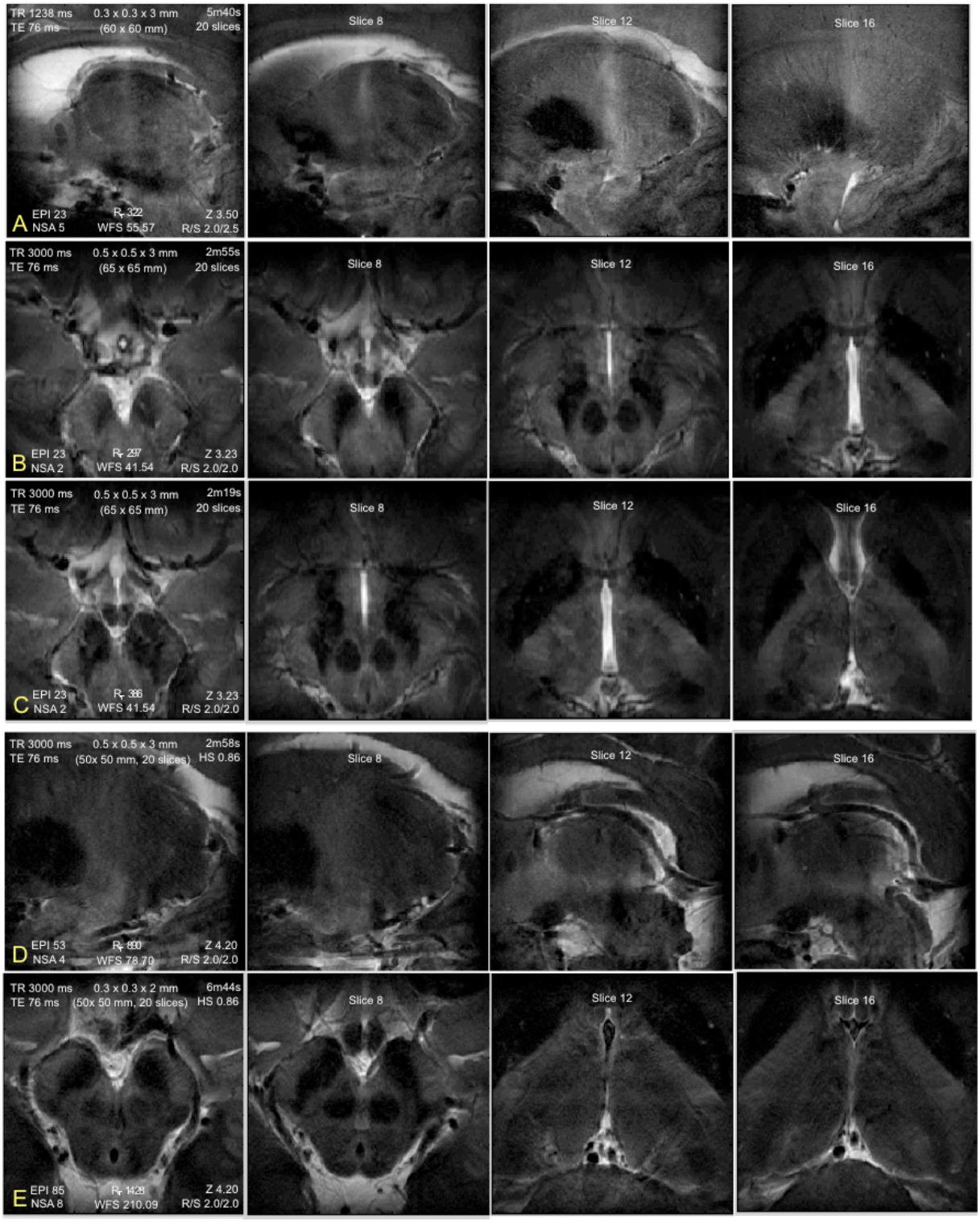

Figure 5.10 – 3D multi-shot EPI combined with IVI-OVS and 2D SENSE acceleration demonstrated to acquire 20 slices with 300 μm sagittal (A), and 500 μm transverse (B) orientation, C.) with transverse OS factor lowered from 1.4 to 1.1. Scans repeated using single shot EPI readout (D, E).

5. DISCUSSION

The combination of SENSE with IVI and OVS based reduced-FOV imaging techniques demonstrated improvement in both single shot and multi shot EPI scans. This was visible in regions where there is an increased amount of susceptibility variation or sensitivity to motion, particularly near sinuses or the brainstem. Any applied FOV reduction, whether SENSE or reduced-FOV based, effectively lowers the number of lines of k-space that must be acquired in a shot, lowering the echo train length. T2* effects have a shorter duration over which dephasing effects can translate to a distortion in the geometry and minimizes potential signal loss. Increments in resolutions would otherwise increase these effects due to the added number of points that must be acquired, both in terms of the readout dimension and added phase encoding lines. A corresponding step down in the FOV size translates into a comparable step up in the achievable resolution to accomplish comparable extent of the artifacts observed. As demonstrated, this trade-off is especially important in single shot EPI scans or those requiring high EPI factors in multi-shot protocols which requires large amounts of data be acquired in a single TR.

Use of SENSE for this protocol assists not only with this reduction but also enables the FOV to be maintained at a slightly larger size while incorporating the IVI or OVS based reduction. At a common SENSE factor of two, this translates to a FOV size two times larger with comparable reduction when combined with rFOV approaches. The added benefit of the measured SNR improvement at this reduction for the FOV sizes tested with IVI further supports the applicability of the combined

SENSE and IVI approach. The enhanced SNR performance here in part may reflect the general benefit of the reconstruction to optimally combine coil intensities when there is acceleration. The g-factor aspect of SENSE based approaches puts an intrinsic limit on the potential reduction achieved using SENSE alone. Increments in field strength and coil element numbers provide a means for lowering these effects. However, at some point, the noise amplification significantly degrades image quality, at a reduction beyond 5 or 6 for the 32 channel array used here. Reduced-FOV methods are not similarly constrained by a g-factor, only by the acceptable SNR loss due to the reduction and the minimum FOV size before desired information is lost.

As long as the FOV size is sufficient to provide coverage of the target area, the reduction losses can be countered by increasing the number of acquisitions while benefiting from the acceleration of each individual acquisition. The comparison data demonstrated the reduced sensitivity to intra-scan motion and susceptibility effects of the IVI images versus full scans while maintaining the same SNR between the comparisons. In this respect, SNR does not have to be sacrificed to achieve improved image performance when targeting localized regions in a small FOV. The resulting improvement in quality that typically would degrade at higher resolutions with full scans enables these resolutions to be targeted up to 160 μm resolutions, as demonstrated here. In these cases, the efficiency improvement does not directly result in a reduction in scan time, but corresponds to an improvement in the obtained quality. Necessitating high numbers of acquisitions to recapture lost SNR further assists with observed quality improvement by diminishing incoherent noise sources when they are combined.

In terms of minimizing scan duration, the fact that each acquisition contributes a smaller amount to the total SNR enables a finer adjustment between scan time and achieved signal quality. In addition, the reductions of artifacts that EPI scans are particularly sensitive to enables higher EPI factors to be targeted for a given resolution and image quality for even faster scans. It likewise enables resolutions to be obtained for anatomical scans that previously would not have been applied due to significant artifact degradation. In this study, 240 μm resolution single shot EPI scans were performed with full scans significantly degraded at 500 μm. Likewise, multi-shot imaging demonstrated 160 μm with no visible features for full scans at these same resolutions due to the presence of significant artifacts.

The use of IVI and OVS enables multiple types of contrast to be obtained to support a variety of studies. IVI in particular, provides T2 weighting of images that uniquely identified a number of features in the regions imaged with susceptibility effects diminished. OVS provides greater flexibility with the image contrast type with T2* weighted images demonstrated here without residual fold-over effects. Power deposition can be typically high with OVS methods; the testing here demonstrates this can be minimized with appropriate pulse selection and optimization. For both IVI and OVS, resolutions ranging from 160 and 300 μm were readily performed with consistent quality throughout the brain. IVI faces the additional unique challenge of off-slice saturation effects that diminish SNR in multi-slice scans. Here we demonstrated quality images can be obtained with multi-slice up to 350 μm, however compensated with additional acquisitions that extend scan durations.

Combining IVI with OVS, SENSE, and EPI with a 3D scan, addresses the multi-slice losses while improving EPI performance for high acceleration without adding acquisitions to improve SNR. The up to 1400-fold improvement in scan time with this combination provided quality images with no discernable distortion artifacts across confined areas of the brain and short overall scan durations. Volume 3D scans provide additional SNR gains by a factor of $\sqrt{N_Z}$ and enable two dimensions of SENSE acceleration. The combination of IVI and OVS provide sharp delineation of the volume boundaries to minimize the number of slices required. This was demonstrated for both multi and single shot acquisitions that provide potential application for both anatomical and functional based volume scans obtained within 2 to 6 minutes. Reduction of over-sampling provides an additional source of duration reduction, with scan times here lowered by 20% with no visible loss in image quality.

The benefit of the described techniques in combination with 7T is the obtainment of improvements in achieved image resolution, demonstrated in the variety of 160 to 300 μm images presented here. In each target area, contrast is visible between grey and white matter regions, with localization of features such as the globus pallidus, putamen, mammillary bodies, hippocampus, choroid plexus, peduncles, cingulate cortex, pons, and cerebellum, with definition of major arteries, their branches, and fine vessels. Localized hippocampus images in a small 40x40 mm FOV highlight the potential for both high resolution and improved image quality using the describe techniques. Lack of visible artifacts or motion effects enabled identification of hippocampal layers and structures including the pyramidal cell layer, dentate gryus, and temporal horn. Specific imaging of this structure could support

study of the effects of a variety of disease states that target or have impacted the hippocampus. The achieved accelerations enabled practical scan times ranging from 2.5 to 15 minutes with this approach.

6. CONCLUSIONS

The described combination of SENSE, reduced-FOV methods IVI and OVS, with multi and single shot EPI provides rapid obtainment of high resolution images in localized human brain regions at 7T for single slice, multi-slice, and 3D scans. This technique diminishes physiological and patient motion effects, reduces susceptibility induced geometric distortions and signal loss, enabling higher resolutions to be targeted and higher EPI factors to be applied compared to full acquisitions. Specific optimization of OVS for diminished SAR with gradient echo scans has been described, and combination of IVI with OVS for rapid 3D scans demonstrated with potential reductions in applied over-sampling factors.

7. ACKNOWLEDGEMENTS

This work is supported by NIH Grant number R01EB000461.

8. REFERENCES

[1] K.P. Pruessmann, M. Weiger, M.B. Scheidegger, P. Boesiger, SENSE: sensitivity encoding for fast MRI, Magn Reson Med, 42 (1999) 952-962.

[2] O. Speck, J. Stadler, M. Zaitsev, High resolution single-shot EPI at 7T, Magma, 21 (2008) 73-86.

[3] D.A. Feinberg, J.C. Hoenninger, L.E. Crooks, L. Kaufman, J.C. Watts, M. Arakawa, Inner volume MR imaging: technical concepts and their application, Radiology, 156 (1985) 743-747.

[4] J. Finsterbusch, Fast-spin-echo imaging of inner fields-of-view with 2D-selective RF excitations, J Magn Reson Imaging, 31 1530-1537.

[5] B.J. Wilm, J. Svensson, A. Henning, K.P. Pruessmann, P. Boesiger, S.S. Kollias, Reduced field-of-view MRI using outer volume suppression for spinal cord diffusion imaging, Magn Reson Med, 57 (2007) 625-630.

[6] T. Chung, R. Muthupillai, Using SENSivity Encoding (SENSE) Acceleration and inner volume imaging (Zoom) techniques to decrease energy deposition and increase image acquisition speed in fetal MR: work in progress, in: Proc. Intl. Soc. Magn. Reson., Honolulu, Hawai'i, 2002.

[7] R.M. Heidemann, F. Fasano, M. Vogler, C. Leuze, J. Pfeuffer, R. Turner, Improving Image Quality by Combining Outer Volume Supression and Parallel Imaging: zoomed EPI with GRAPPA at 7T, in: Proc. Intl. Soc. Mag. Reson. Med., Toronto, Onatrio, Canada, 2008.

[8] R.M. Heidemann, D. Ivanov, R. Trampel, F. Fasano, J. Pfeuffer, R. Turner, Zoomed GRAPPA (ZOOPPA) for Functional MRI, in: Proc. Intl. Soc. Mag. Reson. Med., Stockholm, Sweden, 2010.

[9] T. Breyer, I. Wanke, S. Maderwald, F.G. Woermann, O. Kraff, J.M. Theysohn, A. Ebner, M. Forsting, M.E. Ladd, M. Schlamann, Imaging of patients with hippocampal sclerosis at 7 Tesla: initial results, Acad Radiol, 17 421-426.

[10] B.P. Thomas, E.B. Welch, B.D. Niederhauser, W.O. Whetsell, Jr., A.W. Anderson, J.C. Gore, M.J. Avison, J.L. Creasy, High-resolution 7T MRI of the human hippocampus in vivo, J Magn Reson Imaging, 28 (2008) 1266-1272.

[11] Y. Ge, V.M. Zohrabian, R.I. Grossman, Seven-Tesla magnetic resonance imaging: new vision of microvascular abnormalities in multiple sclerosis, Arch Neurol, 65 (2008) 812-816.

[12] C. Mainero, T. Benner, A. Radding, A. van der Kouwe, R. Jensen, B.R. Rosen, R.P. Kinkel, In vivo imaging of cortical pathology in multiple sclerosis using ultra-high field MRI, Neurology, 73 (2009) 941-948.

[13] J. Moore, M. Jankiewicz, H. Zeng, A.W. Anderson, J.C. Gore, Composite RF pulses for B1+-insensitive volume excitation at 7 Tesla, J Magn Reson, 205 50-62.

[14] J.A. de Zwart, P.J. Ledden, P. Kellman, P. van Gelderen, J.H. Duyn, Design of a SENSE-optimized high-sensitivity MRI receive coil for brain imaging, Magn Reson Med, 47 (2002) 1218-1227.

[15] F. Wiesinger, P. Boesiger, K.P. Pruessmann, Electrodynamics and ultimate SNR in parallel MR imaging, Magn Reson Med, 52 (2004) 376-390.

[16] F. Wiesinger, P.F. Van de Moortele, G. Adriany, N. De Zanche, K. Ugurbil, K.P. Pruessmann, Parallel imaging performance as a function of field strength--an experimental investigation using electrodynamic scaling, Magn Reson Med, 52 (2004) 953-964.

[17] F. Wiesinger, P.F. Van de Moortele, G. Adriany, N. De Zanche, K. Ugurbil, K.P. Pruessmann, Potential and feasibility of parallel MRI at high field, NMR Biomed, 19 (2006) 368-378.

[18] T. Jaermann, G. Crelier, K.P. Pruessmann, X. Golay, T. Netsch, A.M. van Muiswinkel, S. Mori, P.C. van Zijl, A. Valavanis, S. Kollias, P. Boesiger, SENSE-DTI at 3 T, Magn Reson Med, 51 (2004) 230-236.

[19] C.F. Schmidt, N. Degonda, R. Luechinger, K. Henke, P. Boesiger, Sensitivity-encoded (SENSE) echo planar fMRI at 3T in the medial temporal lobe, Neuroimage, 25 (2005) 625-641.

[20] C.F. Schmidt, K.P. Pruessmann, P. Boesiger, Spatial resolution enhancement using sensitivity-encoded echo-planar imaging at 3T in a typical motor paradigm, Computerized medical imaging and graphics : the official journal of the Computerized Medical Imaging Society, 31 (2007) 704-714.

[21] D.J. Larkman, D. Atkinson, J.V. Hajnal, Artifact reduction using parallel imaging methods, Topics in magnetic resonance imaging : TMRI, 15 (2004) 267-275.

[22] Y. Hu, G.H. Glover, Partial-k-space acquisition method for improved SNR efficiency and temporal resolution in 3D fMRI, Magnetic resonance in medicine : official journal of the Society of Magnetic Resonance in Medicine / Society of Magnetic Resonance in Medicine, 55 (2006) 1106-1113.

[23] M. Weiger, P. Boesiger, P.R. Hilfiker, D. Weishaupt, K.P. Pruessmann, Sensitivity encoding as a means of enhancing the SNR efficiency in steady-state MRI, Magnetic resonance in medicine : official journal of the Society of Magnetic Resonance in Medicine / Society of Magnetic Resonance in Medicine, 53 (2005) 177-185.

[24] M.J. Versluis, H.E. Kan, M.A. van Buchem, A.G. Webb, Improved signal to noise in proton spectroscopy of the human calf muscle at 7 T using localized B1 calibration, Magnetic resonance in medicine : official journal of the Society of

Magnetic Resonance in Medicine / Society of Magnetic Resonance in Medicine, 63 (2010) 207-211.

[25] Y. Hu, SERA: A technique to improve the performance of the 3D sequence by reducing aliasing artifacts in edge slices., in: Proc. Intl. Soc. Mag. Reson., Stockholm, Sweden, 2010.

[26] U.C. Wieshmann, M.R. Symms, J.P. Mottershead, D.G. MacManus, G.J. Barker, P.S. Tofts, T. Revesz, J.M. Stevens, S.D. Shorvon, Hippocampal layers on high resolution magnetic resonance images: real or imaginary?, J Anat, 195 (Pt 1) (1999) 131-135.

CHAPTER VI

DTI OF THE HUMAN BRAIN AND IMAGING OF THE CERVICAL SPINAL CORD USING PARALLEL MRI AND REDUCED-FOV TECHNIQUES AT 7T

ABSTRACT

Reduced-FOV methods combined with SENSE parallel imaging and single shot EPI were applied at 7 Tesla to achieve localized spinal cord imaging and diffusion weighted imaging (DWI) and diffusion tensor imaging (DTI) in a variety of targeted human brain regions. The focus of this combination of rapid imaging techniques was to diminish sensitivities of diffusion and spinal cord imaging scans to motion, susceptibility variation, and EPI artifacts at ultra-high field. To accomplish this, the inner-volume imaging (IVI) and outer-volume suppression (OVS) reduced-FOV methods were specifically optimized and applied for the DWI and DTI scans with in-plane single slice resolutions as high as 1 mm^2, using b-values of 1000 s/mm^2, and six diffusion directions and acquisition times of 14 minutes. Mean apparent diffusion coefficient (ADC) and fractional anisotropy (FA) values were measured in a number of fiber tract locations at different resolutions and compared. Additional reduced-FOV imaging was performed in the cervical spinal cord using the OVS technique to obtain 500 and 300 μm resolution images in times of 1.5 to 5 minutes. For both applications, the combined acceleration achieved with the parallel reduced-FOV technique resulted in images devoid of motion and EPI based artifacts in diffusion scans, with high resolution achieved in reduced imaging times. The

higher resolutions resulted in improved localization of fiber tracts, mean FA and ADC values with lowered partial volume effects, and achieved contrast of neurological tissue in the cervical spine. These approaches have broad application for imaging localized anatomical regions at high resolution in reasonable times.

1. INTRODUCTION

A common problem encountered in high-resolution MR imaging is the impact of local field variations caused by B_0 inhomogeneities or rapid susceptibility changes, as well as the effects of physiological and patient bulk motion. These problems result in a number of artifacts that degrade image quality in the form of ghosting, distortion, blurring, and signal dropout that can be severe enough to make image data unusable if not managed or minimized. Certain protocols have a higher sensitivity to these effects due to the nature by which signal is generated and acquired. Diffusion weighted imaging (DWI) and diffusion tensor imaging (DTI), in particular, have constraints on achievable resolution in part due to the need to use single shot methods that avoid ghost artifacts caused by small physiologic or patient motions. Such motions may generate large phase shifts in the presence of the strong gradients used to impart diffusion weighting that induce artifacts.

To partially counter motion sensitivity, DWI and DTI make use of highly accelerated EPI readouts that can acquire full k-space information in a single repetition time. As resolution increases, the number of data points acquired is correspondingly larger, which requires longer echo train lengths relative to T2*

values, resulting in a greater occurrence of image blurring and distortion caused by off-resonance effects. Ultimately, a tradeoff is established between the spatial resolution, signal bandwidth, and the occurrence of EPI based artifacts. Partial compensation can be achieved by using multi-shot EPI to lower the percentage of k-space data covered in a single TR, but multi-shot diffusion imaging typically requires navigator information to correct for phase offsets. Due to low SNR of diffusion-weighted images, resolutions are typically constrained to millimeters with scan durations of 10 to 20 minutes, increasing overall sensitivity to gross movements.

Similar motion and susceptibility constraints occur in high-resolution imaging and diffusion experiments that target the cervical spinal cord. Field variations are often worse because of increased presence of bone surrounding the relatively small cross-sectional profile of the spinal cord. The articulation of the neck, and proximity to the lungs and throat, make these scans additionally sensitive to respiratory, cardiac and swallowing physiological motion as well as bulk motion effects. Application of EPI becomes much more challenging in the presence of high B_0 inhomogeneities. Again, increments in resolution further compound these issues, and diffusion weighted imaging in the spine becomes especially difficult.

To address these imaging constraints, previous authors have applied parallel imaging techniques such as SENSE combined with multiple receiver arrays [1-4]. Here, data set sizes are lowered by a factor of typically two to four, and aliasing artifacts are removed by using sensitivity encoding in the reconstruction. Parallel imaging reduces motion effects, echo train lengths, and EPI artifacts, while potentially enabling higher resolutions for DTI and spinal cord imaging. However,

the reduced SNR from SENSE noise amplification places practical limits on the acceleration achieved to prevent significant loss in image quality.

A number of authors have achieved similar accelerations using reduced-FOV techniques to spatially localize signal to smaller regions of the full FOV [5-10]. This is accomplished using a combination of RF pulses selective along specific dimensions using approaches such as inner volume imaging (IVI) [11], or can be similarly achieved by saturating signal with outer volume suppression techniques (OVS) [5]. As with SENSE, the benefit of using these techniques is lowered data set sizes for a given resolution, potentially diminishing scan times, motion sensitivity, susceptibility effects, and EPI based artifacts. To date, applications of this technique have largely been confined to diffusion imaging measurements in the spinal cord at field strengths of 3T and lower. Introduction of higher field 7T systems provide additional signal strength to improve resolution, but also produces shorter T2* values, greater B1 inhomogeneity, and higher SAR values that have to be managed. Reduced-FOV methods have not previously been applied to improve performance of techniques highly sensitive to motion and susceptibility at 7T and have specific potential benefits for imaging a variety of brain and spinal cord regions.

The goal of this study was to optimize inner-volume imaging (IVI) and outer-volume suppression (OVS) reduced-FOV techniques for diffusion weighted imaging, diffusion tensor imaging in the brain, and for anatomical cervical spinal cord imaging at 7T. The study aimed to combine the reduced-FOV technique with parallel imaging acceleration to achieve higher quality diffusion images in a variety of localized brain regions at high resolution using single shot EPI. The combination of

techniques is intended to reduce artifacts despite the resolution improvements, while making use of the enhanced signal at 7 Tesla. Specific DTI measurements to visualize the organization of fiber pathways in localized brain regions will be performed, as well as observed contrast within the cervical spine.

2. METHODS

2.1 Inner-Volume Imaging Diffusion Weighted Imaging Pulse Sequence

Diffusion weighted imaging (DWI) was combined with an inner-volume imaging (IVI) reduced-FOV technique (figure 6.1) as described by Feinberg [11]. To accomplish this, the standard spin echo DWI sequence was modified to alter the initial 90° pulse to excite selectively along the phase encode dimension. The gradient strength was adjusted match the bandwidth of the RF pulse to select the FOV. Subsequent refocusing by a selective 180° pulse was executed between crusher gradients to eliminate unwanted echoes. The combination of these two

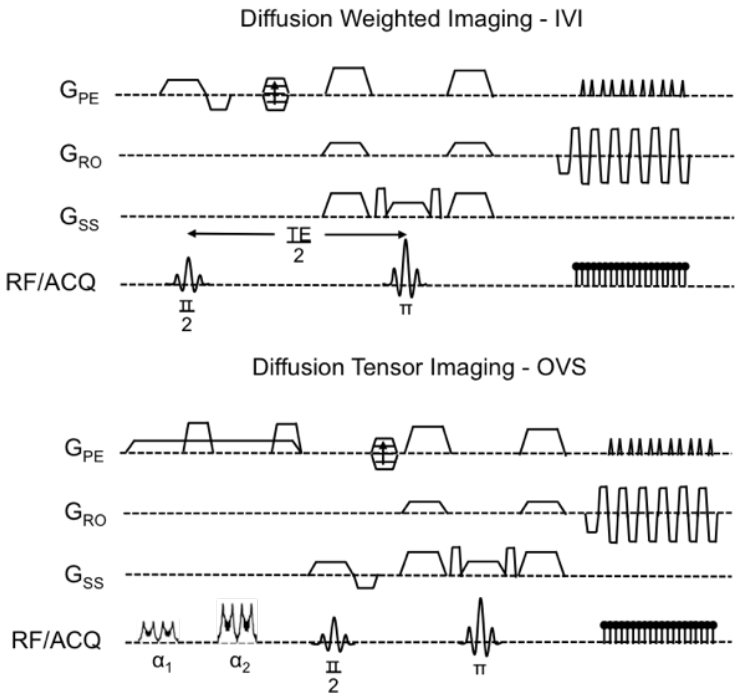

Figure 6.1 – Inner-volume imaging (IVI) and outer volume suppression (OVS) methods for reduced-FOV diffusion weighted scans using a single shot EPI

pulses ensures that only those spins located within their intersection will be diffusion weighted and refocused for imaging. To improve restricted FOV edge sharpness, a five-lobe SINC with 15 μT amplitude and 3.92 ms duration was used for excitation.

2.2 Outer-Volume Suppression Reduced-FOV Pulse Sequence

The combination of an outer volume suppression (OVS) reduced-FOV technique [5] with a diffusion tensor imaging (DTI) sequence, as well as a gradient echo scan for imaging, was accomplished as demonstrated in figure 6.1. Here, the DTI scan consisted of a spin echo sequence with a single shot echo planar (EPI) readout, with a standard cartesian acquisition without EPI applied for the gradient echo scan. OVS was achieved using two repetitions of RF pulses that excited object spins left and right of the desired target area, with the second repetition overlapping the position of the first in a 100 mm wide band. The excited signal was dephased by spoiler gradients set to the system maximum of 40 mT/m and 16 ms durations that occurred between the RF pulse repetitions and at the end of the OVS preparation. Each RF pulse consisted of an FM pulse with linear phase distribution with pulse pairs set to 90° and 160° flip angles. This corresponded to 8.63 ms durations with 8.32/15 μT amplitudes, resulting in a total OVS time of 76 ms.

3. EXPERIMENTAL METHODS

3.1 Human Imaging Experimental Setup

Human imaging experiments were performed on a 7T Philips Achieva System (Philips Healthcare, Cleveland, Ohio) with a 60 cm bore size, maximum gradient

strength of 40 mT/m, slew rate limit of 200 mT/m/ms, and peak B_1 amplitude of 15 μT. Scans were performed on two male and two female subjects between the ages of 20 and 54, with females of child bearing age screened for a negative pregnancy test result. Subjects all provided informed consent as per the protocol described by the Institutional Review Board (IRB) approved by the Vanderbilt University Medical Center (Nashville, TN). Two different coils were used. For DTI brain imaging, a 32 channel Nova receive head array with single volume coil transmission was used; for spine imaging, a 16 channel receive Nova cervical spinal cord array with quadrature saddle coil transmission was applied (Nova Medical, Wilmington, MA).

3.2 Reduced-FOV DTI and DWI in the Human Brain

DTI-OVS and DWI-IVI imaging were both performed using a spin echo scan with single shot EPI that targeted various human brain regions. Performance was specifically demonstrated in the transverse lentiform, brain stem at the level of the red nucleus and substantia nigra, sagittal midline passing through the thalamus, transverse frontal cortex, visual cortex, and coronal midbrain with bilateral visibility of the hippocampus. For both DWI and DTI scans, the FOV size was reduced to dimensions ranging from 60 mm^2 to 90 mm^2 (readout and phase encoding). DTI images were acquired using six diffusion directions along (0, 1, ±1), (±1, 0, 1), and (±1, 1, 0) and a b-value of 1000 s/mm^2, with DWI applied using two directions (0, 0, 0 and 0, 1, 0). In-plane resolutions of 1.0 mm^2 were targeted using 1.0 and 2.0 mm slice thicknesses, with additional 2.0 mm^2 data collected for the DTI scans. Tables 1.1-1.2 summarize the imaging parameters applied, with scan durations of 7m6s and 14m3s for the 2 mm^2 and 1 mm^2 targeted DTI resolutions, respectively.

Table 1.1 – Human DWI-IVI Scan Parameters

Region	EPI	Time *(m:s)*	FOV *(mm^2)*	TR *(ms)*	TE *(ms)*	NSA	Resolution *(mm^3)*	WFS *(pixels)*	b-value *(s/mm^2)*	R
Lentiform	39	1:32	70 x 70	2000	63.68	22	1.0 x 1.0 x 1	19.26	1000	2.0
Cortex	39	2:28	60 x 60	2000	61.77	36	1.0 x 1.0 x 1	57.66	1000	2.0
Coronal	45	2:26	70 x 82	2000	61.79	36	1.0 x 1.0 x 2	13.09	1000	2.0
Midbrain	45	2:26	82 x 70	2000	61.40	36	1.0 x 1.0 x 2	42.47	1000	2.0

Table 1.1 – Scan parameters for four brain regions targeted using diffusion weighted IVI sequence for 1 mm^2 resolutions, two diffusion directions, with b = 0, 1000 s/mm^2.

Table 1.2 – Human DTI-OVS Scan Parameters

Region	EPI	HS	FOV *(mm^2)*	TR *(ms)*	TE *(ms)*	NSA	Resolution *(mm^3)*	WFS *(pixels)*	b-value *(s/mm^2)*	R
Lentiform	27	NA	96 x 80	3000	58.10	20	2.0 x 2.0 x 2	19.26	500	2.0
	51	NA	96 x 80	3000	61.48	40	1.0 x 1.0 x 2	57.66	500	2.0
Midbrain	25	NA	90 x 90	3000	62.10	20	2.0 x 2.0 x 2	13.09	1000	2.0
	47	0.732	90 x 90	3000	65.49	40	1.0 x 1.0 x 2	42.47	1000	2.0
SN Axial	17	NA	90 x 90	3000	59.33	20	2.0 x 2.0 x 2	17.23	1000	2.0
	54	0.732	90 x 90	3000	69.18	40	1.0 x 1.0 x 2	54.00	1000	2.0
Coronal	17	NA	70 x 78	3000	60.98	20	2.0 x 2.0 x 2	11.47	1000	2.0
	54	0.732	70 x 78	3000	64.75	40	1.0 x 1.0 x 2	34.91	1000	2.0
Visual	23	NA	80 x 80	3000	63.75	20	2.0 x 2.0 x 2	14.52	1000	2.0
	43	0.732	80 x 80	3000	67.65	40	1.0 x 1.0 x 2	45.84	1000	2.0

Table 1.2 – Scan parameters for five target brain regions using diffusion tensor imaging OVS sequence with single shot EPI for 1 mm^2 and 2 mm^2 resolutions, six diffusion directions with b-value of 1000 s/mm^2. Halfscan (HS) only applied if resolution resulted in a TE value greater than 70 ms, with highest HS percentage applied for target TE.

3.3 Diffusion Map Image Reconstruction Methods

For each DTI-OVS data set corresponding to a specific localized brain region, diffusion values along each of the six directions were calculated for every pixel [12]:

$$D(i,j) = \frac{\ln(S(i,j)/S_0(i,j))}{-b} \qquad 6.1$$

Here, S_0 corresponds to the non-diffusion weighted signal intensity for b = 0, and S contains the diffusion-weighted intensities along each direction defined by b. From the calculated diffusion values, the apparent diffusion coefficient (ADC) was

determined at each pixel as the mean value of the diffusion matrix trace, with a fractional anisotropy (FA) map generated from the principal eigenvalues (λ_1 λ_2 λ_3):

$$ADC(i,j) = (D_{XX} + D_{YY} + D_{ZZ})/3 \quad 6.2$$

$$FA(i,j) = \sqrt{\frac{1}{2}} \cdot \sqrt{\frac{(\lambda_1 - \lambda_2)^2 + (\lambda_2 - \lambda_3)^2 + (\lambda_1 - \lambda_3)^2}{(\lambda_1^2 + \lambda_2^2 + \lambda_3^2)}} \quad 6.3$$

A color-coded map was then constructed from the FA values and principal eigenvectors for each region to identify fiber tract primary diffusion directions, where red corresponded to right-left, green anterior-posterior, and blue foot-head direction. The color-coded map was used to identify specific fiber tract locations. An ROI was drawn manually and mean ADC and FA values calculated.

3.4 High Resolution Reduced-FOV Imaging of the Human Cervical Spinal Cord

Imaging of the cervical spinal cord was performed using OVS with a gradient echo scan with cartesian readout. An axial slice through the cord was acquired at 500 μm and 300 μm resolutions using a 4 mm slice thickness at a level near the C2 vertebrae. OVS achieved a reduction of the FOV by a factor of 3.0 to 4.2 centered on the cross section of the spinal cord. Fat suppression was accomplished using the Spectral Presaturation with Inversion Recovery (SPIR) technique with an offset frequency of 500 Hz. The applied OVS technique necessitated a TR no shorter than 400 ms, with a TE out of phase with fat of 11.34 ms, and a total of 2 to 6 acquisitions for each of the respective resolutions. A comparable full-FOV acquisition in the same plane was also acquired at 500 μm resolution and two acquisitions, cropped to the spine for comparison, as well as an OVS reduced image of a sagittal view localized on the cerebellum. Images from two subjects were inspected to determine

presence of residual tissue or fat fold-over, gray and white matter contrast in the spinal cord, presence of geometric distortions, and motion artifacts.

4. RESULTS

4.1 Reduced-FOV DTI and DWI of the Human Brain

The reduced-FOV images obtained using both the IVI and OVS approaches for diffusion imaging are presented in figures 6.2-7. Across all regions and resolutions, no visible fold-over artifacts or modulation of signal intensity across the reduced-FOV were observed that was inconsistent with anatomical contrast. FOV reductions corresponded to a 2.6 to 3.5 factor acceleration in acquisition times, 5.2 to 7.0 when combined with a SENSE factor of 2.0. Geometric distortions were insignificant in each of the targeted areas, apparent only in the coronal pons, and as a slight warping of the edge of the frontal cortex and visual cortex. IVI diffusion images (figure 6.2) provided contrast that distinguished gray and white matter, limbs of the internal capsule, and corpus collosum. DTI images using OVS localized a number of prominent fiber tracts and features at the 1.0 mm x 1.0 mm resolution with diffusion orientations matching expected directions based on anatomy, with features labeled in each region figure. These included specifically portions of the corpus collosum (CC), internal and external capsule (IC), optic chiasm (OC), pons, middle and superior cerebellar peduncles (MCP/SCP), fornix (FN), brain stem, optic radiation (OR), substantia nigra (SN), and crus cerebri (CXC). Resolution improvement from 2.0 mm to 1.0 mm produced no change in distortions or artifacts

and improved visualization of a number of tract features, including striations in the internal capsule limbs, corpus collosum, and optic radiation. Smaller tracts such as the optic chiasm and branches in the cerebellum became apparent that were not seen or lacked detail to define at the lower resolution. Hippocampal features were also identified in coronal images, with a sharper pathway boundaries in all areas.

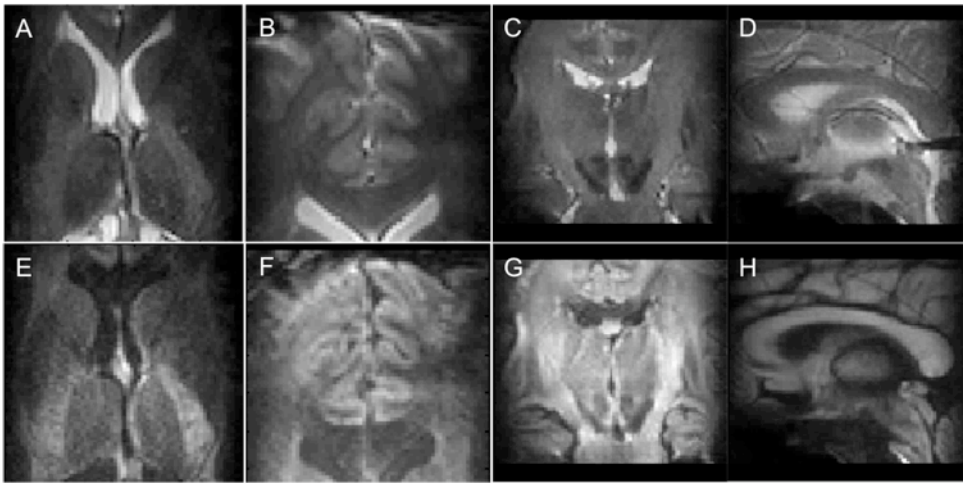

Figure 6.2 – Diffusion weighted IVI of various brain regions at 1 mm^2 for A-D) b = 0, E-H) b = 1000. A,E.) Lentiform, B,F.) frontal cortex, C,G.) coronal bilateral hippocampus, D,H) sagittal midline with view of thalamus and lateral ventricle.

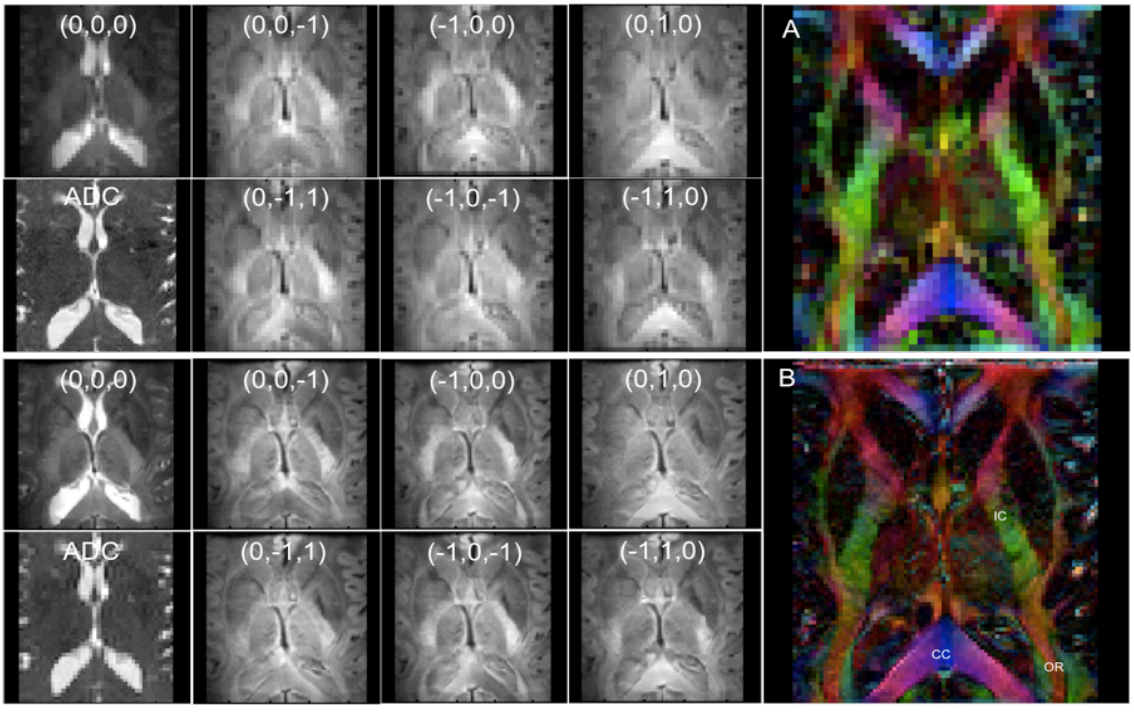

Figure 6.3 – Diffusion weighted OVS transverse images at A.) 2mm x 2mm x 2mm, and B.) 1mm x 1mm x 2mm, showing each diffusion direction for b = 1000 s/mm^2, b=0 s/mm^2 image, ADC map, and color-coded FA map showing principal eigenvectors.

The measured mean FA and ADC values are summarized in table 2 for a number of regions at both resolutions. Overall, mean FA values were 6.7% higher and ADC values 5.5% lower at the 1 mm^2 resolution versus 2 mm^2, indicative of increased partial volume effects on the 2 mm^2 data. In regions that had smaller overall sizes, where partial volume is likely to highly influence values, the difference was pronounced. Specifically, the optic chiasm had a mean of FA of 0.387 at 2 mm^2 versus 0.660 at 1 mm^2 for a 70% difference. Similar differences were seen when attempting to distinguish the periaqueductal grey, substantia nigra, and portions of the hippocampus. In some cases, the ROI was difficult to define due to poor contrast and small size in the low-resolution color-coded vector map. Across all areas, average FA values of 0.625 and ADC of $1.5x10^{-3}$ mm^2/s corresponded well with measurements recorded in prior studies [3].

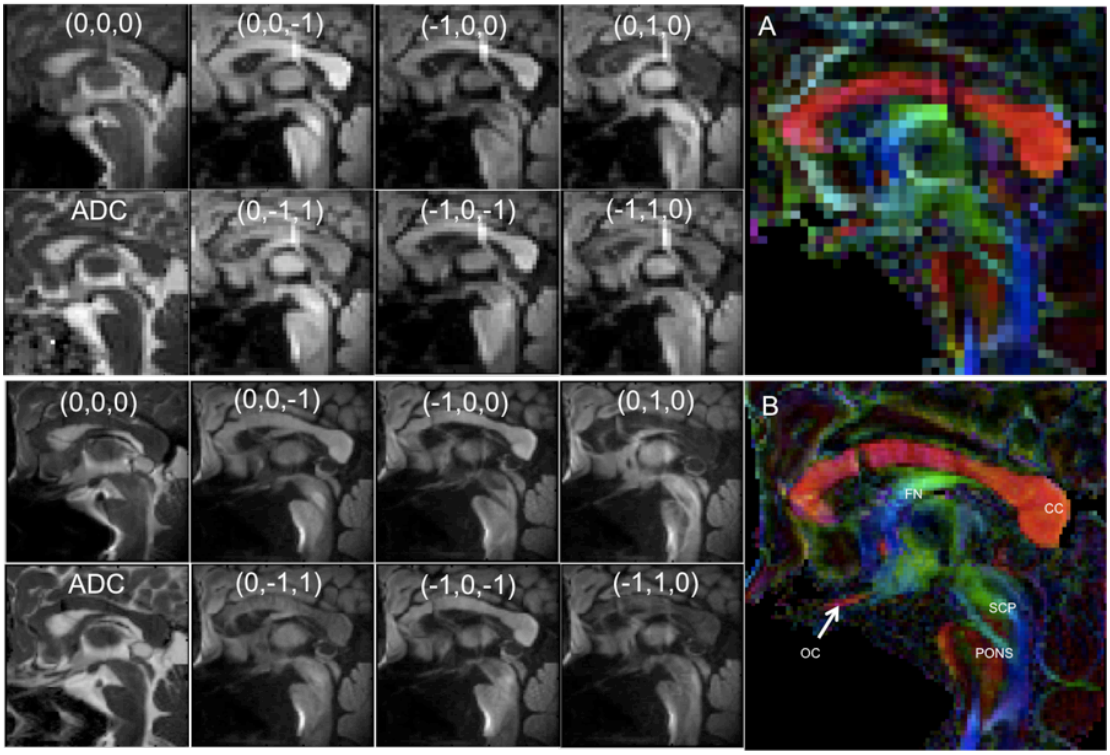

Figure 6.4 – Diffusion weighted OVS sagittal midline images at A.) 2mm x 2mm x 2mm, and B.) 1mm x 1mm x 2mm, showing each diffusion direction for b = 1000 s/mm^2, b=0 s/mm^2 image, ADC map, and color-coded FA map showing principal eigenvectors.

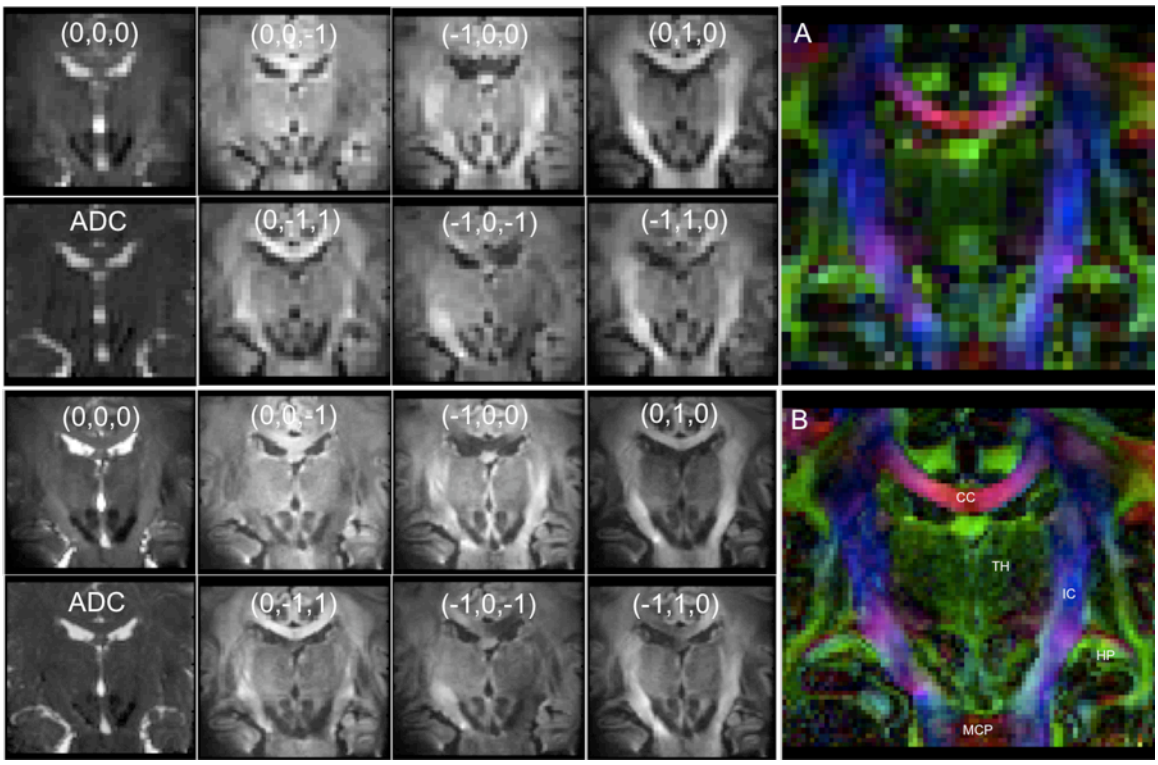

Figure 6.5 – Diffusion weighted OVS coronal hippocampus images at A.) 2mm x 2mm x 2mm, and B.) 1mm x 1mm x 2mm, showing each diffusion direction for b = 1000 s/mm^2, b=0 s/mm^2 image, ADC map, and color-coded FA map showing principal eigenvectors.

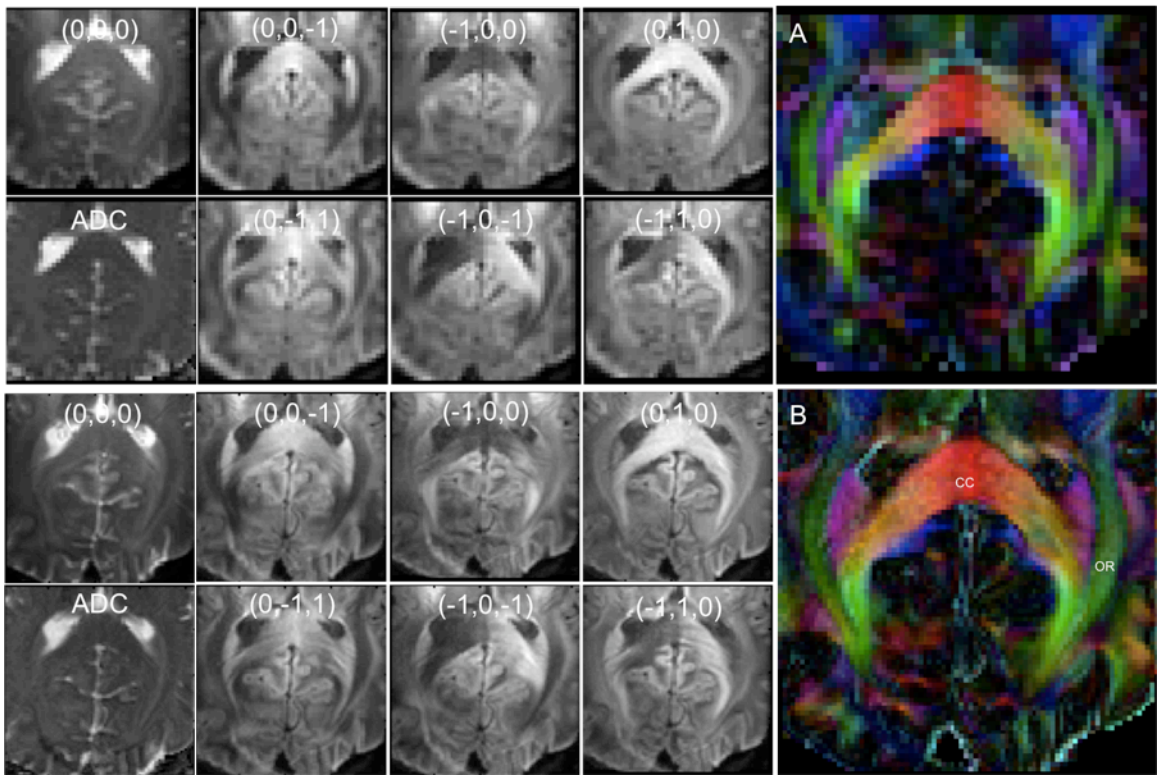

Figure 6.6 – Diffusion weighted OVS visual cortex images at A.) 2mm x 2mm x 2mm, and B.) 1mm x 1mm x 2mm, showing each diffusion direction for b = 1000 s/mm^2, b=0 s/mm^2 image, ADC map, and color-coded FA map showing principal eigenvectors.

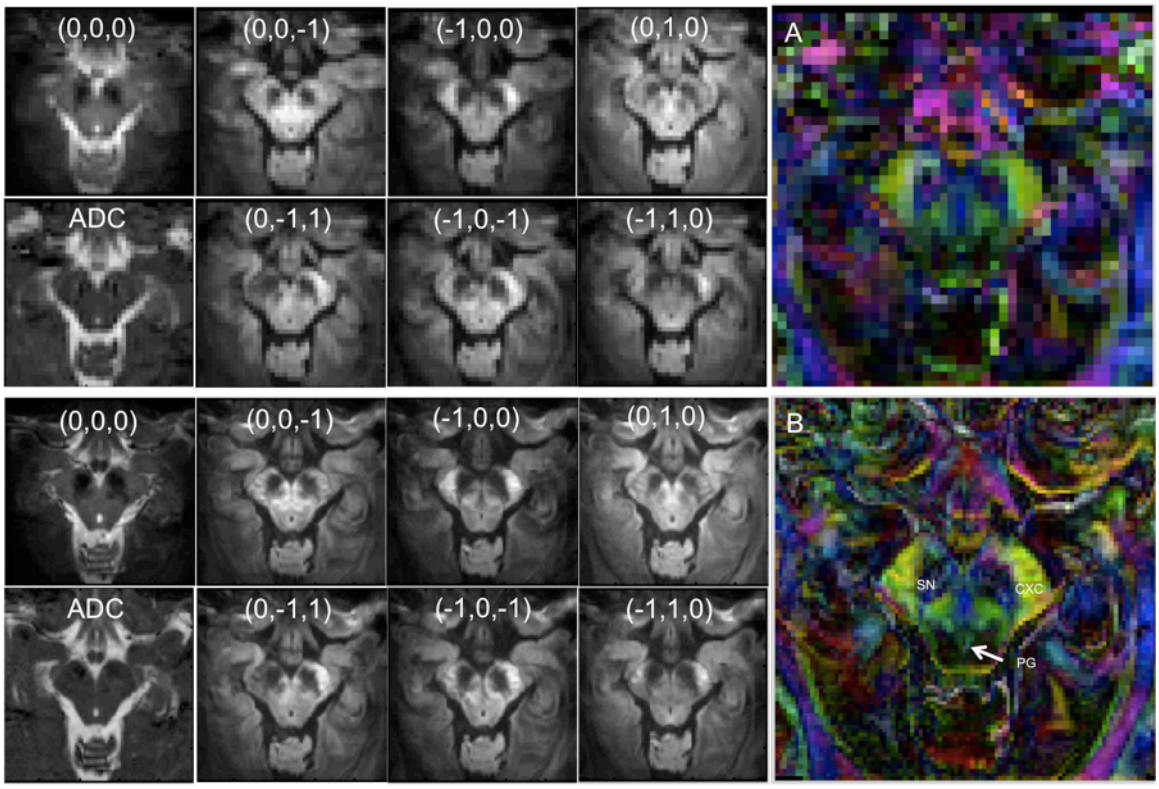

Figure 6.7 – Diffusion weighted OVS substantia nigra images at A.) 2mm x 2mm x 2mm, and B.) 1mm x 1mm x 2mm, showing each diffusion direction for b = 1000 s/mm^2, b=0 s/mm^2 image, ADC map, and color-coded FA map showing principal eigenvectors.

Table 2 – Measured Regional FA and ADC Values

Figure	Location	FA *(2x2 mm²)*	FA *(1x1 mm²)*	ADC *(mm²/s)* *(2x2 mm²)*	ADC *(mm²/s)* *(1x1 mm²)*
3	Internal Capsule	0.711	0.744	8.5×10^{-4}	7.3×10^{-4}
	Corpus Collosum	0.697	0.729	9.7×10^{-4}	9.6×10^{-4}
4	Corpus Collosum	0.851	0.926	0.0016	0.0012
	Brainstem	0.367	0.450	0.0030	0.0018
	Pons	0.551	0.580	0.0013	0.0012
	Optic Chiasm	0.387	0.660	0.0032	0.0016
	Fornix	0.784	0.778	0.0017	0.0017
5	Crus Cerebri	0.767	0.764	0.0016	0.0014
	Substantia Nigra	0.773	0.545	8.9×10^{-4}	0.0015
	Brainstem	0.564	0.534	0.0015	0.0016
	PA Grey	0.263	0.180	0.0021	0.0038
6	Internal Capsule	0.792	0.834	0.0015	0.0014
	Corpus Collosum	0.738	0.787	0.0018	0.0015
	Hippocampus	0.565	0.705	0.0020	0.0015
	Middle Cer. Ped.	0.493	0.518	0.0015	0.0011
	Substantia Nigra	0.526	0.613	0.0014	0.0010
	Thalamus	0.283	0.336	0.0015	0.0014
7	Corpus Collosum	0.801	0.816	0.0014	0.0014
	Optic Radiation	0.585	0.621	0.0016	0.0015
	Internal Capsule	0.617	0.621	0.0015	0.0015

Table 2 – Mean FA and ADC values for each OVS-DTI brain region at 1 mm^2 and 2 mm^2 resolutions for ROI's corresponding to specific fiber tracts. Figure numbers correspond to subsequent figures showing each region image set.

4.2 High Resolution Reduced-FOV Imaging of the Human Cervical Spinal Cord

Axial localization of the cervical spinal cord is displayed in figure 6.8 at 500 and 300 μm resolutions at different spinal cord locations, with additional rFOV imaging of the cerebellum. Axial images corresponded to a three-fold FOV reduction for six-fold total when combined with SENSE. OVS provided distinct reductions without aliasing. However, despite use of SPIR fat suppression, some images show evidence of residual fat fold-over artifacts. Slight distortions at the edge of the cord cross section are apparent as a shading effect, but are not worse at the higher resolution. Contrast is sharply defined between cerebro-spinal fluid (CSF) and spinal cord neurological tissue, with slight grey and white matter contrast and visibility of dorsal and ventral roots. Cerebellum rFOV images demonstrated distinct grey and white matter contrast enabling identification of branches throughout. 300 μm demonstrated no additional artifacts compared to the 500 μm images. Total scan durations for the 500 and 300 μm data were 1m30s and 4m50s, respectively.

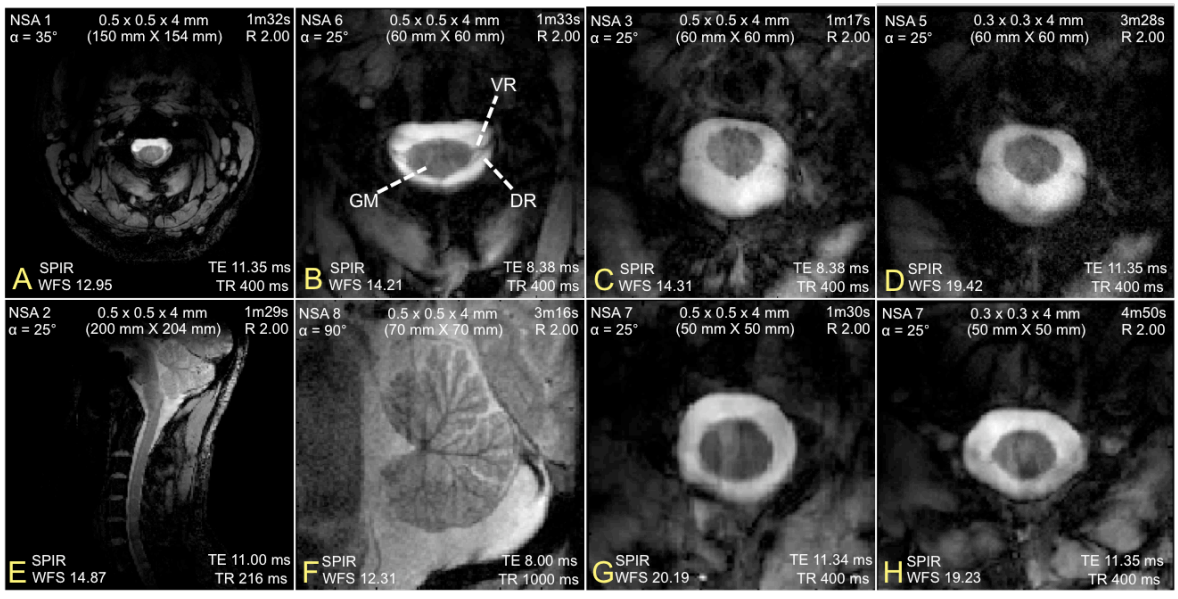

Figure 6.8 – OVS cervical spinal cord images: A.) full axial 500 μm, B,C .) 60x60 mm^2 reduced 500 μm axial, two spine levels, with visible dorsal and ventral roots (DR/VR) and gray matter (GM), D.) 60x60 mm^2 300 μm axial, E.) full sagittal 500 μm, F.) 70x70 mm^2 500 μm sagittal cerebellum, G.) 50x50 mm^2 500 μm axial, and H.) 50x50 mm^2 300 μm axial.

5. DISCUSSION

Application of the IVI and OVS reduced-FOV techniques demonstrated that specific regional localization can be achieved for DWI and DTI that are largely absent of EPI based distortion artifacts. This was consistent despite a two-fold increment in resolution, resulting in no increase in observable artifacts while providing visible improvements in feature identification. The combination of the reduced-FOV methods with SENSE resulted in as much as a seven fold acceleration in acquisition, with a corresponding reduction in echo train lengths for single shot EPI. The short scan times for each individual acquisition provided by both the EPI and rFOV accelerations produces a high degree of motion insensitivity versus other approaches, such as multi-shot EPI techniques, with no visible physiological or patient motion artifacts in the images collected. Typically, multi-shot EPI is applied to reduce distortions that occur with single shot readout; the image quality obtained here for the particular resolutions targeted was not substantial enough to indicate that the EPI based acceleration should be lowered using the multi-shot approach with a lower EPI factor. However, the IVI and OVS methods would readily work without modification with a multi-shot scan, potentially supporting higher resolutions if necessary. Increasing the number of acquisitions to compensate for FOV reduction losses to 20 to 40 as used here does increase sensitivity to inter-scan motion effects. Despite not using registration methods to address this effect, there appeared to be no artifacts suggesting it was significant.

The benefit of the IVI approach for FOV reduction versus OVS for diffusion imaging is a lower overall power deposition as defined by the specific absorption rate (SAR). Here, the system 3 W/kg threshold for human brain imaging necessitated a minimum TR of 900 ms for a single readout when applying OVS. Though well exceeded by the applied TR of 3000 ms, this constraint restricts the number of slices that can be interleaved within a single TR for multi-slice acquisitions without necessitating additional packages that would greatly increase scan times. As described, the DTI application of OVS was optimized with a high SAR FM pulse due to superior suppression performance. Additional pulse types have been tested with the described OVS, including a REST and SINC pulse, which greatly reduce SAR values, and will be applied in future DTI applications. Though IVI has superior SAR performance, multi-slice acquisitions suffer from signal losses due to off-slice saturation effects, which constrained testing to a single slice. IVI also requires additional optimization to properly balance applied spoiling and selection gradients that could impact diffusion weighting across multiple directions beyond the two applied for use with DWI. This will be completed in future work.

Compared to prior studies, to our knowledge, these images represent the first specific localization of diffusion imaging using reduced-FOV methods in many of the regions targeted here in the human brain. Prior investigations applying reduced-FOV have largely been constrained to imaging of the spinal cord where motion and susceptibility issues are problematic. EPI based artifacts are prevalent in a variety of brain areas especially at high field, where the combination of EPI, SENSE, and rFOV can be of benefit when the region of interest is restricted. Images at 1.0 mm x

1.0 mm resolutions match or exceeded a number of reduced-FOV DTI studies that have focused on the spine [5-7], and compare favorably with a number of previous high-resolution full brain DTI scans [3, 13, 14]. The 2 mm slice thickness is larger than an optimal 1.0 mm isotropic resolution, but the signal quality of the acquired DTI images as well as the maximal scan duration of 14 minutes suggests that higher resolutions are possible, which will be the focus of future work. Despite the larger slice thickness, resolution changes from 2 to 1 mm^2 in-plane produced notable improvements in the visibility of features that benefited from the higher signal levels as a result of the thicker slice and decreased partial volume effects. Overall, signal levels remained high despite cutting the resolution in half, with no visible increase in noise levels between the two resolutions within each targeted region. Doubling of the number of acquisitions from a total of 20 to 40 did not fully compensate for the expected SNR loss caused by the resolution improvement, but was sufficient for isolating specific areas and tracts for ADC and FA measurements.

Application of OVS for cervical spinal cord imaging demonstrated similar benefits to that achieved with the DWI and DTI data. Reducing the FOV in this case provides lowered sensitivity to motion, which was not prevalent in any of the images acquired, while potentially shortening scan durations. Suppression based signal localization in this case is challenged by a number of factors, including sufficient saturation of signal, performance in the presence of high susceptibility variation or field inhomogeneity, specific suppression of higher concentrations of fat compared to the scalp for brain imaging, larger amplitude physiological and patient motion effects, and consistent performance across a greater variability in regional properties

between subjects (neck and spine dimensions, and muscle and fat distribution). The suppression challenge of tissue and fat resulted in some case, slight fold-over artifacts. Managing this, in part, requires proper optimization of the shim volume to balance uniform B_0 in the targeted reduced region as well as external to the FOV to insure that applied pulses could sufficiently saturate signal. High degree of field variations in the non-imaged regions that could fold-over often resulted in poor suppression. These variations also induced errors in the scan frequency calibration causing signal losses, as well as potential residual fat signal due to poor performance of fat suppression techniques. A number of these effects potentially have pronounced impact at the 7T field strength. Despite these challenges, the obtained 300 μm resolution represents, to our knowledge, among the highest resolutions cervical spinal cord images at 7T, exceeded only by recent preliminary results by Sigmund at 180 and 220 μm [15, 16]. Future work will incorporate additional slices, resolutions from 160 to 300 μm, and improved suppression.

6. CONCLUSION

In sum, the use of reduced-FOV and SENSE for DTI, DWI, and cervical spinal cord imaging produces high quality high-resolution images in localized regions in reasonable times. For diffusion based protocols in particular, single shot EPI based artifacts are minimized or not apparent, enabling identification of a number of fiber tracts throughout the brain with visible improvement compared to lower resolution scans. This provided targeted FA and ADC measurement in specific fiber tract

locations identified. Similarly, cervical spinal cord imaging using OVS enabled 300 μm resolutions to be obtained with visible contrast of neurological tissue. The combination of IVI, OVS, and SENSE provided as much as a seven-fold acceleration in imaging scans for improved imaging performance.

7. ACKNOWLEDGEMENTS

This work is supported by NIH grant number R01EB000461. The authors would like to acknowledge Ha-Kyu Jeong for his valuable assistance defining the human DTI scan protocol, and Seth Smith for input concerning spinal cord imaging. DTI reconstructions were performed using public Matlab code provided by Dirk-Jan Kroon, adapted for the specific applications demonstrated here.

8. REFERENCES

[1] T. Jaermann, G. Crelier, K.P. Pruessmann, X. Golay, T. Netsch, A.M. van Muiswinkel, S. Mori, P.C. van Zijl, A. Valavanis, S. Kollias, P. Boesiger, SENSE-DTI at 3 T, Magnetic resonance in medicine : official journal of the Society of Magnetic Resonance in Medicine / Society of Magnetic Resonance in Medicine, 51 (2004) 230-236.

[2] K.P. Pruessmann, M. Weiger, M.B. Scheidegger, P. Boesiger, SENSE: sensitivity encoding for fast MRI, Magn Reson Med, 42 (1999) 952-962.

[3] T.K. Truong, B. Chen, A.W. Song, Integrated SENSE DTI with correction of susceptibility- and eddy current-induced geometric distortions, Neuroimage, 40 (2008) 53-58.

[4] R.M. Heidemann, D.A. Porter, A. Anwander, T. Feiweier, K. Heberlein, T.R. Knosche, R. Turner, Diffusion imaging in humans at 7T using readout-segmented EPI and GRAPPA, Magnetic resonance in medicine : official journal of the Society of Magnetic Resonance in Medicine / Society of Magnetic Resonance in Medicine, 64 (2010) 9-14.

[5] B.J. Wilm, J. Svensson, A. Henning, K.P. Pruessmann, P. Boesiger, S.S. Kollias, Reduced field-of-view MRI using outer volume suppression for spinal cord diffusion imaging, Magn Reson Med, 57 (2007) 625-630.

[6] N.G. Dowell, T.M. Jenkins, O. Ciccarelli, D.H. Miller, C.A. Wheeler-Kingshott, Contiguous-slice zonally oblique multislice (CO-ZOOM) diffusion tensor imaging: examples of in vivo spinal cord and optic nerve applications, J Magn Reson Imaging, 29 (2009) 454-460.

[7] J. Finsterbusch, High-resolution diffusion tensor imaging with inner field-of-view EPI, J Magn Reson Imaging, 29 (2009) 987-993.

[8] E.K. Jeong, S.E. Kim, J. Guo, E.G. Kholmovski, D.L. Parker, High-resolution DTI with 2D interleaved multislice reduced FOV single-shot diffusion-weighted EPI (2D ss-rFOV-DWEPI), Magn Reson Med, 54 (2005) 1575-1579.

[9] E.U. Saritas, C.H. Cunningham, J.H. Lee, E.T. Han, D.G. Nishimura, DWI of the spinal cord with reduced FOV single-shot EPI, Magn Reson Med, 60 (2008)468-473.

[10] P. Hiepe, K.H. Herrmann, C. Ros, J.R. Reichenbach, Diffusion weighted inner volume imaging of lumbar disks based on turbo-STEAM acquisition, Z Med Phys, (2011).

[11] D.A. Feinberg, J.C. Hoenninger, L.E. Crooks, L. Kaufman, J.C. Watts, M. Arakawa, Inner volume MR imaging: technical concepts and their application, Radiology, 156 (1985) 743-747.

[12] P.J. Basser, C. Pierpaoli, Microstructural and physiological features of tissues elucidated by quantitative-diffusion-tensor MRI, Journal of magnetic resonance. Series B, 111 (1996) 209-219.

[13] K.M. Hasan, A. Kamali, L.A. Kramer, Mapping the human brain white matter tracts relative to cortical and deep gray matter using diffusion tensor imaging at high spatial resolution, Magn Reson Imaging, 27 (2009) 631-636.

[14] T. Jaermann, G. Crelier, K.P. Pruessmann, X. Golay, T. Netsch, A.M. van Muiswinkel, S. Mori, P.C. van Zijl, A. Valavanis, S. Kollias, P. Boesiger, SENSE-DTI at 3 T, Magn Reson Med, 51 (2004) 230-236.

[15] A.E. Grams, O. Kraff, L. Umutlu, S. Maderwald, P. Dammann, M.E. Ladd, M. Forsting, E.R. Gizewski, MRI of the lumbar spine at 7 Tesla in healthy volunteers and a patient with congenital malformations, Skeletal Radiol, (2011).

[16] E.E. Sigmund, C. Hu, G. Suero, J. Helpern, High resolution anatomical imaging of the spinal cord at 7 T, in: Proc. Intl. Soc. Magn. Reson., Stockholm, Sweden, 2010, pp. 449.

CHAPTER VI

DISCUSSION

The work presented above describes the implementation and optimization of reduced-FOV MRI techniques at ultra-high field strength and demonstrates the benefits of this approach for high-resolution human imaging to achieve quality images with scan times greatly diminished. The first aim, in particular, provided the first comprehensive analysis and comparison of a variety of reduced-FOV techniques that, to date, had only been independently explored by prior authors at lower field. The results here describe the first implementation, optimization, and assessment of each at 7T. As described, 7T presents a number of challenges, including increased B1 inhomogeneity, shorter tissue T2* values resulting in increased susceptibility based distortion and blurring artifacts, and higher SAR. Any selective RF pulse requires proper management of these effects to ensure signal excitation is well localized, complete, and uniform while not exceeding SAR constraints with desired image parameters. In the context of reduced-FOV, this is important to ensure that aliasing artifacts are prevented when the FOV is diminished.

The result of this optimization provided a unique implementation of the OVS technique with SAR values that permitted minimum TR values lower than those established by prior authors at lower field strengths [1] while still achieving 90% suppression levels. Four permutations of the IVI approach were also presented that addressed both reduced-FOV and 7T field dependent constraints distinct from

previous studies [2-5]. This included the use of composite RF pulses and RF scaling to achieve uniform B1, a 2D spiral guassian excitation RF pulse with adjustable profile dimensions, and application of a second off-slice excitation pulse to minimize saturation of neighboring slices. The analysis presented provides the first comprehensive assessment of the relative multi-slice impact of reduced-FOV methods through simulation and experiments, with insights on how to minimize losses by pulse order choices, TR values, interleave numbers, and the suggested pulse additions. The analysis of STEAM, PRESS, OVS, IVI, and BISTRO established specific metrics for determining the optimal method for reduced-FOV imaging in a manner that had not been performed at any field strength with. In many cases, no clear justification has previously been provided to explain the use of one method over another for reduced-FOV or other applications. This comparison has implications not only for their use for the intended reduced-FOV imaging, but could be relevant for spectroscopic applications that commonly apply these same techniques to achieve voxel localization for single voxel spectroscopy.

In sum, the first aim provided a comprehensive basis to support the methods applied in the subsequent work described in this thesis. Specifically, the results primarily indicated that IVI was superior in terms of producing the minimum SAR, close to 100% suppression, and minimal artifacts. The permutations of this technique have potential benefits to address B1 inhomogeneity and multi-slice losses, but were not robust enough to contribute to subsequent studies. Though the OVS assessment produced higher SAR values, lower suppression, and in some cases, resulted in slight fold-over artifacts, IVI was restricted to spin echo imaging,

necessitating use of OVS for more general protocols such as gradient echo imaging. As such, OVS was primarily applied to facilitate a greater variety of scan types and contrast in the human studies.

The primary motivation behind exploring the reduced-FOV methods was the benefit of this class of rapid imaging techniques for high-resolution imaging in the human brain, which served as the focus for the second aim. The resulting technique that was developed to demonstrate the potential benefits of reduced-FOV application in brain imaging consisted of a unique combination of SENSE parallel imaging, IVI and OVS reduced-FOV, and multi-shot EPI. Prior studies had focused on at most, the use of a pair of these techniques versus combining all three [6, 7]. The results of this work demonstrate that this synergistic combination for high-resolution imaging enables massive acceleration of the large data arrays while countering the challenges if each was applied independently. EPI can achieve 20 to 85 fold accelerations, but produces distortion artifacts with large echo train lengths; SENSE provides two to four fold reductions and lowers echo train lengths for improved EPI performance, but contributes significant g-factor noise at high acceleration; reduced-FOV supplies a three to five fold acceleration or higher for further EPI improvement while not contributing g-factor noise, but results in the restriction of imaging to subregions of the object. The specific synergy of low SENSE factors (R=2) with reduced-FOV to produce superior SNR than rFOV or SENSE only is a unique finding that enabled larger FOV sizes with rFOV while maintaining a high degree of acceleration.

The combination of these techniques ultimately produced scans in this work that are: 1.) very rapid, 100 to 500 times faster than a traditional scan; 2.) have reduced sensitivity to motion and EPI artifacts despite high resolution; 3.) are highly localized to target anatomical regions, and 4.) capable of resolutions down to 160 μm without producing significant artifacts. The resolutions specifically achieved match or exceed those currently published at 7T and lower field strengths for *in vivo* human brain imaging [8, 9]. Extended to single-shot EPI, a remarkable improvement in image quality through reduced distortions was observed at 240 μm resolutions in the brain, which could be used to obtain high resolution anatomical data or support functional scans. Use of both OVS and IVI for this aim demonstrated these results are consistent for a variety of contrast types, including T2 spin echo and T2* gradient echo weighting. Additionally, the variety of regions targeted in the cortex and midbrain support the use of the optimized protocol for a range of anatomical studies, enabling identification of a number of features as the resolution improved.

The second aim of this work also defined a specific combination of both IVI and OVS with SENSE along two dimensions and a single or multi-shot EPI for highly acceleration 3D scans. In this case, 1400 fold accelerations to reduce scan times from hours with traditional scans to three to six minutes while obtaining quality images at resolutions as low as 300 μm. The use of 3D imaging in this case overcomes some of the limits of both IVI and OVS that have restricted multi-slice use due to off-slice saturation effects or permitting only a small number of interleaves due to high SAR values. EPI traditionally is not applied for 3D scans with high-resolution, especially with single shot readout due to the excessively long echo

train lengths required that result in severe distortions. Here, the combined SENSE and reduced-FOV methods with rFOV support EPI use for 3D anatomical high-resolution studies that can be well localized or customized to specific target regions.

Aim three extends the human imaging results by using the methods in applications where sensitivities to motion and EPI based artifacts are pronounced. Specifically, IVI and OVS were applied for DTI and high-resolution cervical spine imaging. From a DTI perspective, the results demonstrated that largely artifact free diffusion images can be obtained in localized brain regions. To our knowledge, this represents the first application of rFOV to localize diffusion measurements to the targeted brain regions at the resolutions obtained. Prior studies had focused primarily on applications of DTI to the spine [5, 10]. The benefit of the combined parallel reduced-FOV approach here is the same as that demonstrated in the second aim; it establishes high accelerations for reduced motion sensitivity while minimizing EPI artifacts and g-factor noise effects. The 1 mm^2 resolutions obtained enabled ADC and FA values to be localized to a number of tracts with regional measurements that could have implications for pathologic studies. The comparison with 2 mm^2 scans underlined the benefits of improved resolution to reduce partial volume effects that can impact measured values.

Patient and physiological motion effects and high susceptibility variations that exceed those observed in the brain additionally challenge imaging of the cervical spine. Here again, the reduced-FOV approach was demonstrated to be well suited to address these issues, enabling 300 μm resolutions to be obtained in axial profiles across the spine using OVS. Performance of the applied reduced-FOV method,

however, could benefit from additional optimization. Applied saturation pulses that experience high variation in B1 and B0 appear to produce lowered suppression, especially in the presence of high fat regions, resulting in aliasing effects. Despite these challenges, the resolutions obtained correspond to a remarkable improvement relative to 3T and lower field studies, and constitute among the highest obtained at 7T [11, 12], supporting investigations of spine disease and neurological function.

REFERENCES

[1] B.J. Wilm, J. Svensson, A. Henning, K.P. Pruessmann, P. Boesiger, S.S. Kollias, Reduced field-of-view MRI using outer volume suppression for spinal cord diffusion imaging, Magn Reson Med, 57 (2007) 625-630.

[2] D.A. Feinberg, J.C. Hoenninger, L.E. Crooks, L. Kaufman, J.C. Watts, M. Arakawa, Inner volume MR imaging: technical concepts and their application, Radiology, 156 (1985) 743-747.

[3] J. Finsterbusch, Fast-spin-echo imaging of inner fields-of-view with 2D-selective RF excitations, J Magn Reson Imaging, 31 1530-1537.

[4] D. Mitsouras, R.V. Mulkern, F.J. Rybicki, Strategies for inner volume 3D fast spin echo magnetic resonance imaging using nonselective refocusing radio frequency pulses, Med Phys, 33 (2006) 173-186.

[5] E.K. Jeong, S.E. Kim, J. Guo, E.G. Kholmovski, D.L. Parker, High-resolution DTI with 2D interleaved multislice reduced FOV single-shot diffusion-weighted EPI (2D ss-rFOV-DWEPI), Magn Reson Med, 54 (2005) 1575-1579.

[6] C.F. Schmidt, K.P. Pruessmann, P. Boesiger, Spatial resolution enhancement using sensitivity-encoded echo-planar imaging at 3T in a typical motor paradigm, Computerized medical imaging and graphics : the official journal of the Computerized Medical Imaging Society, 31 (2007) 704-714.

[7] O. Speck, J. Stadler, M. Zaitsev, High resolution single-shot EPI at 7T, Magma, 21 (2008) 73-86.

[8] J.M. Theysohn, O. Kraff, S. Maderwald, M.U. Schlamann, A. de Greiff, M. Forsting, S.C. Ladd, M.E. Ladd, E.R. Gizewski, The human hippocampus at 7 T--in vivo MRI, Hippocampus, 19 (2009) 1-7.

[9] B.P. Thomas, E.B. Welch, B.D. Niederhauser, W.O. Whetsell, Jr., A.W. Anderson, J.C. Gore, M.J. Avison, J.L. Creasy, High-resolution 7T MRI of the human hippocampus in vivo, J Magn Reson Imaging, 28 (2008) 1266-1272.

[10] J. Finsterbusch, High-resolution diffusion tensor imaging with inner field-of-view EPI, J Magn Reson Imaging, 29 (2009) 987-993.

[11] A.E. Grams, O. Kraff, L. Umutlu, S. Maderwald, P. Dammann, M.E. Ladd, M. Forsting, E.R. Gizewski, MRI of the lumbar spine at 7 Tesla in healthy volunteers and a patient with congenital malformations, Skeletal Radiol, (2011).

[12] E.E. Sigmund, C. Hu, G. Suero, J. Helpern, High resolution anatomical imaging of the spinal cord at 7 T, in: Proc. Intl. Soc. Magn. Reson., Stockholm, Sweden, 2010, pp. 449.

CHAPTER VIII

FUTURE WORK

1.1 Implementation of a Multi-Slice Compatible Inner-Volume Imaging Technique

One of the primary constraints of the described selective excitation reduced-FOV approaches is their application for multi-slice imaging scans. As assessed in the first aim, this is due to saturation of spins in off-slice locations by pulses that restrict signal along the x and y dimensions. The perturbed magnetization has a short duration over which to recover to its maximal value to ensure there is no overall SNR loss in the obtained image. Multi-slice imaging is a common approach to achieve efficient scan durations versus conventional 2D imaging that acquires k-space information for only one slice every TR. For broad application, the reduced-FOV approaches must overcome this limitation.

A number of solutions were explored in the first aim using simulation to reduce off-slice losses, including reordering of the PRESS excitations and applying a double off-slice excitation with IVI while maximizing TR values relative to the desired number of slices interleaved. In this regard, future work requires implementation of the described solutions to verify simulation predictions. However, the expected improvements do not ensure full recovery of the saturated magnetization, with residual M_Z simulated after the first interleave only. Acquiring a high number of slices within one TR could have a compounding effect that would further reduce

available signal for imaging. The optimal solution is a reduced-FOV approach that does not in any way impact the available magnetization in a neighboring slice.

The described IVI method that applies a spiral Gaussian excitation offers a potential solution to this problem by selectively restricting excitation in two-dimensions with a single pulse. The extent to which neighboring slices are affected is dependent on the 2D profile for this excitation, which can be customized by scaling each dimension of the pulse shape. Aim 2 described efforts to reduce the profile of this pulse to within the dimensions of a typical slice thickness, but was not readily tested with a multi-slice protocol. Additional work with IVI specifically would focus primarily on this optimization to achieve 2D excitation that can establish 2-6 mm slice thicknesses and 20-100 mm phase encoding widths for localized excitation. A proposed modification to the described 2D RF approach would use a rectangular weighting function instead of a Gaussian to improve profile shapes [1, 2]:

$$W(k_X, k_Y) = h(k_X, k_Y) \cdot rect(\alpha_X \cdot k_X) \cdot rect(\alpha_Y \cdot k_Y) \qquad 8.1$$

This function results in a 2D square excitation, the dimensions of which are scaled by α_X and α_Y, with $h(k_X,k_Y)$ serving as a Hanning window to reduce ripple effects in the established excitation. Preliminary experiments were performed to assess the potential application of this function for IVI reduced-FOV imaging applying the same overall sequence described in aim 1 for the 2D RF approach. Figure 8.1 summarizes these preliminary tests. Here, A and B demonstrated the relative scaling possible with sharp edge boundaries compared to using only a Gaussian, with ripple diminished in C and D by optimizing the Gaussian to serve as the Hanning window function. The plot demonstrates the slice profile along both

dimensions achieved for the narrower thickness (B and D), producing a measured FWHM in both dimensions of 44.3 mm and 6.6 mm. However, an image of the achieved in-plane excitation reduction (figure 8.1 C and E) demonstrates some distortion along the length of restricted area. The achieved slice thickness of 6.6 mm also requires further optimization to allow for narrower slice thicknesses and gaps to insure as few slices as possible are impacted by the 2D pulse.

Overall, if 1 to 3 mm slice thicknesses can be achieved using a 2D RF pulse, the additional benefit of this approach is that a refocusing pulse is no longer required to achieve slice selection as performed for a standard IVI protocol. This extends the use of IVI for both gradient echo and spin echo scans versus spin echo only as performed throughout all three aims. OVS served as the primary option for gradient echo FOV reduction, but has higher SAR values and does not suppress signal as well as IVI. Establishing an IVI version as described here creates a highly flexible reduced-FOV approach that could be used with a variety of scans.

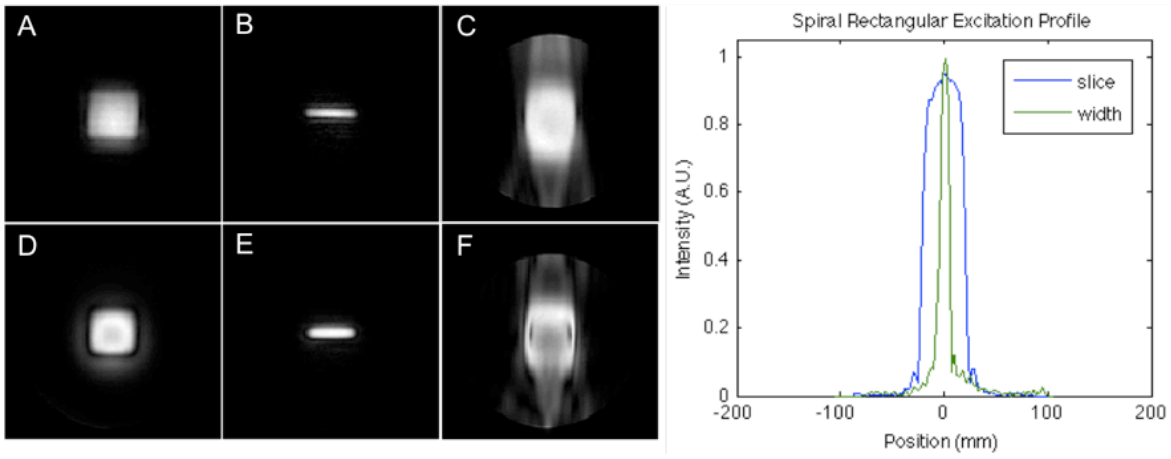

Figure 8.1 – Rectangular spiral IVI 2DRF exciting A.) 44x44 mm^2 FOV, B.) 44x6 mm^2 FOV, C.) 40 mm wide slab, 6 mm thickness, D-F) repeated with Gaussian hanning window. Profile plot for C along both slice and width dimensions.

1.2 Improving Outer-Volume Suppression SAR and Suppression Performance

Compared to the other methods explored, OVS provided the greatest flexibility for implementation with a variety of scan protocols by enabling application with spin echo or gradient echo sequences and does not induce multi-slice signal losses. However, OVS is restricted by higher overall SAR values, lower suppression with the potential for fold-over artifacts, and is performed prior to scans resulting in a longer scan duration compared to IVI. SAR constraints necessitated a TR no less than 900 ms, which is prohibitive for a number of T1 weighted protocols. This was improved upon in the second aim that explored human imaging applications of IVI and OVS by using two different pulse types enabling TR values as low as 400 ms. Suppression, in general, remained at approximately 90%, which, for many regions, was sufficient to prevent aliasing, but in areas such as the cervical spine, produced residual fold-over effects from fat and other tissues.

Future work in this respect will target exploration of a variety of pulse types and configurations to further reduce SAR values, obtain suppression closer to 100%, and perform well with a variety of tissue types. Poor suppression for some experiments, in part, may be due to B1 and B0 field inhomogeneity effects. A preliminary exploration of a variety of pulses in the software library for the Philips system provided a relative comparison of SAR and suppression values with an approximate optimization in a phantom, as presented in figure 8.2. The described frequency modulated, SINC, and REST slabs used in the aims were largely selected from this analysis. However, a number of other pulse types may be equally viable with improved selection of pulse shapes, angles, orders, and repetitions. In addition,

optimization was specifically performed using an FBIRN agar gel phantom that produced a high degree of B1 variability not observed in any of the human experiments. In some cases, an alternate optimization may work well for subject scans that have overall superior performance and lower SAR values than those applied here.

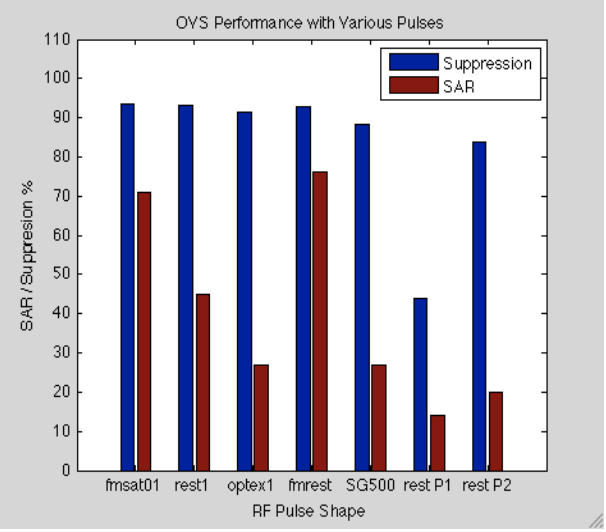

Figure 8.2 – Library pulses attempted for OVS showing percent suppression and SAR.

In the end, achieving improved performance may require uniquely designed RF pulses not found in the scanner software library. Optimized adiabatic pulses, in particular, have potential improved insensitivity to B1 inhomogeneity, with additional customization of the pulses used here specifically for BISTRO a potential area for future efforts. Though not described in the methods development work, alternate pulse organization strategies were explored, including a "Hadamard" style configuration that enabled a single pulse to be used to simultaneously excite two saturation band locations. This is accomplished by multiplying a specific RF pulse with a cosine having a frequency that matches the desired slab positions [3]:

$$S(t) = F(t) * \cos(2\pi f \cdot t) \qquad 8.2$$

Once Fourier transformed, in the k-space domain, this corresponds to the convolution of an ideally rectangular pulse excitation shape with the transform of the cosine, which is an impulse at ±f. The pulse is effectively replicated at the two impulse frequencies enabling simultaneous excitation at those two locations. Figure

8.3 summarizes the design and implementation of such a pulse. The potential benefits of this design is an overall shorter OVS preparation duration. A portion of the current loss in suppression with existing OVS techniques is due to T1 recovery caused by long preparation times. Initial implementation of the approach demonstrated localization, but with some distortion in the shape and suppression not optimized. Overall, additional work with this approach and other pulse options could potentially improve OVS performance.

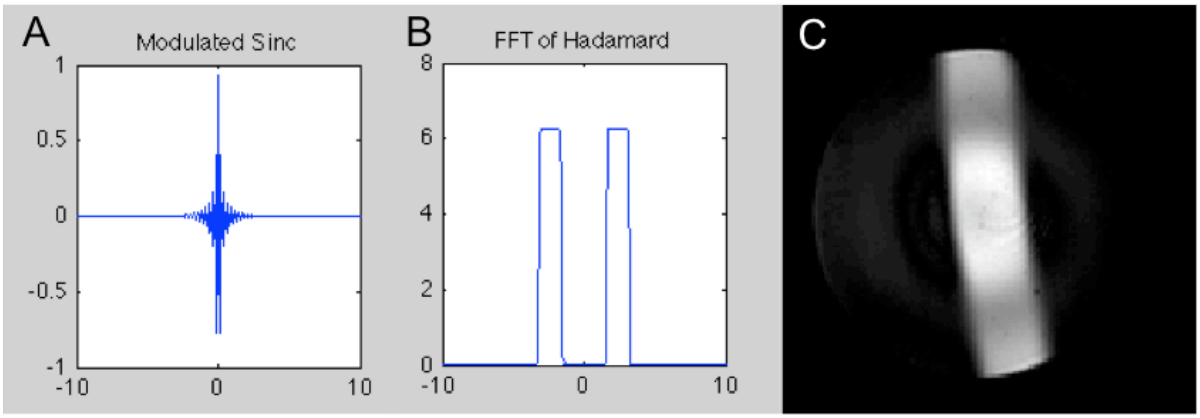

Figure 8.3 – A.) SINC RF pulse modulated with cosine, B.) corresponding fourier transform showing slab positions achieved with one pulse, C.) imaged OVS preparation in FBIRN phantom to achieve 40 mm wide slab, using 100 mm wide saturation bands.

1.3 Reduced-FOV Power Calibration for Optimal B1 Performance

In aim 1, IVI was tested using scaled RF pulses to address localized signal losses caused by B1 inhomogeneity that translated into lowered established flip angles. It was demonstrated that in a reduced-FOV scan using dimensions on the order of 40 mm^2 to 60 mm^2, pulse scaling provide up to a 35% improvement in SNR due to lower inhomogeneity in the localized region compared to calibrations based on exciting the entire full-FOV. Practical implementation of this approach, however, requires knowledge of the B1 error in each particular region to define the correct

scaling factor for maximal SNR. The aim 1 results demonstrated that the appropriate factor could vary substantially across target regions. Versluis accomplished similar scaling for spectroscopic applications by localizing power calibrations to small FOV regions, with 22% to 166% gains in the achieved SNR [4]. This was accomplished by applying selective pulses to generate a stimulated echo restricted to the target FOV that was then used for RF pulse power optimization. Such an approach could work equally well for the imaging studies described throughout the aims that reduce the FOV similarly to that applied for spectroscopic studies. Preliminary investigation of the Versluis power optimization has been implemented on the 7T system for spectroscopy, with future work targeting extension to imaging for seamless optimization of RF pulses for a variety of studies.

1.4 Addressing Intra-Scan Motion Using Registration and Gating Methods

To compensate for SNR losses caused by phase encoding dimension reduction for smaller FOV sizes, the human imaging experiments incorporated additional acquisitions. In some cases, acquisition numbers exceeded 100 that necessitated increasing the default scanner system software limit of 32. Though the short individual acquisition times reduce sensitivity to intra-scan motion, inter-scan motion sensitivity potentially increases because of the high number of acquisitions. For incoherent motion such as general movement of the head, this can result in a blurring effect in the image; for coherent sources such as respiration, cardiac motion, or blinking, ghosting artifacts can be reinforced. Potential solutions to these effects include registration of the individual acquisitions prior to combination [5], respiratory or cardiac gating [6], and use of navigators for multi-slice EPI readout [7].

A preliminary investigation of registration-based improvement was performed for small FOV anatomical imaging scans. From a single slice reduced-image with no apparent motion artifacts, a stack of images was generated, each with a unique random rotation and offset that exceeded no more than four pixels to simulate patient motion. To replicate the lower SNR typically expected for each frame, a 10% random noise distribution was also incorporated into each image. All noised and rotated images were summed to show the overall impact of the errors in a combined image. The images were then all registered to the first using an affine transformation and combined to produce the registered sum. Figure 8.4 (A-D) demonstrates the resulting simulated improvement, with a visible distinction of a number of features lost in the unregistered combined sum.

The developed registration program was additionally tested using stacks of collected human image data in an IVI reduced-FOV with acquisitions separated. This was performed specifically in 30 mm^2 and 60 mm^2 FOV sizes targeting the hippocampus and lentiform, respectively, with as high as 50 total individual acquisitions. The images were combined unregistered as with the simulated data, and then combined after registration, with results presented in figure 8.4 (E-G). In this case, the registration did not produce a notable improvement in image quality, with close inspection revealing slight loss of small vessel features. However, the combined image without registration did not indicate significant motion for this study. Future work will focus on additional exploration and application of the registration for regions highly sensitive to motion, such as the cervical spine. The work will be

combined with gating and navigator approaches to determine feasibility for image quality improvement for high acquisition numbers using reduced-FOV methods.

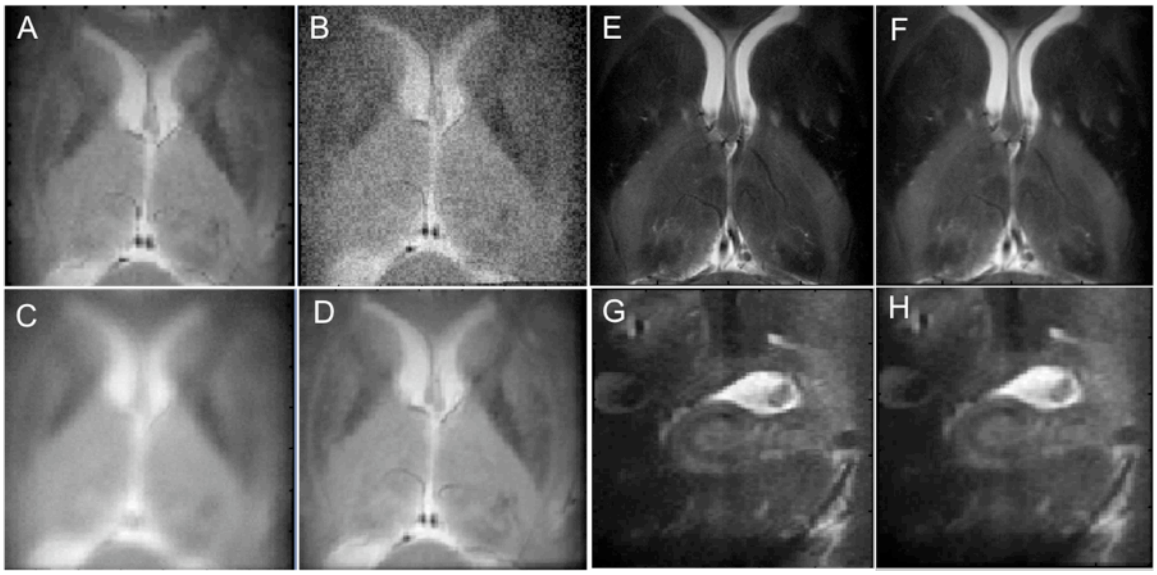

Figure 8.4 – A.) Original single human image to generate stack of 50 slices with offset and angle shifts, B.) with 10% noise level added, C.) sum of stack unregistered, D.) sum of registered motion simulated data. E.) Sum of multiple acquisitions collected in human, F) registered and summed, repeated in hippocampus (G,H).

1.5 Reduced-FOV Excitation Using Arbitrary FOV Shapes

Flexibility in FOV sizes as well as shapes could potentially provide enhanced localization of excitations, or serve as a mechanism to correct for B1 inhomogeneity using complex pulse patterns. Signal could be further restricted to regions that are not defined by square dimensions, which could further compress data sizes. These types of techniques could be compliant with protocols attempting to obtain precise restriction of signal to measure parameters such as relaxation or functional bold response in target areas, or could support establishing sparsity for compressed sensing rapid imaging techniques for additional acceleration of acquisitions.

Preliminary work to generate arbitrary excitations was performed using a combination of a spoke-based methodology [8] with the IVI technique. Similar to the spiral and composite pulse approaches described in aim 1, spokes achieves a target excitation pattern by applying RF pulses along a specific trajectory through excitation k-space, weighted by the target pattern. Typically with spokes, this constitutes a relatively small number of points and is performed along three dimensions, with the trajectory defined by a composite of x, y, and z gradients. As a proof of concept, we attempted to establish both a square pattern and checkerboard excitation. A composite RF pulse interleaved with x and y gradients were defined by simulation to determine optimal pulse amplitudes, phases, and gradient amplitudes. The pulse was followed by a refocusing pulse to achieve slice selection, with results shown in figure 8.5 in a phantom. Excited patterns matched well with simulated results.

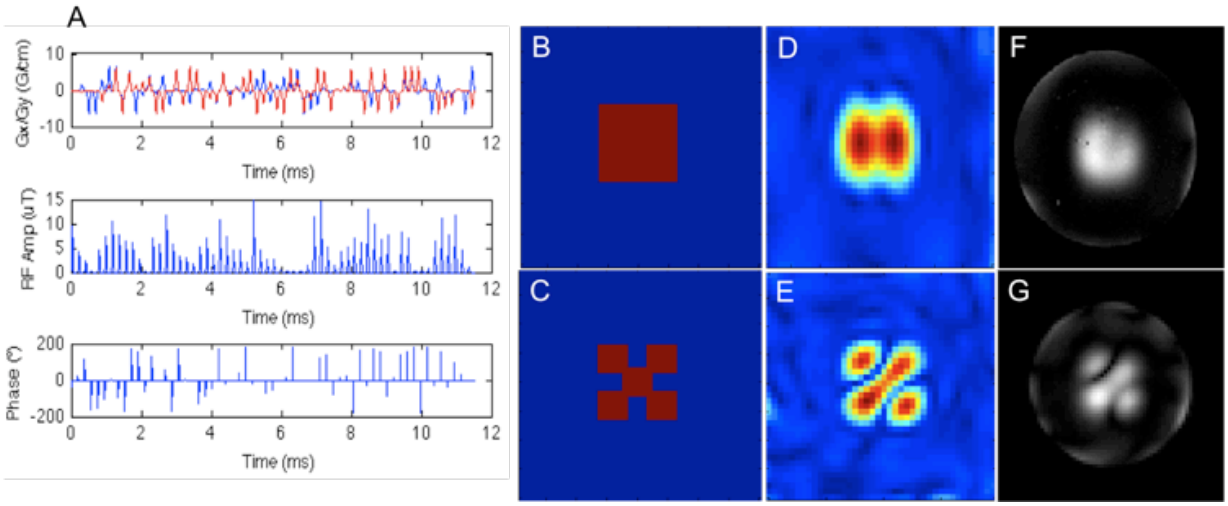

Figure 8.5 – A.) Spoke based x and y gradient profile, RF amplitude and phase. B,C.) Target square and checkboard excitation pattern, D,E.) simulated excitation, F,G.) actual excitation in FBIRN phantom using spoke-IVI approach.

Similar excitation could be achieved using the spiral excitation method by altering the weighting function, or could incorporate maps of the B1 inhomogeneity in an attempt to simultaneously restrict the FOV and produce appropriate B1 distributions. Generally, all of these techniques have difficulty in defining sharp boundaries or transitions due to sparse sampling of excitation k-space without producing excessively long pulse durations which would be prone to T2* effects. Parallel transmit arrays provide a potential mechanism for reducing overall pulse durations to address this problem while incorporating the possibility to apply multiple pulses with unique shapes, phases, and amplitudes for a customized combined effect. This could enhance shape definition, B1 correction, or could be used with previously described 2D RF IVI for narrower slice profiles. In general, this extension may be necessary for advanced applications of reduced-FOV at 7T and warrants further investigation as parallel transmit technology is incorporated.

1.6 General Reduced-FOV Implementation with A Variety of Scan Types

For use with a broad range of scan types and protocols, the described reduced-FOV techniques require additional optimization and testing. Specifically, Turbo Spin-Echo (TSE), Turbo Field Echo (TFE), Gradient Spin Echo (GRASE), and inversion recovery based sequences have been preliminarily implemented but not fully tested with the IVI and OVS methods described. Specific readouts are also of interest, including radial, spiral, as well as EPI forms of these listed scan types. Spiral acquisition, in particular provides potential enhanced motion insensitivity. As mentioned, the OVS approach can be readily implemented with these techniques without significant coding changes since it performs prior to scans. However, some

attention is necessary to insure signal can sufficiently stay saturated external to the target FOV before T1 recovery begins to restore enough signal to cause fold-over effects. Lastly, alternate forms of contrast, such as T1 weighted and susceptibility weighted scans, also require further optimization for regular use.

1.7 Reduced-FOV Imaging Using Parallel Transmit at 7 Tesla

For all of the imaging experiments performed in this work, single channel volume or quadrature surface coil transmission was used to deliver RF pulses for each sequence. Recent advancements in coil technology enable RF to be transmitted by multiple channels simultaneously using parallel transmit arrays, with the potential to specify unique waveform shapes, phases, and amplitudes from each coil array element [9, 10]. The additional customization in the applied RF as a result of using multiple coils can be applied to address B1 inhomogeneity effects, reduce SAR, shorten pulse durations, and provide sharp boundaries for slice profiles or arbitrary excitations [11-13]. In the context of reduced-FOV imaging, addressing any of these constraints with parallel transmission would be of benefit. Specifically, improving B1 inhomogeneity would provide superior SNR performance, reducing SAR and duration limits would address OVS constraints, and improving slice profiles would assist with IVI 2D RF pulse definition using the spiral Gaussian excitation. Many of these issues are of particular constraint at 7T, with parallel transmit targeted for this system in the near future, enabling exploration of its applied benefits. It is expected that it will ultimately improve 7T imaging and reduced-FOV performance for human brain imaging studies and facilitate new reduced-FOV approaches.

REFERENCES

[1] C.J. Hardy, et al, Spatial Localization in Two Dimensions Using NMR Designer Pulses, Journal of Magnetic Resonance, 82 (1989) 647-654.

[2] J. Pauly, et al, A k-space Analysis of Small-Tip-Angle Excitation, Journal of Magnetic Resonance, 81 (1989) 43-56.

[3] M.A. Bernstein, K.F. King, X.J. Zhou, Handbook of MRI pulse sequences, Elsevier Academic Press, Burlington, MA, 2004.

[4] M.J. Versluis, H.E. Kan, M.A. van Buchem, A.G. Webb, Improved signal to noise in proton spectroscopy of the human calf muscle at 7 T using localized B1 calibration, Magnetic resonance in medicine : official journal of the Society of Magnetic Resonance in Medicine / Society of Magnetic Resonance in Medicine, 63 (2010) 207-211.

[5] B. Kim, J.L. Boes, P.H. Bland, T.L. Chenevert, C.R. Meyer, Motion correction in fMRI via registration of individual slices into an anatomical volume, Magnetic resonance in medicine : official journal of the Society of Magnetic Resonance in Medicine / Society of Magnetic Resonance in Medicine, 41 (1999) 964-972.

[6] S. Skare, J.L. Andersson, On the effects of gating in diffusion imaging of the brain using single shot EPI, Magnetic resonance imaging, 19 (2001) 1125-1128.

[7] K.L. Miller, J.M. Pauly, Nonlinear phase correction for navigated diffusion imaging, Magnetic resonance in medicine : official journal of the Society of Magnetic Resonance in Medicine / Society of Magnetic Resonance in Medicine, 50 (2003) 343-353.

[8] M. Jankiewicz, H. Zeng, J.E. Moore, A.W. Anderson, M.J. Avison, E.B. Welch, J.C. Gore, Practical considerations for the design of sparse-spokes pulses, Journal of Magnetic Resonance, 203 (2010) 294-304.

[9] G. Adriany, P.F. Van de Moortele, F. Wiesinger, S. Moeller, J.P. Strupp, P. Andersen, C. Snyder, X. Zhang, W. Chen, K.P. Pruessmann, P. Boesiger, T. Vaughan, K. Ugurbil, Transmit and receive transmission line arrays for 7 Tesla parallel imaging, Magn Reson Med, 53 (2005) 434-445.

[10] K. Setsompop, L.L. Wald, V. Alagappan, B. Gagoski, F. Hebrank, U. Fontius, F. Schmitt, E. Adalsteinsson, Parallel RF transmission with eight channels at 3 Tesla, Magn Reson Med, 56 (2006) 1163-1171.

[11] U. Katscher, P. Bornert, Parallel RF transmission in MRI, NMR Biomed, 19 (2006) 393-400.

[12] U. Katscher, P. Bornert, C. Leussler, J.S. van den Brink, Transmit SENSE, Magn Reson Med, 49 (2003) 144-150.

[13] U. Katscher, P. Bornert, J.S. van den Brink, Theoretical and numerical aspects of transmit SENSE, IEEE Trans Med Imaging, 23 (2004) 520-525.

CHAPTER IX

CONCLUSIONS

The work here supports the use of reduced-FOV techniques when imaging can be localized to a specific target area without sacrificing necessary object information. When such regional localization is desirable based on study of particular brain areas, the reduction achieved by this approach can be used in a variety of ways. First, for a fixed resolution, the total scan time can be diminished as long as predicted SNR losses are supported or addressed. This is warranted if the full-FOV scan has no additional means of reduction; acquisitions are already minimized with each individual acquisition contributing a necessary percentage of the total SNR. Adjusting the FOV in this case enables a finer SNR and scan time alteration by diminishing the imaged dimensions, with each acquisition contributing a relatively smaller percentage of the total SNR compared to the full-FOV case.

Second, for a fixed resolution and SNR, reduced-FOV can be applied to improve image quality by reducing prevalence of artifacts. In this case, each individual acquisition has been performed more rapidly than the full FOV scan, reducing sensitivities of each to motion and susceptibility effects. Increasing the total number of acquisitions enables SNR to be maintained without loss if necessary, producing images of matched resolution and time, but superior quality. In this capacity, the work performed here demonstrated that reduced-FOV methods specifically addressed challenges of EPI based rapid imaging, enabling EPI to be

used at higher resolutions or to be adjusted to larger EPI factors without sacrificing image quality. Third and finally, reduced-FOV enables resolution improvements in situations where SNR is abundant but efficiency or artifact constraints prevent acquisition. This can be accomplished with an imaging time that matches that used currently for a lower resolution scan. For example, halving the resolution while cutting the FOV size in half corresponds to no change in the total number of acquired points with a scan time matching that used at the lower resolution.

The combination of these applied uses provides flexibility and compromises in the achieved resolution, scan time, SNR, artifact sensitivity, and image quality that supports application in a large variety of human imaging studies. Contrasted to SENSE based rapid imaging techniques that apply similar reductions, it enables higher accelerations without a compounding g-factor noise type effect that diminishes SNR. More importantly, the work here demonstrated the synergy of this approach with a variety of techniques to speed up acquisition times, including multi and single-shot EPI, parallel imaging, and partial Fourier approaches. This combination ultimately enabled the high accelerations achieved here, countered a number of challenges of 7T imaging, addressed constraints of the partnered rapid methods, diminished artifacts, and produced high resolution images that covered a large variety of regions in the human brain and spine. Many of these images represent the highest achieved to date in the human, supporting localization and visualization of features important in human imaging using reduced-FOV methods.